

Performance Assessment of a 3-Body Self-Reacting Point Absorber Type Wave Energy Converter

by

Patrick Maloney

BS Florida Institute of Technology 2012

A Thesis Submitted in Partial Fulfillment
of the Requirements for a Degree of

MASTER OF APPLIED SCIENCE

in the Department of Mechanical Engineering

© Patrick Maloney, 2019

University of Victoria

All rights reserved. This thesis may not be reproduced in whole or in part, by photocopy or other means, without the permission of the author.

Supervisory Committee

Performance Assessment of a 3-Body Self-Reacting Point Absorber type Wave Energy
Converter

by

Patrick Maloney

BS Florida Institute of Technology 2012

Supervisory Committee

Dr. Brad Buckham, Department of Mechanical Engineering
Supervisor

Andrew Rowe, Department of Mechanical Engineering
Departmental Member

Abstract

Supervisory Committee

Dr. Brad Buckham, Department of Mechanical Engineering
Supervisor

Andrew Rowe, Department of Mechanical Engineering
Departmental Member

The Variable Inertia System Wave Energy Converter (VISWEC) is a self-reacting point absorber (SRPA) type wave energy converter (WEC) capable of changing its mechanical impedance using an internal reaction mass system. The reaction mass is coupled to a rotating assembly capable of varying its inertia and this changing inertia has the effect of creating an added inertial resistance, or effective mass, to oscillations of the reaction mass. An SRPA has two main bodies, designated Float and Spar, capable of utilizing the relative motion between the two bodies to create power through a power take-off (PTO). The implementation of the reaction mass, a 3rd body, and the variable inertial system (VIS) is designed to change the response of the Spar in order to create larger relative velocities between the two bodies and thus more power. It is also possible to lock the VIS within the Spar, and when this is done the system is reduced to a conventional 2-body SRPA configuration.

To better understand the effects of the implementation of the VIS on the overall stability of the VISWEC and the power conversion performance, a numerical model simulation within ProteusDS, a time-domain modelling software, was created. Power production and parametric excitation are the metrics of comparison between the two systems. Parametric excitation is a phenomenon that correlates wave excitation frequency to roll stability and has been shown to negatively affect power production in SRPAs. Simulations of the 2 and 3-body provide a basis of comparison between the two systems and allow the assessment of parametric excitation prohibited or exacerbated by the implementation of the VIS as well as power production.

The simulation executed within the commercial software ProteusDS incorporates articulated bodies defined with physical parameters connected through connections allowing kinematic constraints and relations and hydrodynamics of the hull geometries as they are exposed to regular waves. ProteusDS also has the ability to apply kinematic constraints on the entire system allowing the analysis of isolated modes of motion.

The implementation of the VIS demonstrates a generally higher power production and stabilization of the system with regards to parametric excitation. While the 3-body system is more stable, the bandwidth at which rolling motion is induced increased in comparison to the 2-body system. Rolling motions in both the 2 and 3-body systems are characteristic of parametric excitation and show a direct correlation to reduced power production. Overall the 3-body VISWEC outperforms the typical 2-body SRPA representation but more research is required to refine the settings of the geometric and PTO control.

Contents

Supervisory Committee	ii
Abstract.....	iii
Contents	v
List of Tables	ix
List of Figures.....	x
Acknowledgements.....	xiv
Dedication.....	xv
Nomenclature.....	xvi
Latin Variables.....	xvi
Greek Variables	xvi
Acronyms.....	xvii
Chapter 1 Introduction	1
1.1 Motivation	1
1.2 Wave Energy Background	2
1.2.1 Historical Developments	2
1.2.2 The Need for Diversity in Renewables	3
1.3 The Wave Energy Resource.....	7
1.4 Wave Energy Converter Classifications	9
1.5 Point Absorbers.....	11
1.5.1 Single Body Point Absorber (SBPA)	13
1.5.2 Self-Reacting Point Absorber (SRPA)	14
1.5.3 Geometrically Controlled SRPAs (GC-SRPA).....	18
1.8 Gap in Knowledge	23
1.9 Thesis Objective and Contribution	24

1.10 Thesis Outline	24
Chapter 2 VISWEC Dynamics.....	26
2.1 Linear Wave Theory and Buoyancy	27
2.2 Parametric Excitation Literature Review.....	30
2.2.1 Spar Platforms	30
2.2.2 WECs.....	32
2.3 Righting Moment.....	33
2.3.1 Buoyant Righting Moment.....	34
2.3.2 Ballasted Righting Moment.....	36
2.4 Rolling Dynamics and the Mathieu Equation.....	38
2.5 Test Case.....	40
2.6 Closing Remarks.....	44
Chapter 3 Model Parameters	46
3.1 Role of Numerical Modelling for WECs	46
3.2 WEC Dynamics Modelling.....	48
3.3 Physical Parameters	50
3.3.1 Environmental and Simulation Parameters	50
3.3.2 Mass and Surface Geometry Models – Float and Spar	53
3.3.3 Variable Inertial System.....	58
3.4 Hydrodynamics	63
3.4.1 Hydrostatic Buoyancy and Wave Excitation Force	64
3.4.2 Radiation	66
3.4.3 Drag.....	68
3.5 Natural Frequency.....	70
Chapter 4 Model Settings.....	71

4.1 Mechanical Impedance and WECs	71
4.2 Impedance Matching.....	78
4.2.1 Single Body Impedance Matching	78
4.2.2 Two-body SRPA Impedance Matching	79
4.2.3 Three-body SRPA Impedance Matching	79
4.3 Assumptions.....	80
4.4 PTO Damping Calculation for the 2-body System	82
4.4.1 Drag Linearization & PTO Impedance Calculation	82
4.4.2 Direct PTO Optimization	85
4.4.3 Power Sensitivity to PTO Damping	87
4.5 PTO Damping Calculation for the 3-body System	88
Chapter 5 Testing Conditions and Results	90
5.1 Wave Parameters	90
5.2 Kinematic Constraints and Performance Metrics	95
5.2.1 Kinematic Cases	95
5.2.2 Performance Metrics	96
5.3 Simulation Results	98
5.3.1 Heave Only	98
5.3.2 Heave and Roll	100
5.3.3 Moored	104
5.3.4 Free	108
5.4 Comparison of Results.....	112
5.4.1 Two-body System Comparison	112
5.4.2 Three-body System Comparison	116
5.4.3 Inter-system Comparison	120

Chapter 6	Conclusions and Future Work	125
6.1	Observational Conclusions	125
6.1.1	PTO Damping Value	125
6.1.2	VIS Implementation	125
6.2	Future Work	126
6.2.1	PTO Value	126
6.2.2	Frequency Testing Range	126
6.2.3	VIS Testing Range	127
6.2.4	Limiting Parametric Excitation	127
References	129

List of Tables

Table 1: Parameters for use in ODE	41
Table 2: Simulation Parameters	51
Table 3: Environmental Parameters	52
Table 4: Mass and Moment of Inertia.....	53
Table 5 : Mesh Comparison.....	57
Table 6: Point Absorber and VIS Connection Properties	61
Table 7: Drag Coefficients.....	70
Table 8: Natural Frequencies Under Different Constraints.....	70
Table 9: Parameters for use in impedance calculation. Physical origination comes from the 1/25 th physical model	81
Table 10: Froude Model Scaling	93
Table 11: Environmental Model Settings	94
Table 12: Kinematic Cases	95
Table 13: 1/20 th Scaled and Corresponding Full-scale Model Settings.....	127

List of Figures

Figure 1: a) Californian Energy production profile with duck curve, outlined in green, creating large ramp up and down periods for other form of generation at morning (blue line) and evening (red line) b) Energy Production profile without wind or solar for reference [13]	6
Figure 2: Available wave energy resource around the world, as determined by Gunn and Stock-Williams [14]	8
Figure 3: Monthly Modelled Wave Energy Transport (kW/m) at Amphitrite Bank, approximately 7 km offshore [17]	9
Figure 4: WEC Classification table graphic[20]	10
Figure 5: Wave energy converters a) Oyster b) CETO 6 c) Pelamis d) LIMPET	11
Figure 6: A Point Absorber (blue) connected to the seabed by a PTO represented with a parallel spring, fcg and damper fcf.	12
Figure 7: Self-Reacting Point Absorber composed of a Float (body 1) Spar (body 2), PTO and mooring lines	15
Figure 8: Wavebob SRPA WEC composed of two bodies and a PTO [28]	16
Figure 9: Two SRPAs for comparison in Beatty et al.’s work. The left being a close comparison for this works physical model [29]	17
Figure 10: Internal Mass-Modulation Scheme as conceptualized within the University of Victoria [36]	19
Figure 11: Working Physical Model	21
Figure 12: SRPA (datasets 1 and 2) and Geometrically Controlled SRPA (dataset 3) Power Capture Comparison with the Budal limit (dataset 4)	23
Figure 13: Wave Terms: wavelength is from crest to crest or trough to trough, wave height is the vertical distance from crest to trough, and positions x (with the wave propagation) and y (across the wave front) for waves are referenced from the center of orbital rotation while z is taken from the free surface is $z = 0$ as a wave passes. The displacement η is assumed to be nominal.	28
Figure 14: Linear Buoyancy Force	29
Figure 15: Two points in time as a wave propagates past a long vessel and changes the waterplane area	34

Figure 16: Righting Moment with center of gravity, metacenter buoyancy and roll angle for a buoyancy stabilized body.....	35
Figure 17: Variation of the righting moment through the movement of the waterline causing both a change in buoyancy force and moment arm, subscript indicates the higher waterline, h, and the lower waterline, l.....	36
Figure 18: A submerged cylinder exposed to an incoming wave.....	37
Figure 19: Mathieu Equation Test Case.....	43
Figure 20: Time Domain plot of the Mathieu Equation Test with a GM Variation of 25%	44
Figure 21: Example of panel based evaluation, if this cube was submerged the net buoyancy force could be evaluated by integrating the hydrostatic pressure over the surface	54
Figure 22: Circular shape represented by an octagon, this is an example of the top view of the Float represented by a mesh with eight radial segments.....	55
Figure 23: Physical geometry of Spar.....	55
Figure 24: Physical geometry of Float.....	56
Figure 25: Results of the chosen mesh in the time domain	58
Figure 26: Connection layout with corresponding numbers to Table 6.....	60
Figure 27: The full VISWEC and VIS with labeled bodies and connection numbers shown as a) physical model and b) ProteusDS model.....	62
Figure 28: Linearized Friction in VIS the blue lines are the experimental tests and the black line with red circles at the peaks are the ProteusDS simulations of the system. The plots are arranged by inertial setting (kg m^2) of the VIS.....	63
Figure 29: a) Froude Krylov Force coefficient over a span of frequencies b) Scattering Force over a span of frequencies.....	66
Figure 30: a) Added Damping coefficient and b) Added Mass coefficient for the Float and Spar in roll/pitch and heave over a range of frequencies	67
Figure 31: Rotational Limitation, as the width of a rotating body grows the approximation of path begins to not hold, if the body is discretized into panels each panel can be calculated with a linearized assumption [72].....	68
Figure 32: Heave decay plot of experimental results and that of the drag matching achieved through ProteusDS simulation	69
Figure 33: Mechanical Circuit Elements. Reproduced from [25].....	73

Figure 34: 3-Body SRPA Circuit Impedance reduced using Thevenin’s theorem where body 1 is the Float and body 2 is the Spar [25]	75
Figure 35: 2- body SRPA Circuit Impedance [25]	76
Figure 36: Single body point absorber circuit impedance [25].....	77
Figure 37: Conversion of a typical Thévenin’s Theorem [25]	77
Figure 38: Linearized drag coefficients of each body determined by three different velocities over a span of frequencies.....	84
Figure 39: PTO values from different considerations for a drag term within the analytical solution for optimal PTO	85
Figure 40: PTO values from different considerations for a drag term within the analytical solution for optimal PTO	86
Figure 41: Power sensitivity (color) to PTO value with refined optimal PTO (x) and the chosen PTO value from consideration of linearized drag using water velocity (-)	87
Figure 42: Optimal inertial setting for geometric control configuration	89
Figure 43: Optimal PTO values for both configurations	89
Figure 44: Histogram of significant wave height and period at Amphitrite Bank off the west coast of Vancouver Island [17].....	92
Figure 45: Histogram of significant wave height and period at Amphitrite Bank off the west coast of Vancouver Island [17] with the tested value range expressed as a box.	94
Figure 46: Time domain plot of the VISWEC at a frequency of 2.5 rad/s and wave height of 0.3 meters. The top showing position, middle orientation and bottom of relative velocity between the Spar and Float. The position/orientations are blue for surge/roll red for sway/pitch and yellow for heave/yaw.....	96
Figure 47: Visualization of the calculation of tipping magnitude	97
Figure 48: Heave Only a) 2-body and b) 3-body results	99
Figure 49: 2-body Heave and Roll Only a) Power Production and b) Rolling Magnitude	101
Figure 50: 3-body Heave and Roll Only a) Power Production and b) Rolling Magnitude	103
Figure 51: 2-body Moored a) Power Production and b) Tipping Magnitude	105
Figure 52: 3-body Moored a) Power Production and b) Tipping Magnitude	107
Figure 53: 2-body Unconstrained a) Power Production and b) Tipping Magnitude	109
Figure 54: 3-body Free case results of a) Power Production and b) Tipping Magnitude.	111

Figure 55: Comparison of 2-body power production in Watts between the Heave only case and Heave and Roll case, green shows where the Heave Only out performs Heave and Roll and red shows the contrary. 113

Figure 56: Comparison of 2-body a) power production in Watts between the Heave only case and Moored case and b) tipping magnitude in meters between the Heave and Roll case and Moored case, Green shows where the Moored values are larger, red shows the contrary. 114

Figure 57: Comparison of 2-body a) power production in Watts between the Heave only case and Free case and b) tipping magnitude in meters between the Heave and Roll case and Free case, Green shows where the Moored values are larger, red shows the contrary..... 115

Figure 58: Comparison of 3-body power production in Watts between the Heave only case and Heave and Roll case, green shows where the Heave Only out performs Heave and Roll and red shows the contrary. 117

Figure 59: Comparison of 3-body a) power production in Watts between the Heave only case and Moored case and b) tipping magnitude in meters between the Heave and Roll case and Moored case, Green shows where the Moored values are larger, red shows the contrary. 118

Figure 60: Comparison of 3-body a) power production in Watts between the Heave only case and Free case and b) tipping magnitude in meters between the Heave and Roll case and Free case, Green shows where the Moored values are larger, red shows the contrary..... 119

Figure 61: Comparison of the 2-body and 3-body power productions in Watts. Red shows where the 2-body system outperforms the 3-body system and green shows the opposite. 120

Figure 62: Comparison between the 2-body and 3-body systems Heave Only case of a) power production in watts and b) tipping magnitude in meters. Green areas show where the 3-body system values are greater than the 2-body system. 121

Figure 63: Comparison between the 2-body and 3-body systems Moored case of a) power production in watts and b) tipping magnitude in meters. Green areas show where the 3-body system values are greater than the 2-body system. 122

Figure 64: Comparison between the 2-body and 3-body systems Free case of a) power production in watts and b) tipping magnitude in meters. Green areas show where the 3-body system values are greater than the 2-body system. 123

Acknowledgements

I would like to extend a great thanks to everyone who helped me with the completion of this thesis. A particular thank you to Dr. Helen Bailey, for her patients, reviews and endless support through the execution and understanding of the software used within. A thank you to Dr. Bryson Robertson for his belief and support in me throughout even the roughest times. A shout out to my colleagues and friends in WCWI and IESVic as a whole. Most importantly a special thank you to Dr. Brad Buckham whom I have the utmost respect and admiration for, thank you for your constant understanding, support and guidance during my time here.

On a personal level I would like to thank my father, mother and step-mother for their ceaseless support, understand and selflessness; you have taught me how to be the man I am that brought be here today. To my friends, scattered around the US and other countries for your support and couch when I needed some time away. You all provide me with the means and motivation to continue my pursuit of knowledge.

This work was funded by the Natural Sciences and Engineering Research Council of Canada.

Dedication

To my mother, who supported me leaving to further my education with the knowledge that it would sacrifice her limited time left with me. This one's for you and me Mama Bear, I miss you.

Nomenclature

Latin Variables		Greek Variables	
a	Constant in Mathieu Equation	α	Half the wave height
A	Added mass	β	Response parameter
A_{proj}	Projected Area	γ	Pumped parameter
A_0	Original cross sectional area	Δ	Change
c	Hydrodynamic stiffness	η	Wave free surface
c_k	Structural stiffness	θ_a	Roll amplitude
d	Depth	θ_{mag}	Roll magnitude
D	Added damping	θ_w	Wave phase
D_q	Quadratic drag coefficient	θ_x	Roll angle
D_l	Linear drag coefficient	κ	Wave number
F_b	Hydrostatic buoyancy force	λ	Wavelength
f_{cf}	Dampener	Λ	Scaling number
f_{cg}	Spring	π	Mathematical constant pi
g	Gravity constant	ρ	Density
\overline{GM}	Distance from G to M	τ_{mag}	Tipping magnitude
\overline{GZ}	Distance from G to Z	ϕ_a	Pitching amplitude
h	Wave height	ϕ_{mag}	Pitching magnitude
H	Draft	ϕ_y	Pitching angle
I_{xx}	Roll moment of inertia	ϕ_0	Initial phase offset
m	Mass	ω_e	Excitation frequency
M	Metacenter	ω_n	Natural frequency
M_θ	Righting moment in roll	ω_{rat}	Frequency ratio
p	Undisturbed wave pressure		
P	Power		
q	Constant in Mathieu Equation		
t	Time		
x	Position axis		
y	Position axis		
z	Position axis		
Z	Intersection point on z-axis		
z_B	Location of buoyancy on z-axis		
Z_{eq}	Equivalent impedance		
Z_{Meff}	Effective mass impedance		
Z_{PTO}	PTO impedance		
Z_i	Body impedance		
\dot{z}_{rel}	Relative heave velocity		

Acronyms

CSP	Concentrated Solar Power
DoF	Degree of Freedom
GC-SRPA	Geometrically Controlled Self Reacting Point Absorber
NREL	National Renewable Energy Lab
PTO	Power Take-Off
PV	Photovoltaic
SBPA	Single Body Point Absorber
SRPA	Self Reacting Point Absorber
SWAN	Simulating Waves Numerically
UVic	University of Victoria
VIS	Variable Inertia System
VISWEC	Variable Inertia System Wave Energy Converter
WAMIT	Wave Analysis Massachusetts Institute of Technology
WEC	Wave Energy Converter

Chapter 1 Introduction

1.1 Motivation

In a world seeking to harvest power from renewable sources, wave energy remains a largely untapped renewable resource. In addition to ocean waves being relatively difficult to access relative to land based renewables, a reason for the lack of commercial wave energy technologies is that there are a plethora of ways in which energy can be extracted from a propagating water wave resulting in a lack of convergence on a single design.

Wave energy can be harnessed using the kinetic energy of the fluid driving a power conversion process, the alternating free surface that exerts a powerful fluctuating buoyancy force, the pressure oscillations beneath the free surface, the overtopping of waves directed through a turbine and combinations of the previously stated. With the multitude of concepts being investigated, each having their advantages and disadvantages, there is a resulting difficulty determining a single optimal design.

This work is focused on a particular class of wave energy technology - the point absorber. A point absorber is a surface piercing device comprised of one or more floating bodies that are driven by the fluctuating buoyancy force as a wave passes. Advantages of the point absorber are that it can harvest energy from waves arriving at the site from any direction, and that its dynamic response can be *tuned* to any wave climate; that is, the frequency at which the point absorber components naturally oscillate can be *tuned* to suit the collection of wave periods that exist at the location and time. However, point absorbers have also been demonstrated to suffer from an instability in their dynamic response at some wave frequencies that compromises power production performance. This work aims to present a clear description of the source of the instability, and explore the implications of a proposed tuning method on a point absorber's dynamic response including the tendency of the method to mitigate or exacerbate the instability.

1.2 Wave Energy Background

1.2.1 Historical Developments

In the Information Age, global society faces an energy predicament. As nations seek to participate in a largely electrically driven economy, there is an increasing demand for electricity generation. Simultaneously, climate change mitigation is motivating a decarbonization of the world's energy systems. It is widely accepted that for both ambitions to be realized renewable energy technologies need to be adopted and widely implemented. However, when considering energy systems on a global scale no single renewable option will be the sole solution. Between different locations the abundant local renewable changes. For coastal jurisdictions at higher latitudes wave energy is the predominant renewable option and thus Wave Energy Converter (WEC) devices are a necessary entry in the technology portfolio that will lead our world to cleaner energy production.

Utilizing wave energy is not a new concept. Centuries before electricity became the dominant energy commodity, humans were harvesting the power of wind and running water to grind grain and pump water. By the mid 1700s the innovative coal powered steam engine was getting established and in 1880 Thomas Edison attached it to an electrical generator, providing Wall Street with centralized electricity. About a year later in 1882, a hydroelectric generator was launched on the Fox River in Appleton Wisconsin, the first major renewable energy generation. Only a decade later, the first WEC patent was filed in the United States [1]. But while WEC concepts date back to the beginning of centralized electricity production, it still remains today to find ways to harness wave energy at commercially competitive costs.

In the broader context of ocean energy research and development (including wave, tidal and offshore wind), developments have been primarily motivated by spikes in the cost of fossil fuels, resulting increases in domestic energy unit costs and subsequent concerns on energy security. Recently in Nova Scotia, coal price volatility aided a political push towards renewables such as tidal in order to stabilize the cost of energy [2]. In the 1970s there was a surge of research into renewable energy, unfortunately, this push would subside as the price of oil decreased once again. Out of this push came advances in ocean wave energy conversion, mostly but not exclusively in the United Kingdom because they continued research after the oil price decrease while the United States drove more towards solar. Major contributions in ocean energy were from researchers such as Salter, Budal and Falnes [3], [4]. These events reflect that conventional

thermal energy generation could be compromised by supply or poor political relations with exporting countries, and that energy generation needs to be diversified to be more stable.

Since the 1970s, Sweden has been steadily eliminating fossil fuel usage within their borders by investing in alternative forms of energy production such as, but not limited to: solar, wind and hydroelectric energy production in conjunction with increasing energy efficiencies of all aspects of their country [5]. Scotland produced the equivalent of 97% of their household electricity needs with wind power in 2015 with a total renewable electricity generation contribution of 26% to the UK [6], [7]. Hydroelectric, geothermal, wind and solar made up almost 99% of Costa Rica's electrical needs in 2015, with 250 days of 100% renewable energy production to the national grid [8]. Even the world's largest carbon producer, China, has been installing wind and solar farms committing to phasing out coal and pollution [9].

With increased awareness and concern of the impact of humans on the earth, combined with an urge for energy security and continued increases in power demand, clean renewable wave energy production has become a topic of focused worldwide research once again [10]. Groups charting a path for a 100% renewable energy future, task wave energy with a 0.37% or 5.85 GW, of the United States of America energy production portfolio by 2050; this compares to wind and solar at 50% and 45% respectively. Jacobson et al. mention that the available resource is about 23 times the purposed power delivered, 5.85 GW, and no single state's capacity for wave energy utilization is over 1% of the overall portfolio [11]. This is a proportionate amount considering the state of wave energy today, having no commercial installations.

In contrast to wave energy devices, renewable technologies such as wind and solar are maturing and penetrating electricity grids in developed countries. Now is the time for wave energy technology to make the advancements needed to bring it to a fully commercially viable state. To get to the commercial state, the pros and cons of each class of device need to be fully understood so power project developers can make an informed selection of a technology and then focus resources on technology readiness – building the supply chain, manufacturing process and operating procedures to reduce the cost of production.

1.2.2 The Need for Diversity in Renewables

Each current form of power generation has unique characteristics. Coal power plants are able to produce large amounts of energy but cannot change their power output quickly. Liquid natural gas and combined cycle gas plants are able to quickly start up and change their output but

tend to have a smaller capacity than most traditional non-renewable power sources. Hydro-electric plants need to have a minimum output at all times but can have the flexibility to ramp up and down quickly as well as in some cases pump water back up to store energy. This can be very useful as it provides flexibility without relying on a carbon producing generator. Renewable sources such as wind, wave and solar are geographically and temporally constrained: they are physically located where the resource exists and they are subject to the variability of the natural process supplying the energy. Given the limitations of energy storage technologies, surplus renewable power must be used when it is delivered. As the capacity of any one form of renewable energy generation is built out, the consequences stemming from the intermittency of that renewable are heightened.

While wind and solar energy technologies are already major contributors to renewable energy portfolios in many North American jurisdictions, wind power has been proven difficult to integrate due to large and unpredictable ramping events, while solar power is susceptible to interruptions due to cloud cover and precipitation [12]. The National Renewable Energy Lab (NREL) did a test study of a largely diversified power system portfolio with solar and wind encompassing 48% of the total 111 GW generation as part of an investigation for the integration of wind and solar into USA's power grid [13]. Outlined in green, Figure 1 shows the contribution to the electricity portfolio from solar, both Photovoltaic (**PV**) and Concentrated Solar Thermal Power (**CSP**); this contribution is commonly referred to as a "Duck Curve". The Duck Curve highlights a rapid increase and decrease of solar energy generation in the morning and evening, respectively. Since the grid must accept the solar energy as it is delivered, other sources of generation, in this case "Gas CC", must ramp down in the mornings and up in the evenings to balance demand as well as be kept on stand-by in case solar or wind energy cannot perform (i.e. cloudy day). Ramping events, particularly for coal fired plants, have to be stretched out over longer periods of time resulting in excess energy being supplied to the grid and not used productively, shown as the power production below zero on the y-axis. Consequently, if power supplies cannot ramp up fast enough the supply is not met and customers do not receive the power they need.

In comparison to the time scales of the variabilities of wind and solar energy, wave energy has been shown to vary on longer time scales and has greater predictability which makes it a more reliable, predictable source of power production. Reikard et al., analyzed the integration of

wave energy with wind and solar in the Pacific Northwest on the timescale of a day and a year. They found wave energy production to be generally “smoother” not suffering from large ramp up and ramp down events as well as being more predictable than solar or wind on a 1-hour forecast [12].

Based on the lessons learned to date in the build out of large scale solar energy, it is evident that a diversity of renewable options is needed – a mix of different renewable supplies with distinct temporal characteristics over a large geographic area is needed to consistently balance energy demand without creating added stresses on conventional thermal based generators. Given that wave energy has a naturally slower energy transport, not following the wind and solar cycles, it will certainly provide a balancing role in the mix of renewables.

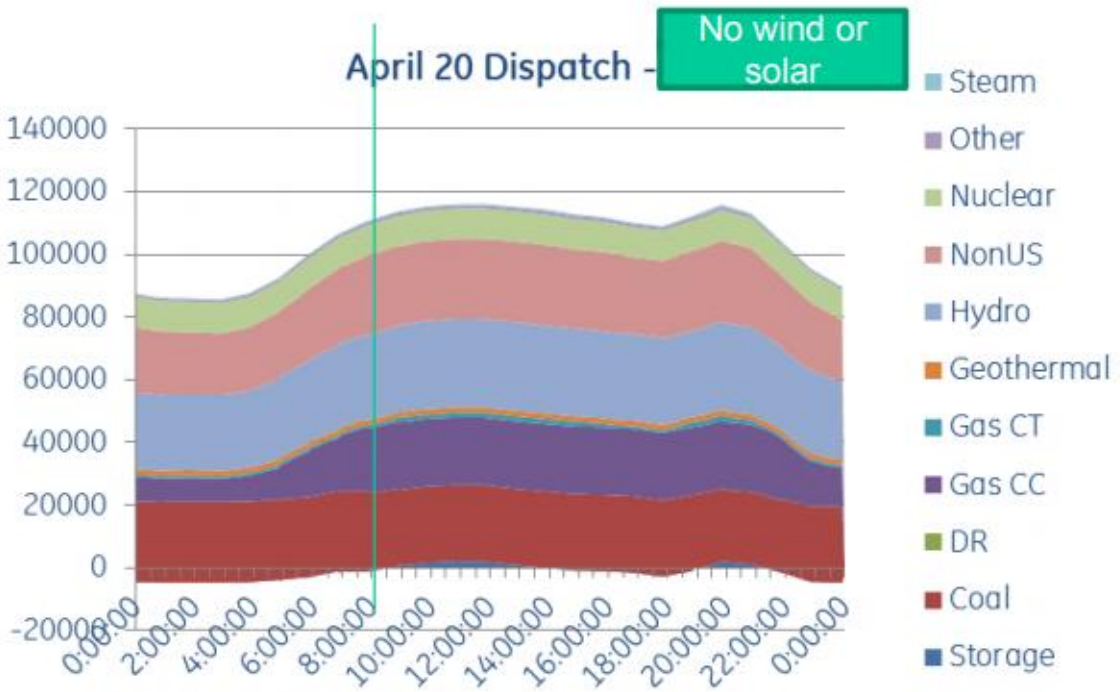
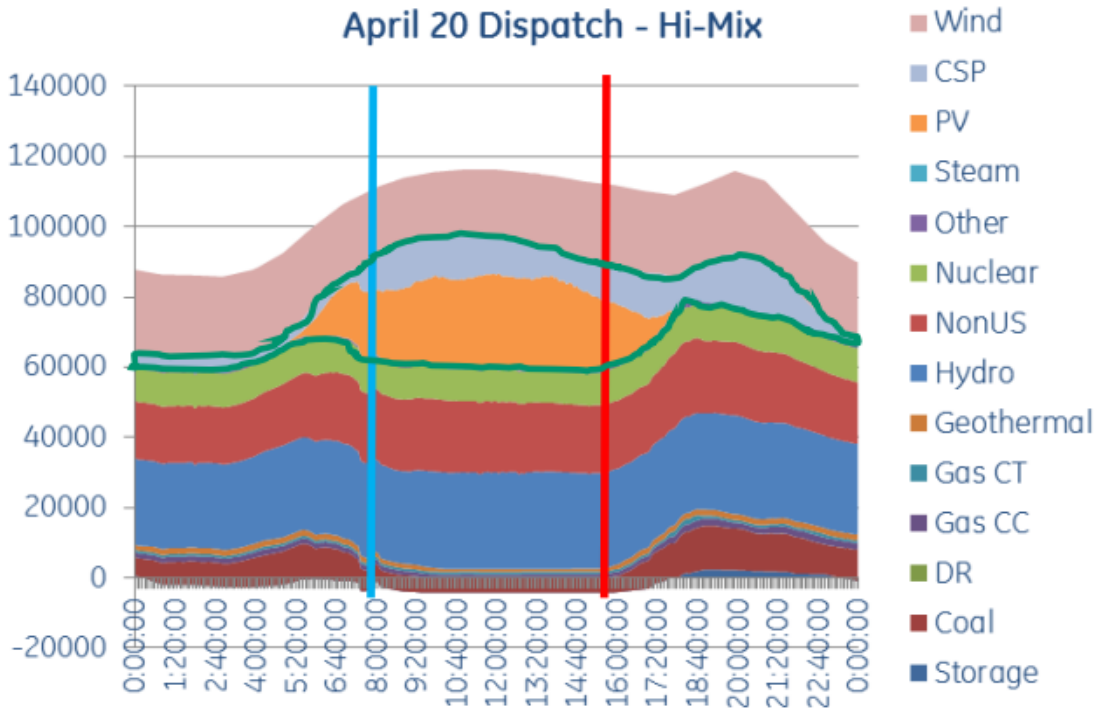


Figure 1: a) Californian Energy production profile with duck curve, outlined in green, creating large ramp up and down periods for other form of generation at morning (blue line) and evening (red line) b) Energy Production profile without wind or solar for reference [13]

1.3 The Wave Energy Resource

Although wave power has yet to be utilized for generating electricity on a large scale, the raw untapped resource available is large, typical estimates suggest 2.11 TW of resource worldwide [14]. The amount of available wave power per meter, shown in Figure 2, has been estimated for coastlines across the globe. Areas of interest include areas in the mid-level latitudes where the energy demand and the wave energy resource are correlated on a seasonal basis [14]. While Figure 2 gives a global view of the regional total amount of power that is available, it does not provide information on the quality of the wave resource, this requires a local wave resource assessment.

There are many ways to model the nearshore wave field of a localized zone. There are two classes of near shore wave model – ‘phase resolved’ and ‘phase averaged’. Phase resolved tracks the wave specific properties throughout an area. Phase averaged models do not track the specific phases of the propagating water waves that comprise the sea surface. Rather, they track the evolution of the wave spectra from model grid point to grid point. As a spectrum is strictly defined by the total variance in surface elevation change within a set of frequency bins, these models are referred to as ‘Spectral action density models’ where spectral action density is simply variance with an assumed uniform probability distribution for phase [15]. Relative to phase resolved models, spectral action density models require much more reasonable computational resources while providing adequate output data for analysis of the raw wave energy resource and the performance assessment of deployed WEC devices. These resource models are capable of representing most waves including shallow waves, interactions between waves, wind effects and are used to calculate wave transformations over large areas in order to find accurate wave conditions near shore [16].

Robertson et al., created a higher fidelity model for a localized region close to shore [17]. The method used a Simulating WAVes Nearshore (**SWAN**) model to create a temporal and spatial representation of the waves off the west coast of Vancouver Island. This SWAN model is a coastal modelling tool that can provide the wave conditions over a large geographic area with knowledge of the wave condition at a few boundary locations. This coastal model was found to have a higher correlation in a hindcast model when compared to measured data [17]. Robertson et al., also compared the results to a previously published paper by Cornett and Zhang which agreed with a near shore evaluation but compared poorly on the location further from shore [18].

The results from Robertson et al.'s is shown in Figure 3 as a line plot and the comparison shown as a bar graph. The large amount of wave resource more than warrants development of WECs, especially when considering the temporal aspect of the resource.

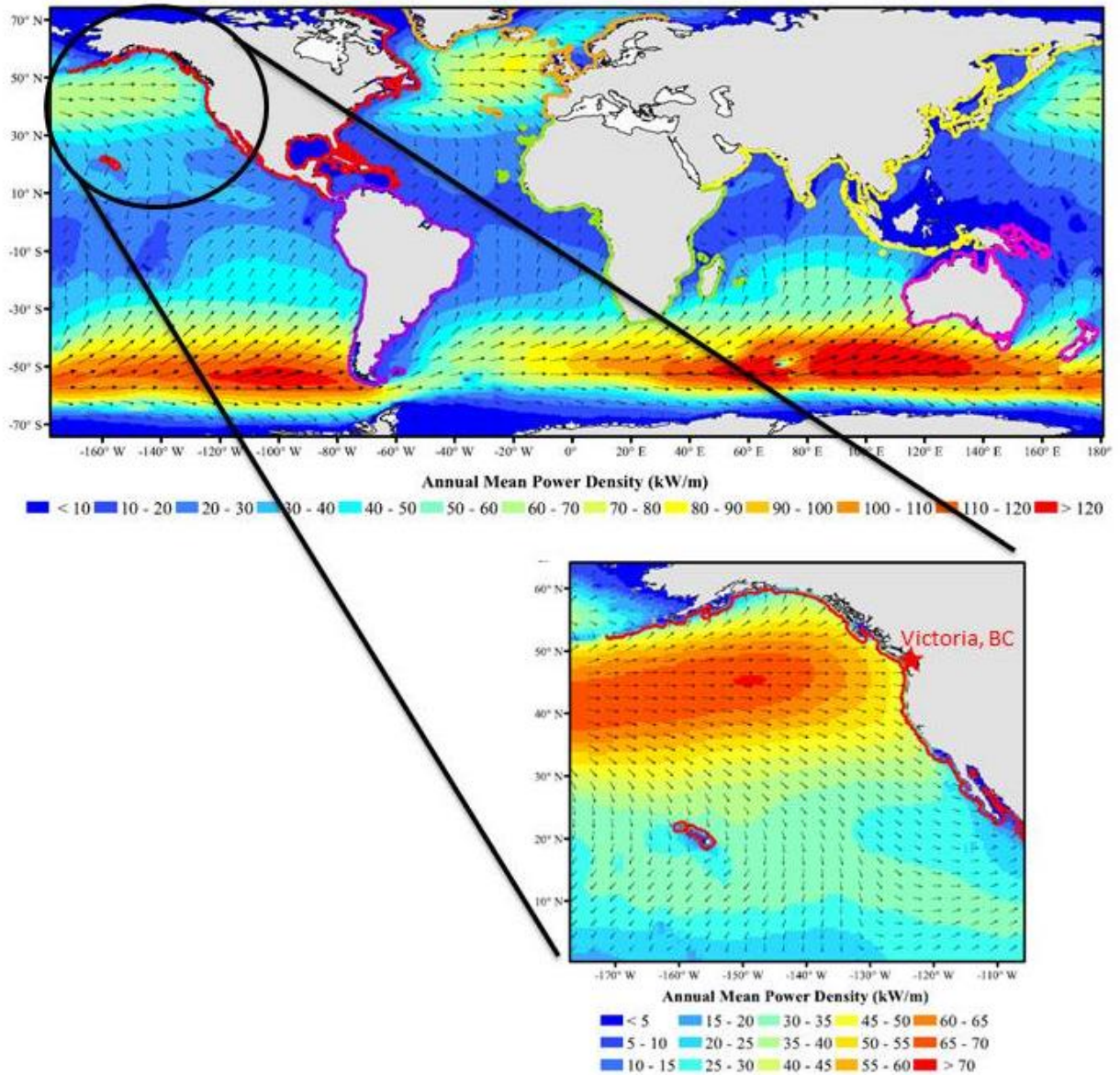


Figure 2: Available wave energy resource around the world, as determined by Gunn and Stock-Williams [14]

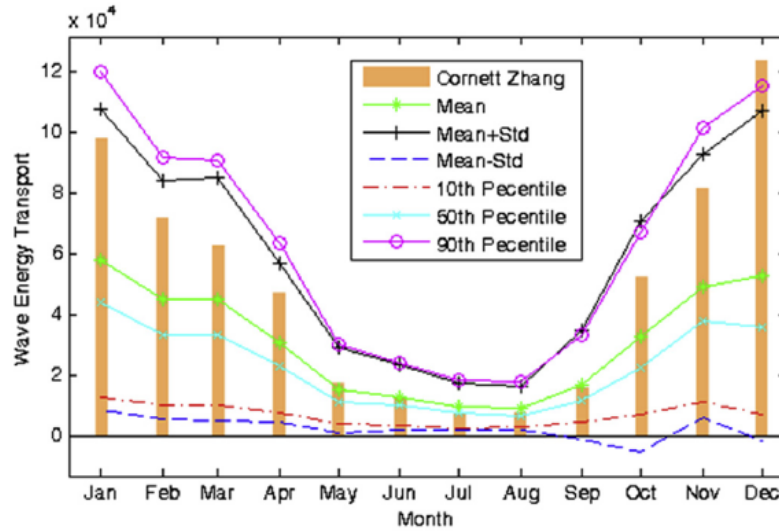


Figure 3: Monthly Modelled Wave Energy Transport (kW/m) at Amphitrite Bank, approximately 7 km offshore [17]

1.4 Wave Energy Converter Classifications

A WEC is a moving articulated multi-body system that is driven by an oscillating force exerted by the collection of wave energy propagating through the deployment site. A power-take-off (PTO) converts the kinetic energy into a transportable energy commodity. Wave energy converters have not converged to a single predominant design concept and several different WEC categorizations or ‘types’ have been proposed. Each type uses a different characteristic as the basis for differentiation; example being the geometry of the WEC, the operating principle (e.g. the physical mechanism through which the energy is extracted), the mode of motion that is driven by the wave, the energy commodity produced, and more. Here, classification is made according to WEC geometry and operating principle.

WECs classified by geometry fall into 3 major categories: point absorbers, attenuators and terminators. Point absorbers are typically axisymmetric about the vertical axis and have a small diameter in comparison to the incident wavelength. Attenuators are approximately the same length as the incident wavelength and are deployed perpendicular to the primary direction of waves. Terminator devices are a similar size to attenuators although they are deployed parallel to the incident wave front, this category includes shore based WECs and breakwaters [19]. This categorization can be seen by the color code in Figure 4.

In the context of operating principles, floating structures are positively buoyant wave activated bodies that are excited by the incident wave and power is created using a PTO that

reacts against the WEC motion. Oscillating water column type devices use an internal ‘moon-pool’ free surface to drive compression of a trapped air volume which subsequently is fed to a turbine. Overtopping devices are WECs that channel the surging motion of a wave crest overtop a structure that directs the water through a turbine. WECs can also operate off of the pressure differences as a result of a passing wave or take advantage of the oscillating surging motion of the waves. Each of these categories are noted by the columns of Figure 4.

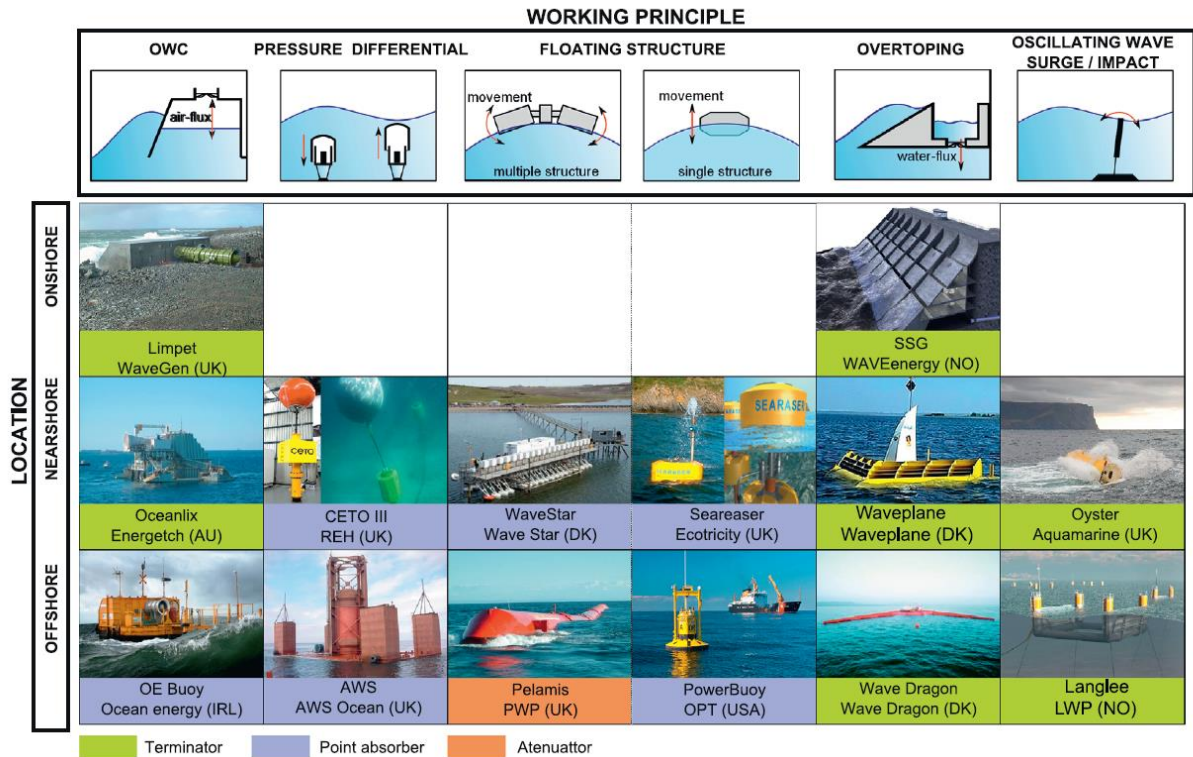


Figure 4: WEC Classification table graphic[20]

There are various pre-commercial variants of each of these basic WEC types. Some of the more well-publicized converters are the Scottish Pelamis terminator, the Australian Carnegie CETO point absorber, the UK based Aquamarine Power Oyster surging flap device and the LIMPET shore based oscillating water column - all shown in Figure 5.

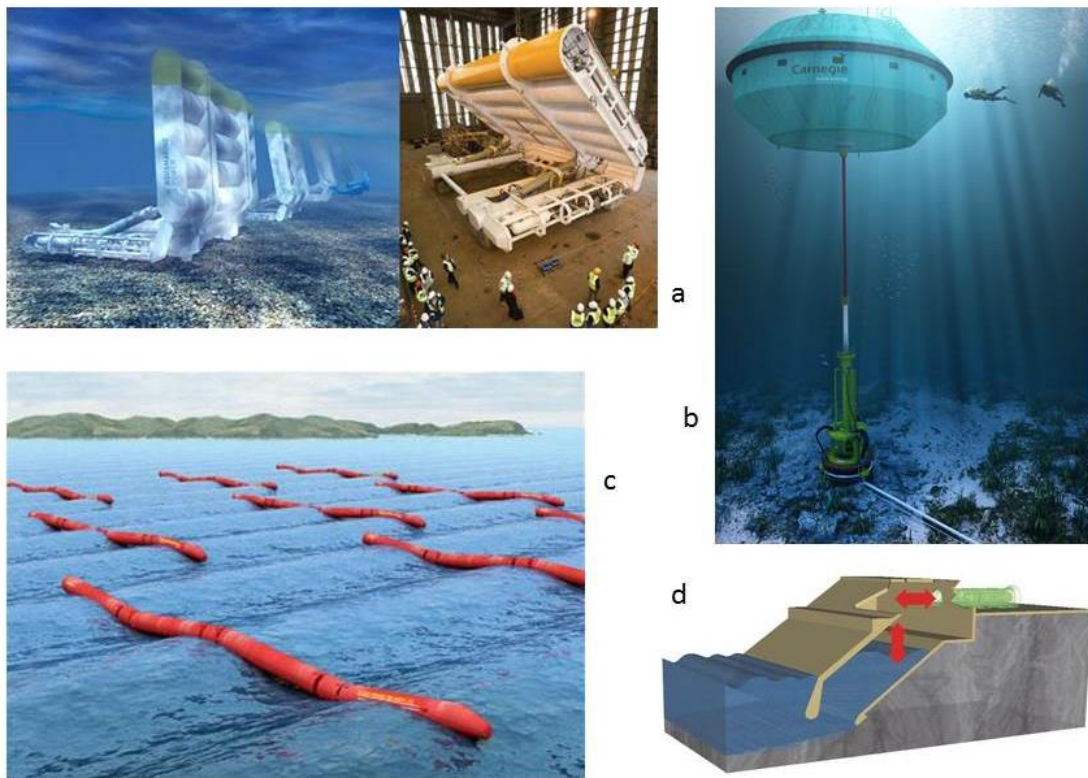


Figure 5: Wave energy converters a) Oyster b) CETO 6 c) Pelamis d) LIMPET

1.5 Point Absorbers

This research will focus on the dynamics of heaving point absorbers. Point absorbers are a predominant class of WEC: approximately 72% of current WEC designs fit within this class [21]. The dominance of point absorbers in the WEC design space is due to two performance advantages: point absorbers can extract energy from waves coming from any direction [22], and they can be designed to exploit system resonance. At resonance, a mechanical oscillating system is forced at a frequency that matches twice the natural frequency of the system and experiences growth in the oscillation amplitude that is only limited by the strength of any damping elements in the system. Energy extraction is accomplished by the dampening component within the PTO, shown in Figure 6 as f_{cf} which affects the amplitude of oscillation. The spring component, f_{cg} , provides an opportunity to *tune* the WEC to resonate at the wave excitation frequency, controlling the phase of the oscillation; with this the power output could be maximized due to the

increased motion [23]. This idealized representation of a PTO is common throughout a broad collection of existing literature [23]. While a point absorber can be designed to achieve resonance at a particular wave frequency through proper choice of float geometry, achieving this condition at different frequencies requires a way to actively modulate physical properties of the system to create changes in the natural frequency. This modulation is one form of Point absorber control, geometric control.

As can be seen in eq. (1.1), natural frequency, ω_n , depends on the mass of the system, m and the structural stiffness, c [24]; in the case of Figure 6 this is the spring stiffness or the hydrostatic stiffness of the buoy, discussed more in the linear wave theory section. To change the natural frequency through geometry, a change in mass or hydrostatic stiffness is necessary; mass being the easier of the two as the physical geometry of the system does not change.

$$\omega_n = \sqrt{\frac{c}{m}} \quad (1.1)$$

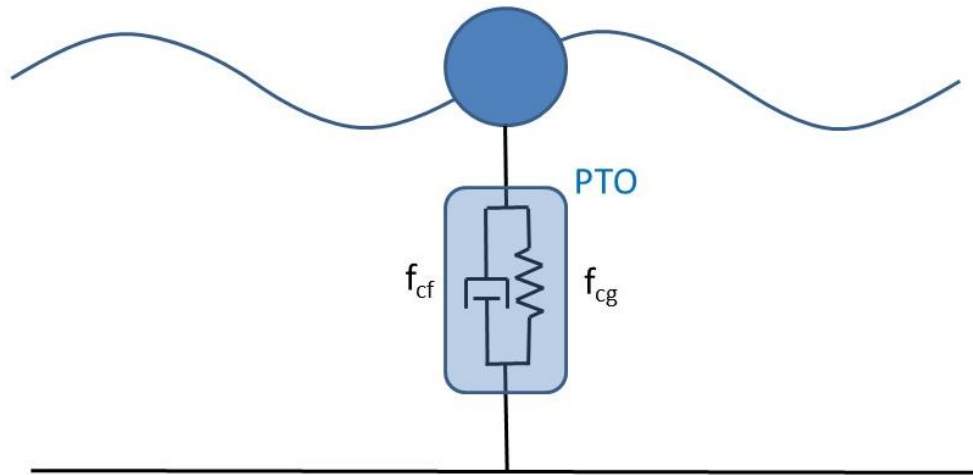


Figure 6: A Point Absorber (blue) connected to the seabed by a PTO represented with a parallel spring, f_{cg} and damper f_{cf} .

WEC control can be categorized into two categories, geometry control and PTO control. Power-take-off control is the active variation of the force in the PTO through modulation of the stiffness, f_{cg} , and damping parameters, f_{cf} . The goal of PTO control is to control the spring and dampening forces affecting the phase and amplitude respectively to maximize power capture

[25]. Geometry control is the active variation of a physical parameter of the WEC structure. The goal of geometry control is to produce a resonance in the system, and for the case of the point absorber in Figure 6, this would be a change in the mass, or diameter of the blue float. For the simple point absorber shown in Figure 6, the separation of roles in geometry and PTO control is arbitrary. As an example, the spring stiffness element in the PTO could be used to manipulate the system natural frequency just as changing the float geometry would, and in fact could be a simpler method to accomplish a change in natural frequency. However, for other more complicated point absorber topologies, or *architectures*, this overlap in functionality is not present and the two control methods serve distinctly different roles.

In this thesis, the focus is on a specific point absorber *architecture*: the Self-Reacting Point Absorber (**SRPA**) with an internal geometry control mechanism. Below, the progression from the point absorber design of Figure 6 to the SRPA with geometry control (**GC-SRPA**) is described.

1.5.1 Single Body Point Absorber (SBPA)

Single Buoy Point Absorbers (**SBPA**), shown in Figure 6, are required to be referenced with the ocean floor and are simpler systems due a single body system. This is one of the earliest WEC *architectures*, Johansen filed for his patent in 1982 with a buoy that would pull a rope on its upstroke that spun an onshore machine [1]. The SBPA is a single float connected to the sea floor via a tension member. The PTO is connected to that tension element at the seabed or onshore if the tension element is routed to shore via a pulley. Due to the taut element connecting the float to the seabed, an SBPA is referred to as a ‘bottom-referenced’ device. The SBPA concept was modernized and implemented by Carnegie Energy, shown in Figure 5b, where a single large float is connected to the sea floor through a hydraulic PTO. Since the PTO in this type of point absorber must act dually as a means of power extraction and a means of mooring, it can experience large loads.

The PTO control in an SBPA aims to maximize efficiency through the control of the forces within the PTO, the main mechanism for controlling the response of the system. Hals et al., outlined and compared a selection of control options all incorporating a way to inject and/or extract energy to/from the system. Strategies include basic resistive loading or a force proportional to velocity, complex conjugate control which uses a controlled resistive load

coupled with a controlled way to inject energy back into the system such as a controllable spring. Approximate velocity tracking control aims to achieve an optimal velocity through force control of the PTO. Finally, latching and clutching control are two control techniques applied within the PTO which involve sudden and sizable changes in the PTO resistance that delay motion of the float such that the phase angle between the wave excitation force and the float velocity is eliminated [26]. Therefore, the wave forces on the body increase until the optimal time to release, characterized by the PTO, so that the work completed by the wave on the body is maximized in the following moments.

1.5.2 Self-Reacting Point Absorber (SRPA)

When a WEC is to be deployed off-shore, water depths can extend past the feasible range of a bottom-referenced point absorber; a SRPA's niche is located at these depths. SRPAs are more complex due to the two bodies reacting against each other but have the benefit of functioning in large depths with a cost effective mooring system. An SRPA is able to extract energy through the relative movement of two bodies while being held on station through the use of 'slack' mooring lines. The two hull components, shown in Figure 7, of an SRPA are articulated rigid bodies that are both subjected to wave forces. Due to differences in body hydrodynamics where the float follows the free surface elevation and the spar directly opposite, they naturally tend to move out of phase providing force for the PTO to extract energy from.

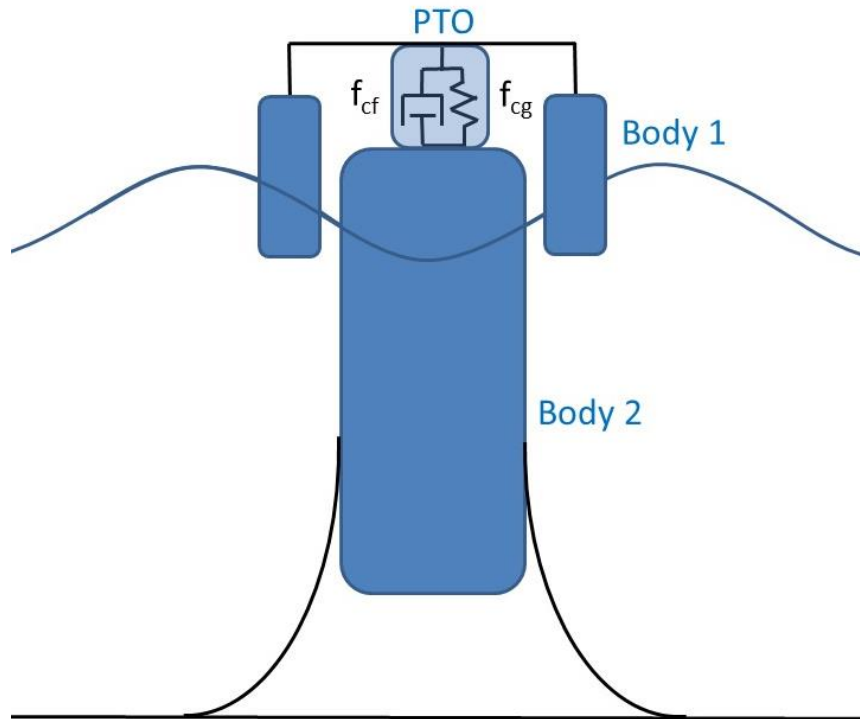


Figure 7: Self-Reacting Point Absorber composed of a Float (body 1) Spar (body 2), PTO and mooring lines

Since the force across the PTO is delivered by the two separate bodies, the forces transferred to the mooring lines are significantly reduced relative to the SBPA designs. As such, the costs of deployment can be reduced due to the reduction of material needed to secure it to the sea floor. Additionally, this type of mooring naturally corrects for tides by providing excess scope in the mooring lines. Wavebob sought to utilize the SRPA *architecture* with their patent, shown in Figure 8, and researched different possibilities for system control [27], [28].

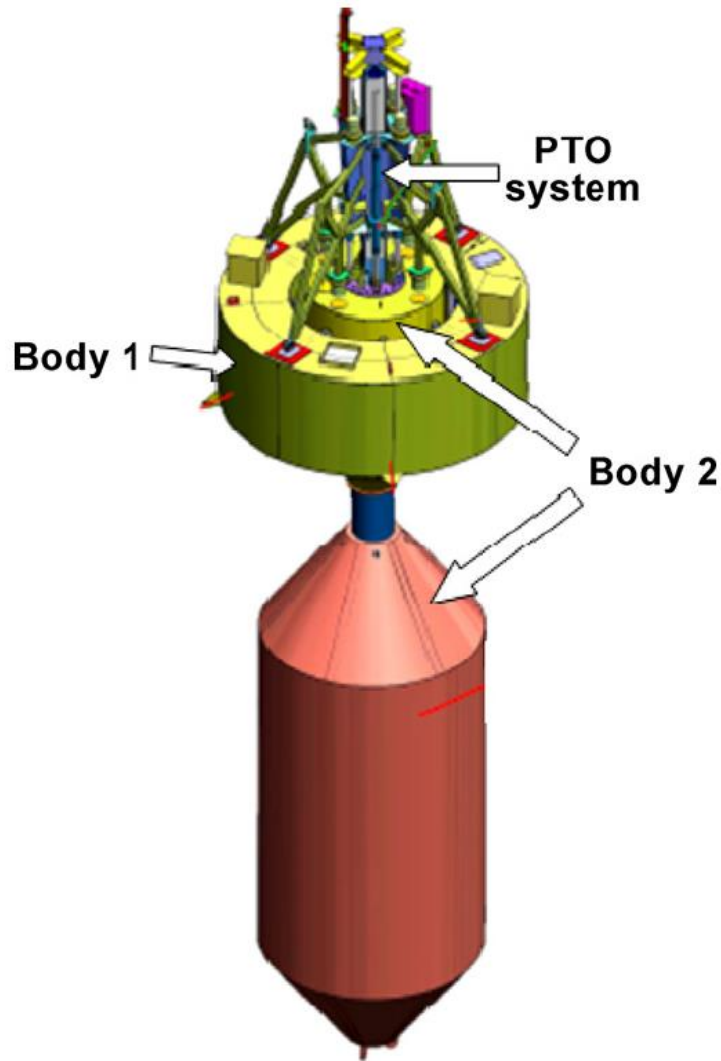


Figure 8: Wavebob SRPA WEC composed of two bodies and a PTO [28]

Beatty et al., compared two geometrically different SRPAs, one similar to Wavebob's to be the baseline of comparison for the WEC tested in this work, and one with a large dampening plate on the bottom, shown in Figure 9 [29], [30]. Both Wavebob's and Beatty et al.'s work aimed to maximize power extraction by controlling the PTO without changing the geometry of the structure. Power-take-off control is ultimately determined by the geometry of the bodies present in the system. These techniques work well with monochromatic waves but have difficulty being *tuned* to extract optimal power from multiple frequencies simultaneously such as a polychromatic state, typical natural sea states.

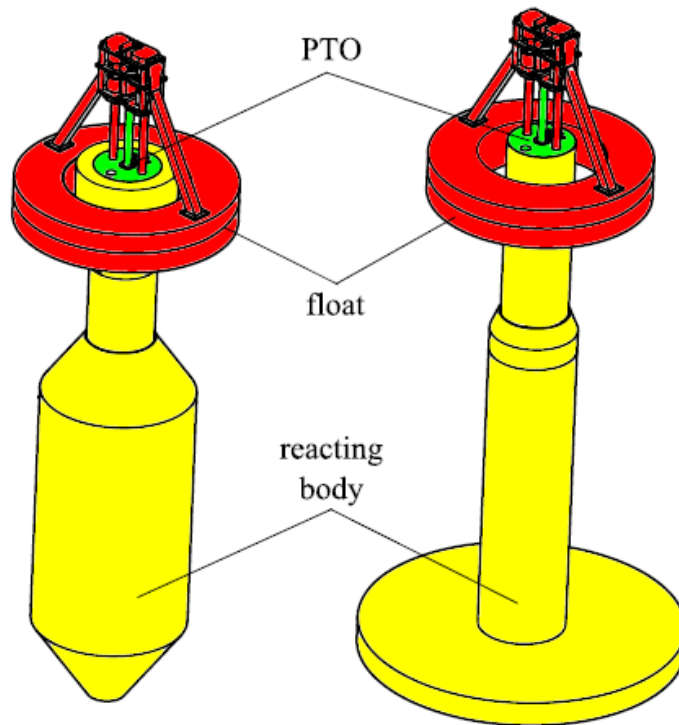


Figure 9: Two SRPAs for comparison in Beatty et al.'s work. The left being a close comparison for this work's physical model [29]

While the same control principles of SBPAs are extended to SRPA devices, the control problem is more complicated as there are 2 bodies and more opportunities to inject impedance and reactance into the system. To allow for SBPA control principles to be applied to the SRPA *architecture*, Falnes was able to simplify the SRPA dynamics down to a form that was equivalent in structure to those of an SBPA system [23]. In his process, the physical specifications of the SRPA components combined to form the equivalent buoyancy, and mass properties of the equivalent SBPA. Depending on the design of the two hull components, SRPAs present an opportunity to exploit two resonant modes of oscillation, one for each body, thus creating the opportunity to achieve better power conversion performance across an expected range of wave frequencies. Although more challenging an SRPA has the potential to achieve a higher power output compared to an SBPA [31]. Bubbar explored the upper limit of SRPAs and found that maximum power production from an SRPA was the sum of each body as if each were an SBPA with the same PTO [25].

1.5.3 Geometrically Controlled SRPAs (GC-SRPA)

Oscillating systems, such as point absorbers, are known to operate at their highest efficiency when operating in resonance. When the frequency of the incoming wave matches the natural frequency, an increased amount of motion is experienced, increasing the efficiency of the system [32]. Geometric control of a SRPA, for the purpose of this work, aims to vary the natural frequency of the Spar in order to achieve a high efficiency.

Geometric control changes the mechanical properties of the Spar and PTO control is dependent on those mechanical properties. Since geometry control adjusts the natural response of the system, it is considered a precursor to PTO control. As such, there is a *master-slave* relationship between the two modes of control: geometry control being the *master* and the implementation of the PTO control being dependent, or *slave*, to the changes in mechanical properties realized at the geometry control stage [25]. The coordination of the *master-slave* relationship makes GC-SRPAs the ultimate challenge in WEC design. The background for the GC-SRPA *architecture* used in this work is provided in the sections below.

Wavebob

This work will perform tests on a geometric control mechanism inside the Spar in an SRPA. Similar work can be observed in publications from the WEC developer Wavebob and the University of California Berkley where they both used a method of trapping water or air to change the *effective mass*, or the observed WEC mass response to wave excitation of the system [27], [33]–[35]. Orazov et al. numerically modeled the design from Wavebob [27] which uses a mechanism that traps water within the Spar to control the *effective mass* of that body and effectively the natural frequency; they showed that this could expand the efficient operational range of incident wave frequencies for the device [33]. Orazov et al. admitted the numerical model was highly simplified and Diamond et al. expanded that model with the inclusion of a higher fidelity model of the momentum transfer associated with the mass flux of water into and out of the Spar. They concluded that the device power conversion efficiency could indeed be increased with the use of the mass-modulation scheme [35]. Diamond et al. more intimately explored the topic of mass-modulation schemes by comparing experimental results with numerical model results; discovering that a particular method of trapping water was needed in order to increase the harvesting potential of the WEC [34]. It is worthy to note that these models operated in a single degree of freedom (**DoF**), heave, the power producing degree of motion.

Variable Inertia System WEC (VISWEC)

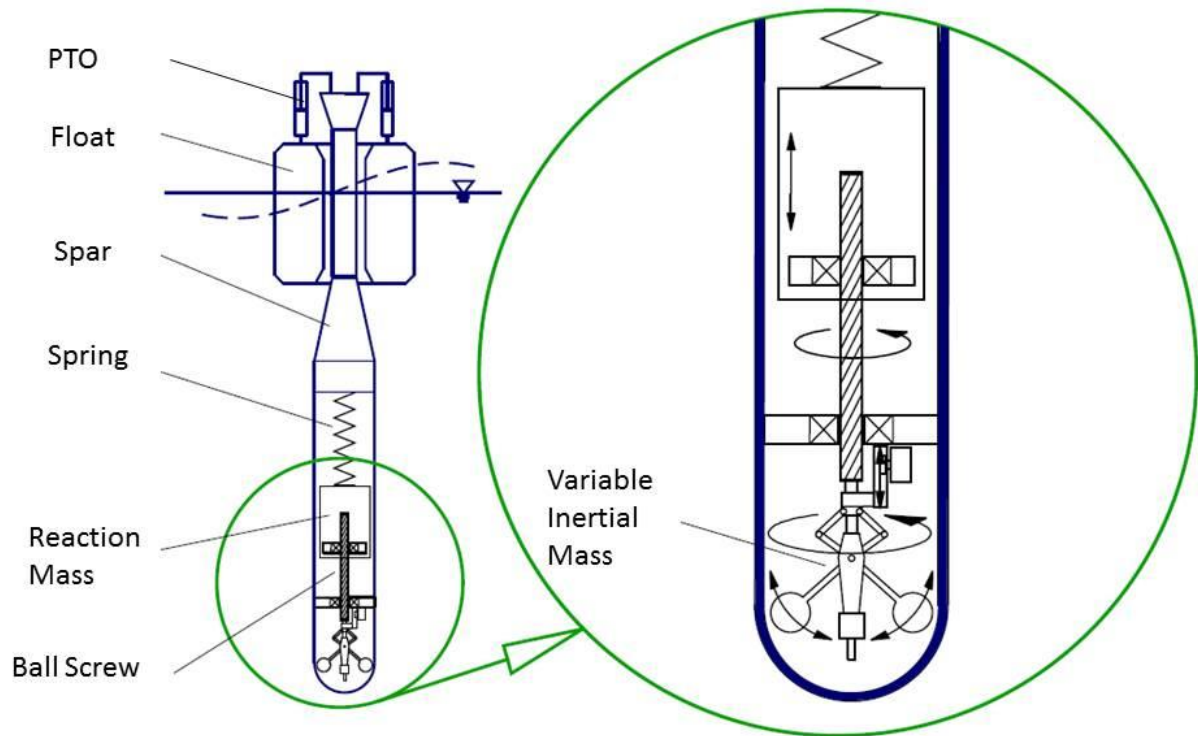


Figure 10: Internal Mass-Modulation Scheme as conceptualized within the University of Victoria [36]

In 2007, the University of Victoria (**UVic**) started research on a GC-SPRA WEC that used an inertially controlled Spar to vary the natural frequency of the system [37]. This WEC is an SRPA with an internal elastically supported Reaction Mass that allows the control of the natural frequency of the larger body, here on referred to as VISWEC. In Figure 10, the two main bodies can be identified, from here referred to as the Float and Spar, these are the only two bodies with a wetted hull. The Float is smaller and hydrodynamically stiff, designed to closely follow the water displacement while the Spar is larger and designed to respond out of phase with the waves as to invoke the greatest relative motion between the two bodies.

The topology of this WEC is similar to most SRPAs but the innovative part is the inertially controlled Spar where a large Reaction Mass is suspended by a spring allowing it to react separately from the rest of the Spar. The Reaction Mass is connected to a ball screw, converting relative linear motion of the Reaction Mass within the Spar to rotational motion in the ballscrew.

The variable inertia mass, which is mounted at the end of the ballscrew, controls the rotational inertia of the ballscrew and in turn the resistance of vertical motion of the Reaction Mass. In order for relative acceleration between the Reaction Mass and Spar to occur, the variable inertia system (**VIS**) must accelerate in rotation. As such, the VIS adds an additional (and variable) level of inertial resistance to the relative oscillations of the Reaction Mass.

In the equations of motion for the system, this additional rotational inertia appears as an additional mass that is added to the true magnitude of the Reaction Mass – it is often referred to as an *effective mass*. This coupling of the rotational and translational inertias allows the dynamic response of the system to be adjusted through direct adjustments to the rotational inertia and avoids the transfer of actual mass to/from the spar as is the case in the WaveBob SRPA *architecture*.

The internal coupling can be seen as a way to detach mass from the Spar allowing it to be more responsive at higher frequencies. That natural oscillation tendency combines with the hydrodynamic properties of the spar (e.g. damping) can create out of phase oscillations with the Float to improve power performance. At the theoretical extremes: if there was no rotational inertia the Spar and Reaction Mass would only be connected through the supporting springs and have a maximum natural frequency; as the rotational inertia grows the Reaction Mass would impose more mass on the Spar and eventually lock together, reacting as one body with the total mass of both giving a minimum natural frequency. In between these two extremes there is a continuum of settings, this allows for the control of the *effective mass* through the control of the VIS allowing the system to act in resonance through a larger bandwidth. A fundamental feature of this design is the ability to perform as a 2-body or a 3-body system. A 2-body system is a conventional SRPA where there is only a Float and Spar; the 3-body system is the system where the Spar is utilizing the VIS, when the Reaction Mass is fused with the spar it acts as a conventional 2-body system. When the VIS is fused, it is done so the center of gravity of the Spar is not altered, this is also where the Reaction Mass naturally hangs with the support of the springs.

Physical Model Basis for Numerical Model

The 1/25th scale physical model shown in Figure 11 was developed by Bubbar and the author for a physical modelling test program that is currently underway at the UVic. The scale was determined with a general full-scale size in mind but since there is no current full scale

device the scaling of the model is approximate. In addition to being the basis for the numerical model tested within this thesis, the physical model allows for future validation between this and experimental work.

No change in hull geometry between the 2-body and 3-body system allows for the identical exterior geometry to ensure there is no change in the hydrodynamics affecting power production. This is crucial so that the difficult to determine hydrodynamic coefficients are static through multiple configurations making the response more easily predictable. This design allowed for all physical parameters to stay constant while the *effective mass* was varied. To convert from a 3-body to a 2-body the Reaction Mass would be locked down, unable to move without the Spar. When designing this device, constraints in the testing facility size forced design changes such as the spring tubes extending into the upper spar accommodating the elastic supports. This is not the optimal design but as it is the only physical realization to date this work will follow this physical model.

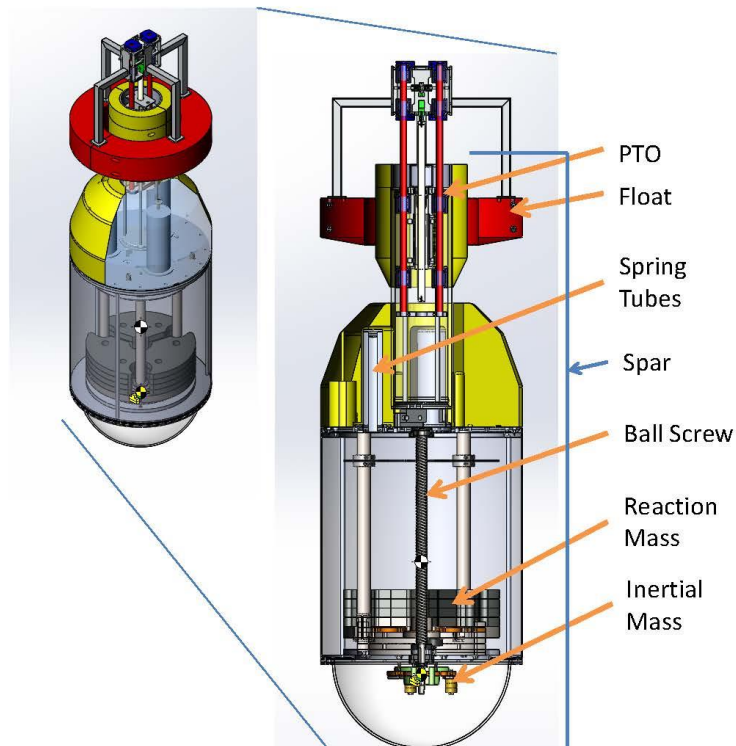


Figure 11: Working Physical Model

Previous Dynamic Research on VISWEC

The development of the VISWEC concept at the UVic was initiated by Beatty, who tested a two-body point absorber, an SRPA without the geometric control, in order to establish a baseline level of performance and allow improvements associated with the variable inertia system to be calculated. Experimental tank testing was performed on scale size SRPAs to determine hydrodynamic coefficients and characterize the reactions from a wave field. The results were compared with a frequency domain, linear, heave constrained dynamics model to validate the accuracy of the numerical model. Beatty's work went on to outline recommendations for design improvement upon the original patent design and specifications for a full-scale WEC to meet the requirements of a remote island community [38]. Mosher expanded on this research with frequency domain, heave constrained modelling to encompass time-variation parameter control. In Mosher's work, the design recommendations from Beatty's work were realized into Figure 10 [36]. Mosher analyzed the WEC's physical control parameter in the frequency domain allowing for design refinement at the conceptual level.

This idea of pre-design analysis was continued with Bubbar's work where an analytical solution for the optimal PTO and Geometric control is sought for a WEC with variable geometric parameters [31]. Bubbar extended the concept of applying electrical circuit theory to mechanical systems as Falnes did with the simplification of a two-bodied system to a single-body system [23], [25]. The mechanical circuit method of modelling mechanical systems operates on the principle of mechanical impedance, quantifying the response of a structure when subjected to a oscillating wave force; discussed in Chapter 4.

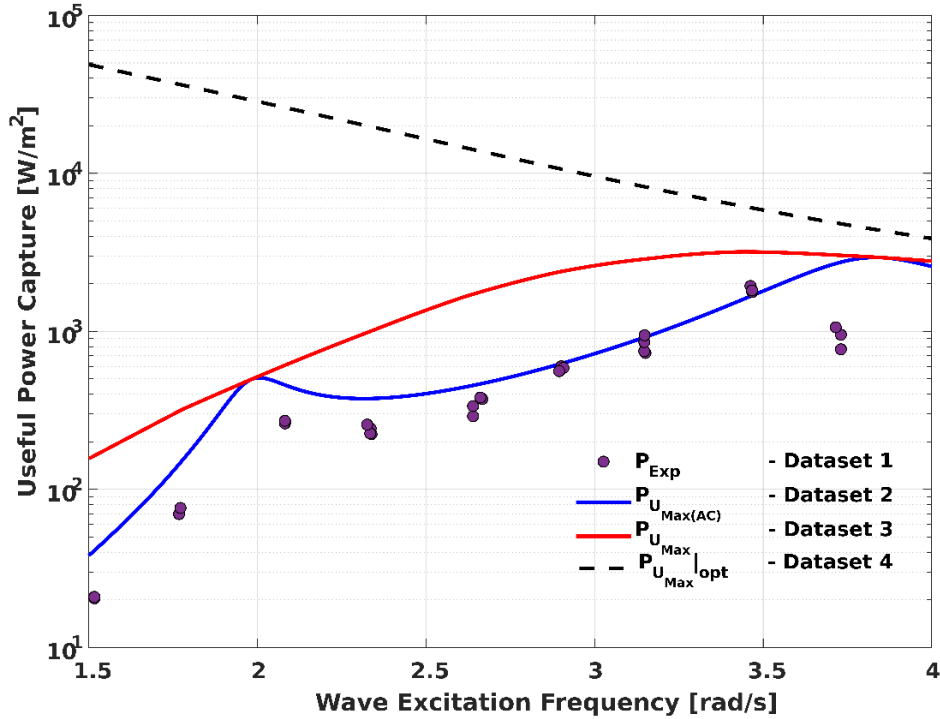


Figure 12: SRPA (datasets 1 and 2) and Geometrically Controlled SRPA (dataset 3) Power Capture Comparison with the Budal limit (dataset 4) [25]

Figure 12 shows the comparison between Beatty’s experimental work (dataset 1) and Bubbar’s theoretical work of: model of Beatty’s experimental design (dataset 2), the design Beatty used with reactive control (dataset 3) and a WEC with geometric and reactive PTO control (dataset 4). These are preliminary finding to the gains possible with geometric control. This work will provide numerical results for comparison to experimental data.

1.8 Gap in Knowledge

The majority of the research completed at UVic on SRPAs and the VISWEC system has been constrained to have only numerical models and experimental trials leaving questions as to the spatial motions of the VISWEC. The heave constraint is implied because the heaving mode of motion is the power producing mode of motion and ideally the system would only move in the one mode of motion to maximize power output. Although, as Beatty found on two geometrically different SRPAs when performing full 6-DoF (surge, sway, heave, roll, pitch, yaw) experimental tests and numerical models, SPRAs are susceptible to excitation in the rolling and pitching modes of motion especially at certain frequencies which the numerical results did not predict [39]. These types of motions pull energy from the system reducing the efficiency of power

conversion. Subtleties in the mechanical design of an SRPA have significant impact on the instability. Ortiz's attempt to optimize mooring structures for an SRPA showed that optimal moorings actually were mitigating roll instability during operation.[40]. If that was observed by Ortiz, then it is possible that the gyroscopic effects of the spinning/oscillating VIS and Reaction Mass could impact the roll instability as well. This is a complex multi-body 6-DoF system and there is a need to establish an expectation on whether the roll instability is going to be mitigated or exacerbated by the proposed VISWEC architecture. This work aims to provide data on the impact of adding the VIS system to an SRPA WEC.

1.9 Thesis Objective and Contribution

The objective of this thesis is to use a six degree of freedom (**6-DoF**) high fidelity numerical simulation to:

1. Evaluate both systems for power production
2. Evaluate both systems for parametric excitation
3. Determine if the implementation of the VIS promotes or mitigates parametric excitation and if it produces more power than the 2-body equivalent

This work will describe a method to calculate the theoretical optimal resistive PTO control of the PTO and determine the optimal geometric control for the VISWEC system shown in Figure 11. The numerical model will include representative drag forces both within the system and between the fluid and structure. Comparisons will be made with the metric of power production and this work will examine how the parametric excitation problem is promoted or mitigated by the implementation of the VIS and if this negatively or positively impacts power performance.

This work will help others to understand the phenomenon of parasitic parametric excitation that plagues SRPA WEC systems by identifying, isolating and analyzing all pertinent modes of motion for any potential parasitic motion through time domain numerical modelling. Both SRPA and VISWEC systems will be inspected to determine if the effect is enhanced or diminished with the presence of the VIS.

1.10 Thesis Outline

This thesis contains 6 chapters, the first outlining a brief history of energy production, the need for diversity and how wave energy can help fulfill that need. In addition, it covers the

general type of converter and well as the specific system studied in this work concluding with the contributions this work will bring to the field.

Chapter 2 contains information about the VISWEC dynamics, describes the phenomenon of parametric excitation and why it is a problem for the WEC studied in this work. Chapter 3 will state the static parameters of the system and how they were obtained while Chapter 4 will describe the dynamic parameters of the system and how they were obtained such as the method for obtaining the optimal *effective mass* and PTO damping value.

Chapter 5 will outline the testing conditions including the wave field and kinematic constraints, why they were chosen and the results that follow with discussion on what is displayed. Chapter 6 will present the conclusions and any recommended future work. Any additional information and references can be found after Chapter 6, at the end of this work.

Chapter 2 **VISWEC Dynamics**

This chapter will focus on a particular phenomenon within the complete interaction of a floating body and a propagating water wave, namely parametric excitation in the pitch and roll degrees of freedom. Examples showing how parametric excitation complicates system response in ocean waves, and why these complications are relevant to WEC dynamics analysis, will be given.

Parametric excitation is a phenomenon that can affect WECs and other floating structures. The fundamental definition of parametric excitation is the amplification of a response parameter (e.g. a degree-of-freedom or DoF) due to the time varying (i.e. harmonic oscillation) of an intrinsic physical parameter. This phenomenon can be seen in the simple case of a child on a swing, as they change the effective pendulum length by changing their center of mass, raising and lowering their legs, they increase their swinging motion. It is important to note that the child cannot randomly change their pendulum length to gain motion, they must do it at a specific frequency. This frequency is a harmonic, or a multiple of the natural frequency, more specifically the second harmonic or twice the natural frequency of the pendulum. In electrical engineering this phenomenon is taken advantage of to amplify harmonic electrical signals [41]. Rhoads et al. noticed that parametric excitation was often utilized within electrical and communication systems but was yet to be implemented usefully in larger mechanical systems, and sought to close any possible knowledge gaps by providing an example of a mechanical amplifier [42].

In naval architecture, parametric excitation is not intentionally exploited but it can be responsible for unstable and unwanted ship motions, as will be presented in this chapter. This chapter will first present the basics of linear wave theory and how the buoyant force is

calculated. Then a section of an overview of parametric excitation with similar bodies to that of the system under investigation and showing how the phenomenon of parametric excitation is being handled in floating spar platforms where motion is undesirable and then WECs where motion in power producing modes are desirable but not in others directions. The following section will outline the difference of the derived stability between buoyancy stabilized, such as vessels, and ballast stabilized such as point absorber type WECs. Once the difference is established, a section on how ballast stabilized bodies are of the Mathieu type equation and validated by the section following presenting a test case. The final section will make closing remarks on parametric excitation and the dynamics of the system to be investigated.

2.1 Linear Wave Theory and Buoyancy

Here a short summary of linear wave theory is presented as it is the foundation of existing studies on parametric excitation of floating structures. As wind hits the ocean surface, deforming it from its steady state, surface tension and gravity work to restore it resulting in wind generated waves. Waves in the ocean can be generated by other forces such as gravity from the sun or moon and objects breaching the surface, like ripples from a stone dropped into a pond, but gravitational waves have a wavelength much too large for WECs to exploit and objects falling into the ocean are not consistent enough of a generator to focus on. Wind generated waves are the most pertinent to consider when working with WECs because wind generated waves are common, can persist over a long predictable time period and have a wavelength exploitable by WECs.

Naturally occurring wind wave sea states can be linearly represented as a combination of cosine functions. Linear wave theory, also referred to as Airy wave theory or small wave theory, is based upon a number of assumptions: the fluid is homogenous, incompressible, inviscid, and irrotational, the pressure at the surface is uniform and constant, the bottom is smooth and impermeable, the waves are two dimensional and the wave height is much smaller than both the wavelength and water depth. This theory also neglects surface tension and Coriolis effects as the former is applicable to very small scale forcing and the latter to very large scale forcing. The fluid particles within the wave are understood to move in orbitals, or circular motions. The surface displacement (η) in linear wave theory is calculated using eq. (2.1), where h is wave height, ω is the wave angular frequency, λ is the wavelength, θ_h is the wave heading and ϕ_0 is

the constant wave offset which randomizes the starting phase of each superimposed wave [43]. Since this work will only use single frequency regular waves from a single heading, the equation can be simplified to eq. (2.2), where θ_w is the phase of the wave. The phase can be calculated by eq. (2.3) where k is the wave number ($1/\lambda$). The theory and terms used are visualized in Figure 13 where the waveform is accompanied by the orbital motion of the water particles. These orbital motions cause pressure differences within the wave column and these pressures exert forces on any structures present within.

$$\eta = \frac{h}{2} \cos(\omega_e t - \frac{2\pi}{\lambda} (\cos(\theta_w) x + \sin(\theta_w) y) + \phi_0) \quad (2.1)$$

$$\eta = \frac{h}{2} \cos(\theta) \quad (2.2)$$

$$\theta_w = kx - \omega_e t \quad (2.3)$$

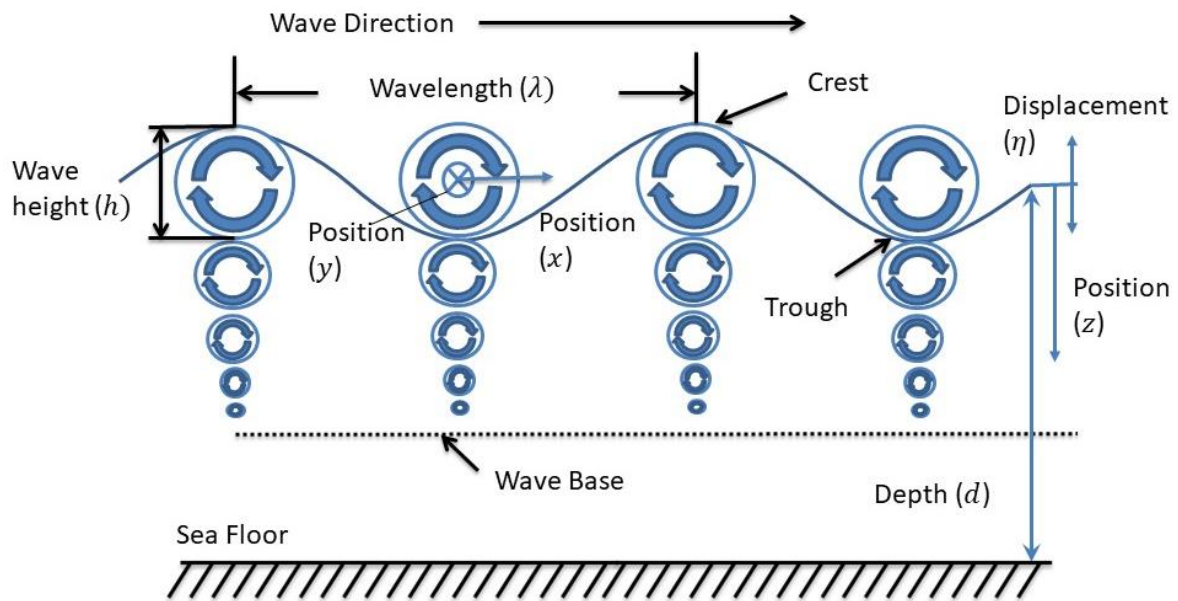


Figure 13: Wave Terms: wavelength is from crest to crest or trough to trough, wave height is the vertical distance from crest to trough, and positions x (with the wave propagation) and y (across the wave front) for waves are referenced from the center of orbital rotation while z is taken from the free surface is $z = 0$ as a wave passes. The displacement η is assumed to be nominal.

According to linear wave theory the undisturbed pressure (N/m^2) can be calculated at any depth as:

$$p = \rho g d + \frac{1}{2} \rho g h \frac{\cosh \left[\frac{2\pi}{\lambda} (z - d) \right]}{\cosh \left(\frac{2\pi}{\lambda} d \right)} \cos(\theta_w) \quad (2.4)$$

Equation (2.4) has two components: the hydrostatic pressure or the pressure due to depth ($\rho g d$), viscosity gravity and depth multiplied and the second part is the pressure variance due to the wave which is dependent on the position in depth z , wave height h and the wavelength λ . As the submerged depth increases, the first term dominates the equation and at shallow depths the pressure fluctuation is greater from the waves. These pressures can be multiplied by the surface area of a submerged body to calculate the force acting on that area. The sum of the hydrostatic pressure around a submerged object results in the buoyancy force which is equivalent to the weight of the fluid displaced by the body and acts through the centroid. This force can be idealized as a linear elastic response if the volume changes linearly with a change in draft, i.e. the water plane area does not change with heaving motion as shown in Figure 14.

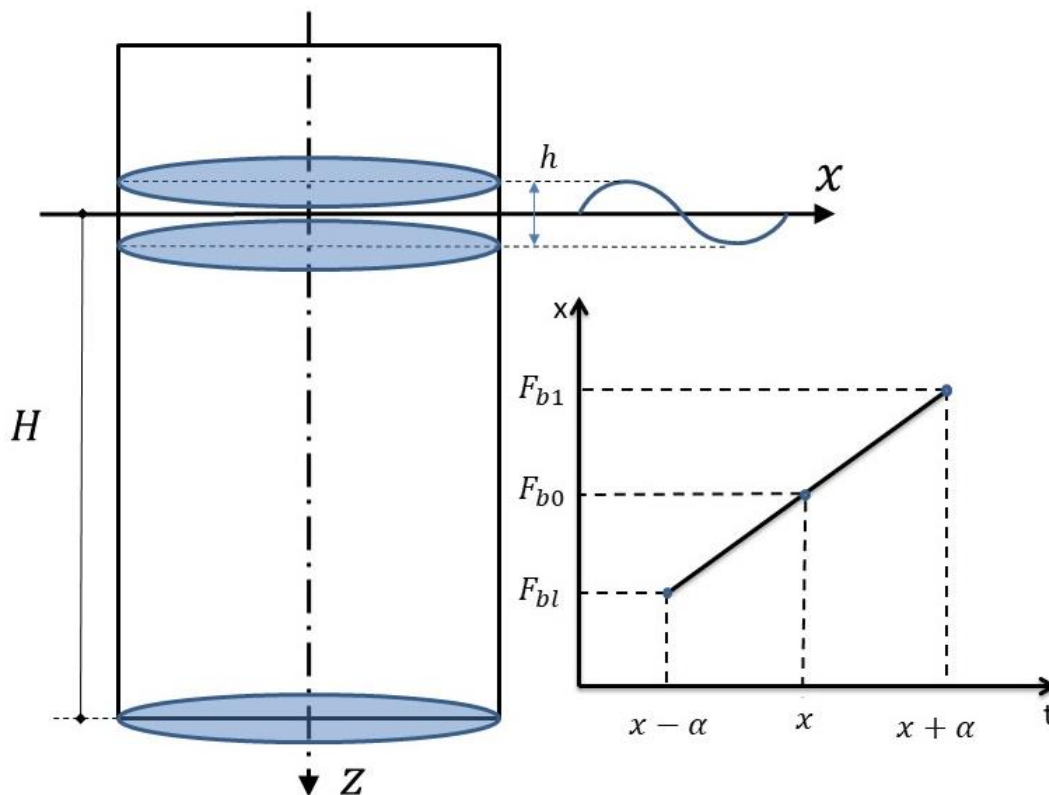


Figure 14: Linear Buoyancy Force

Considering only the heave of a body, the changes in submerged water volume are trivial as long as the waterplane area is constant with draft. If this holds true, then eq. (2.5) is sufficient to calculate the linear hydrostatic buoyancy force, F_b . This buoyancy force is only in the heave direction. If the body tilts then there will be a moment created by the buoyant force, as discussed later. A body that has a large value for C_k , is considered to be hydrostatically stiff. Though it is possible to calculate the buoyancy force by calculating the displaced volume of water multiplied by the density of water, if work is to be done in 6-DoF then it is necessary to calculate the submerged volume and locate the new centroid of that volume.

$$F_b = C_k z \quad (2.5)$$

$$C_k = \rho g A_0 \quad (2.6)$$

2.2 Parametric Excitation Literature Review

Stabilizing a floating body is accomplished in two ways:

- 1) Buoyancy
- 2) Ballast

Buoyancy stabilized bodies such as vessels depend on the geometry to move the buoyancy force to create a moment to right the vessel. The center of gravity is located above the center of buoyancy as mentioned in Section 2.3.1 and shown in Figure 16. Ballast stabilized bodies, on the contrary, rely on gravity to keep the body upright. The center of gravity is below the center of buoyancy as mentioned in Section 2.3.2 and shown in Figure 18. The following subsections review previous work on parametric excitation on ballast stabilized bodies

2.2.1 Spar Platforms

The work on parametric excitation, which originated in naval architecture for floating vessels, was applied to the analysis of stability on spar platforms. A spar platform is a large submerged cylinder with a platform atop, typically an oil rig, which is subject to heaving, rolling and pitching motions. Work has been done to study the relation between heaving and pitching/rolling motions associated with parametric excitation. Haslum and Faltinsen, studied the instability of a spar platform with large heaving amplitudes in resonance using a simplified numerical model that used a time varying pitch restoring moment along with a physical model [44]. They proposed a geometric change of the spar to alter the natural frequency of the heaving motion to help reduce the resonant response which mitigated the motions in roll and pitch by

reducing the variation in the restoring moment by reducing the variation in the buoyant force. Similarly, Rho et al., used helical strakes, damping plates, and moon-pools to change the natural frequency of the spar platform which reduced the heaving motion as well as the pitching motions confirming heave and roll/pitch are coupled [45]. Although Rho et al., did not consider the pitch damping, Zhang et al., extended this research to include it. They found that the addition of pitch damping changed the natural frequency but parametric excitation was still present [46]. Further extension of this work by Koo et al., considered the time varying displacement of the structure and continued to observe parametric excitation [47]. All of these works concur that the coupling between heave and pitch/roll can be modeled as a Mathieu type equation and show that parametric excitation exists in both experimental and numerical results. No matter which modelling techniques were used to vary the righting moment, parametric excitation was present.

It is worth noting that Neves et al., have published both on unstable ship motion and vertical cylinders, agreeing that ship motions are characteristic of parametric roll and a Mathieu type equation but contradicted that vertical cylinders did not experience the same type of phenomenon because the origin of the roll excitation was from the forcing of the wave field not in the GM variation [48], [49]. However, while the source of the variation of the righting moment is different or dominated more by the change in buoyancy rather than buoyancy stiffness the phenomenon is still caused by the change in the righting moment. The work of Neves et al., on vertical cylinders included both experimental model testing and numerical simulation of a vertical cylinder with a large diameter, small draft and a variety of mooring configurations [49], contrasting previous work [44]–[47] that had a smaller diameter than draft and no moorings. Neves' model would tend to be more stable and less susceptible to parametric excitation due to a larger GM, as shown in the small percentage ΔGM change in the test case. The work still showed results of pitching and rolling excitation at frequencies that were claimed to not be characteristic of the Mathieu type equation and no amplification at the characteristic frequencies but it is noted that further investigation should be conducted into the effects of moorings on a system which could affect the resonant frequency of the system. Ortiz's work mentioned in the following section, showed moorings have a large impact on the motions of a vertical cylinder and can change the natural frequency of the system [40].

2.2.2 WECs

Within ocean energy conversion, parametric excitation was seen both as an opportunity and a predicament. Rhodes et al., published on the utilization of parametric excitation in electrical engineering and implored other facets of engineering, such as mechanical engineering, to take advantage of parameter pumping for increased output. Parameter pumping is a term for the active variation of a parameter to incite parametric excitation [42]. Positive effects of parametric excitation have been implemented within the wave energy field. The technique of parameter pumping was implemented by Olvera et al., by varying the volume of the air chamber within an OWC in order to achieve resonance within the chamber and achieve a lower power loss [50]. They were successful in their numerical modelling of the system but only commented on a physical solution for future work and did not test one. More recently, Hals et al., proved a design with a bottom-referenced SBPA where the natural frequency of the system could be varied through a mechanism that can push or pull, effectively changing the mass of the system to alter its response; they found the device to increase power absorption by three times [51].

Parametric excitation has also caused power loss in wave energy converters. Both experimental and numerical results of an SRPA WEC showed that at particular frequencies, rolling and/or pitching motions that were parametrically amplified and were linked to decreased relative heave motions resulting in lower power production than expected at those frequencies [39], [40], [52], [53]. This parametric excitation is considered to be a parasitic type of excitation as the excited motion requires energy and results in a lower power production. This parasitic type of parametric excitation has been noted and observed but scarcely published. Wavebob, one of the first large companies investigating a SPRA WEC, encountered the issue of pitch and roll amplification associated with parametric excitation and used a PTO control strategy to mitigate the pitch/roll motions and increase power production [52], [53]. Using similar WEC geometry and numerical modelling techniques used for this work, Tarrant and Maskell, show excitations in both pitch and roll of an SRPA WEC in both numerical and experimental testing at characteristic frequencies. They also showed the occurrence of parametric excitation and the amplification of the rolling angle with higher PTO damping coefficients [52]. More numerical and physical model testing was conducted by Beatty et al., who provides results of a geometrical mitigation technique; adding strakes to added resistance in the pitch and roll DoFs while minimally affecting the heaving motions [39]. In conjunction with these results is Ortiz's work on full scale

numerical modelling of an SRPA WEC with focus on the effects of moorings, finding that mooring system configurations could both induce and mitigate parametric excitation depending on the design. This excitation had a large effect on power output, the higher power production occurred when there was little to no roll or pitching motions [40].

2.3 Righting Moment

Naval Architects were some of the first to investigate parametric excitation on floating structures dating back to the 1950's where a nonlinear coupling between roll stability and rolling motions was noticed [54]–[56]. Roll stability pertains to the righting moment caused by the buoyant force when the body is tilted, the stronger the moment the more stable the body. The term nonlinear coupling refers to the system's rolling response not being proportional to the change in inputs of the wave loading and that the response is coupled with the change of the righting moment. The instability can be caused by any term in the rolling moment oscillating to cause an oscillation in the stability in rolling moment. The variation of the stability of roll could cause rolling motion in ships, the variation in rolling moment is first considered without the heaving motion of the ship. Without a change in heave, the change in stability originates from the change in buoyancy stiffness since the density of water and the gravitational constant are not changing, a change in waterplane area will drive the change in buoyancy stiffness.

Typically, one of the following scenarios dominates any resulting change in righting moment and can be used exclusively.

- 1) The body is stationary while a wave passes
- 2) The body changes its draft while the water is stationary

Most ships have a long profile, sometimes longer than the wavelength, as well as non-uniform geometry. This can cause the water plane area to change drastically depending on the wave state, as presented in Figure 15. The volume of the ship below the water plane determines the location and magnitude of the buoyancy force. Changes in the water plane cause changes to the buoyancy force affecting the righting moment (the moment that restores the ship to its steady state position) [54], [57]. Spars and WECs have a large mass and moment of inertia and tend not to significantly move as a wave passes. Therefore, the change in buoyancy force for ships and similar floating bodies is best represented by scenario 1, and there is limited influence from scenario 2 as pitching and rolling are minimal and mitigated where possible.

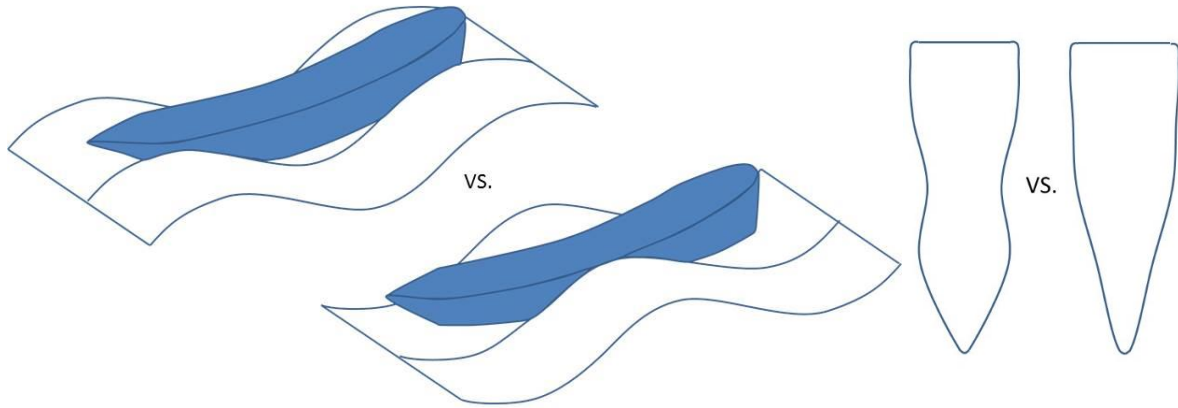


Figure 15: Two points in time as a wave propagates past a long vessel and changes the waterplane area

Floating bodies that are small compared to the wavelength tend to have a relatively level displaced water elevation across their bodies as the wave passes, therefore the waves can be most closely represented by a still, oscillating, level waterline. The diameter of a point absorber, more closely examined in Chapter 3, is small in comparison to the wavelength, it has a typical diameter of approximately 0.30 m compared to typical wavelengths, more closely examined in Chapter 5, of 2.85 – 20.26 m (both given at 1:25 tank scale), and therefore the work pertaining to WECs in Section 2.3.2 will also consider the second scenario.

2.3.1 Buoyant Righting Moment

When pertaining to vessels, the waterplane area and buoyant force is considered to oscillate with the passage of a wave. The scenario is explained by Allivevi and Soundack [58] when considering a cross-sectional view of center of the vessel, where the side walls are vertical, visualized in Figure 16. A ship in its stable position has a center of gravity (G) vertically above the center of buoyancy, Z_B , and a vertical line can be drawn through both of these points. This configuration of buoyancy and gravity means that the body is buoyancy stabilized. When this ship tips at an angle θ_x from its stable position the center of buoyancy moves laterally as demonstrated in Figure 16, while the center of gravity, the reference point, remains in the same relative position on the ship. A new vertical line can be drawn through the center of buoyancy which will intersect with the original central longitudinal plane of vessel; the point at which they intersect is the metacenter (M), as seen in Figure 16. Point Z is defined as the position along the new vertical line which is level to the center of gravity. The horizontal distance between G and Z

is \overline{GZ} . This distance is the moment arm of the buoyant force. The righting moment M_θ is calculated from eq. (2.7) where the buoyancy force is multiplied by GZ .

$$M_\theta = F_b \overline{GZ} \quad (2.7)$$

The distance from the center of gravity, G , to the metacenter, M , is the transverse metacentric height (\overline{GM}) which quantifies the rolling stability of a ship; the larger the metacentric height is, the larger the righting moment will be for any set roll angle and the more stable a ship will be in the roll DoF.

As the wave passes and the local water level changes it varies the buoyancy force, F_b , both in location and magnitude as shown in Figure 17. The change in location of the center of buoyancy and its magnitude varies the righting moment, M_θ . Parametric excitation comes from the variation of the righting moment which originates from the variation of the magnitude of the buoyancy force, F_b , the moment arm \overline{GZ} or both.

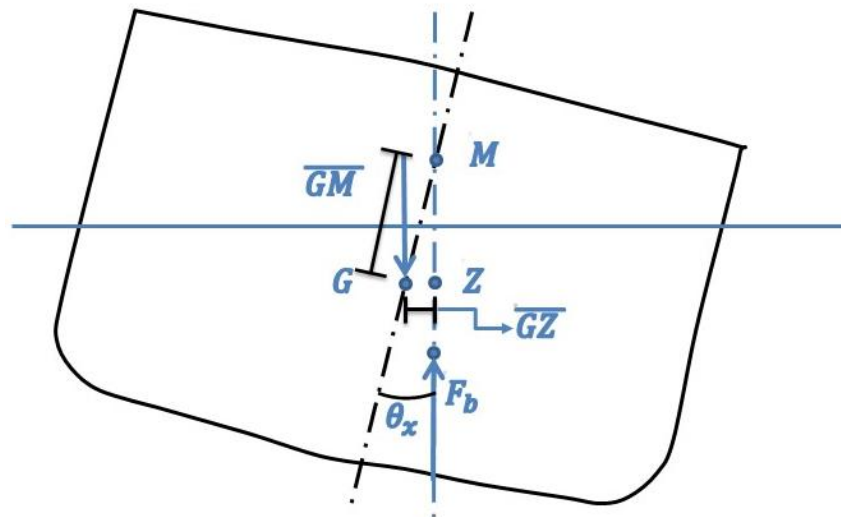


Figure 16: Righting Moment with center of gravity, metacenter buoyancy and roll angle for a buoyancy stabilized body

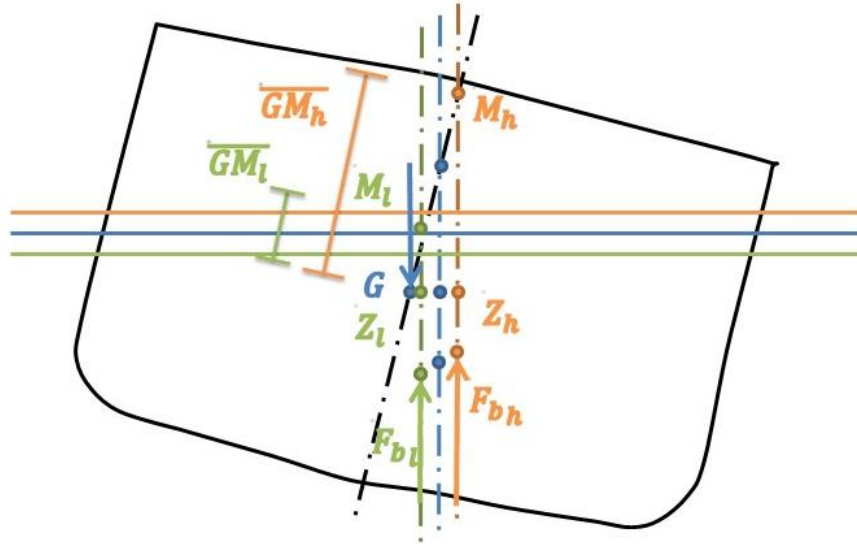


Figure 17: Variation of the righting moment through the movement of the waterline causing both a change in buoyancy force and moment arm, subscript indicates the higher waterline, h , and the lower waterline, l .

There is a time modulation of the metacentric height as the wave pass the ship. For ships, the roll dependence of the F_b and \overline{GZ} terms adds significant complexity. In the next section ballast stabilized vertical cylinders, the typical geometry of point absorbers type WECs, are considered

2.3.2 Ballasted Righting Moment

To discern how the righting moment variation can incite internal parameter response growth we examine a case of an arbitrary submerged cylinder as shown in Figure 18 with a draft H , center of buoyancy, B , cross-sectional area, A_0 , and the reference point, center of gravity, G . The case of a submerged cylinder differs from the case of a vessel in the fact that the gravity is lower than the buoyancy making it a ballast stabilized body; this is the same case with a point SRPA system. The cylinder will rotate about the reference point center of gravity, G , and the distance between B and G is the metacentric height \overline{GM} for buoyancy stabilized bodies. As a wave, with the free surface elevation, η , and height, h , passes the cylinder it creates an additional submerged area with height $\alpha = \frac{h}{2}$. This change in submerged area causes a change in the center of buoyancy, B' , and a change in metacentric height $\Delta\overline{GM}$.

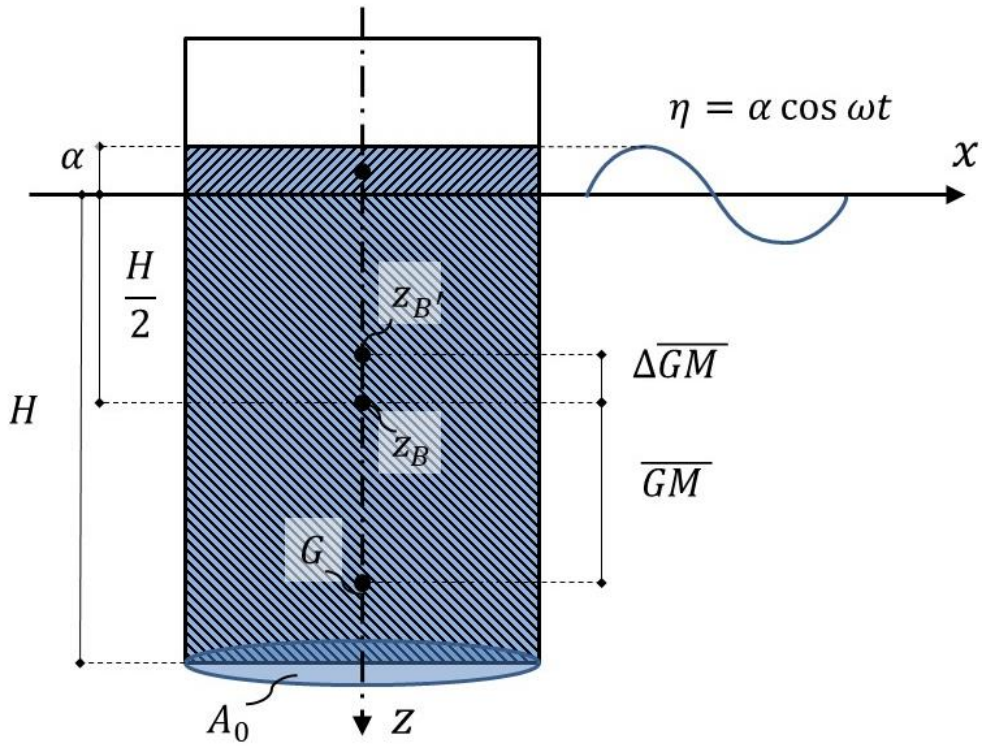


Figure 18: A submerged cylinder exposed to an incoming wave.

The location of the altered buoyancy by the wave on the z axis can be expressed as the center of each volume divided by the whole:

$$z_{B'} = \frac{\frac{H}{2}(HA_0) + \left(-\frac{\alpha}{2}\right)\alpha A_0}{(H + \alpha)A_0} \quad (2.8)$$

Cancelling out A_0 and bringing the equation to two dimensions:

$$z_{B'} = \frac{\frac{1}{2}(H^2 + \alpha^2)}{H + \alpha} = \frac{\frac{1}{2}(H + \alpha)(H - \alpha)}{H + \alpha} \quad (2.9)$$

$(H + \alpha)$ in the numerator and denominator cancel for the new location of buoyancy:

$$z_{B'} = \frac{1}{2}(H - \alpha) \quad (2.10)$$

Therefore the change in metacentric height for one half of the wave is:

$$\Delta \overline{GM} = \frac{H}{2} - \frac{1}{2}(H - \alpha) = \frac{1}{2}\alpha \quad (2.11)$$

The righting moment as shown in eq. (2.4) can be rewritten in terms of volume and distance \overline{GM} . With the assumption the roll angle is small the equation can be simplified with the small sine angle approximation $\sin\theta_x \approx \theta_x$:

$$M_\theta = F_b \overline{GZ} = -\rho g \nabla \overline{GM} \sin\theta_x \approx -\rho g \nabla \overline{GM} \theta_x \quad (2.12)$$

Adding in the change in volume and righting arm:

$$M_\theta = -\rho g [\nabla_0 + A_0 \alpha \cos(\omega_e t)] [\overline{GM}_0 + \Delta \overline{GM} \cos(\omega_e t)] \theta_x \quad (2.13)$$

Pulling the original volume, ∇_0 , out from the first set of brackets and simplifying the cross-sectional area divided by the volume with the knowledge that $\frac{A_0}{\nabla_0} = \frac{A_0}{A_0 H} = \frac{1}{H}$; additionally substituting $\Delta \overline{GM}$ from eq. (2.11)

$$M_\theta = -\rho g \nabla_0 \left[1 + \frac{\alpha}{H} \cos(\omega_e t) \right] \left[\overline{GM}_0 + \frac{\alpha}{2} \cos(\omega_e t) \right] \theta_x \quad (2.14)$$

Multiplying through the two sets of brackets reveals the \overline{GM}_0 in two of the terms which is then pulled out:

$$M_\theta = -\rho g \nabla_0 \left[\overline{GM}_0 \left(1 + \left(\frac{\alpha}{2\overline{GM}_0} + \frac{\alpha}{H} \right) \cos(\omega_e t) \right) + \frac{\alpha^2}{2H} \cos^2(\omega_e t) \right] \theta_x \quad (2.15)$$

Equation (2.15) shows how the variation in the righting moment is subjected to a cosine and cosine squared term, varying the term at the frequency of the oncoming wave. Additionally the variation of α can be seen in the constant term varied by the cosine and cosine squared, as well as the constant term not varied by the cosine. This will have an effect on the frequencies at which parametric excitation is experienced as shown in Section 2.5.

2.4 Rolling Dynamics and the Mathieu Equation

When the righting moment oscillates at the correct ratio (determined by the variables in the Mathieu Equation) to the rolling natural frequency, it can excite rolling motions [57]. A linear mathematical model can be used to describe this coupling that causes roll excitation [54], this linear mathematical model has been shown to fall under the classification of a Mathieu equation, outlined in [58] and in the following section. It is assumed that the oncoming wave does not have any forcing in the roll DoF, that the height of the wave is small in comparison to the draft of the body and that the body is not moving as wave passes. This section will outline what reductions are necessary to show that the equation of motion in the roll DoF is a Mathieu type equation as the term is often referenced in literature as shown in Sections 2.2 and 2.3.

Assessing eq. (2.15), the coefficient of the $\cos(\omega t)$, the perturbation caused by the wave, α , would be significantly smaller than the draft, H , and twice the original metacentric height, \overline{GM}_0 , so it can be stated that the coefficient is approximately zero leading to the removal of the $\cos(\omega_e t)$ term

$$M_\theta = -\rho g \nabla_0 \left[\overline{GM}_0 + \frac{\alpha^2}{2H} \cos^2(\omega_e t) \right] \theta_x \quad (2.16)$$

The double angle identity for $\cos \varphi$ is $\cos(2\varphi) = 2 \cos^2 \varphi - 1$, solving for the squared term results in $\cos^2 \varphi = \frac{1}{2}(\cos 2\varphi + 1)$

$$M_\theta = -\rho g \nabla_0 \left[\overline{GM}_0 + \frac{\alpha^2}{4H} (\cos 2\omega_e t + 1) \right] \theta_x \quad (2.17)$$

$$M_\theta = -\rho g \nabla_0 \left[\left(\overline{GM}_0 + \frac{\alpha^2}{4H} \right) + \frac{\alpha^2}{4H} \cos 2\omega_e t \right] \theta_x \quad (2.18)$$

The equation of motion for a floating body in the roll DoF can be expressed as eq (2.19) which is comprised of an inertial and gravitational term, respectively. The inertial term has the moment of inertia in the roll DoF, I_{xx} , multiplied by the acceleration of the rolling motion while the gravitational term is a righting moment (M_θ) that is dependent on the roll or pitch angle (θ_x) and time (t).

$$I_{xx} \frac{d^2 \theta_x}{dt^2} + M_\theta(\theta_x, t) = 0 \quad (2.19)$$

With buoyancy being the leading term in eq. (2.18) which can be substituted for the moment component of the equation of motion eq. (2.19)

$$I_{xx} \frac{d^2 \theta_x}{dt^2} + F_b \left[\left(\overline{GM}_0 + \frac{\alpha^2}{4H} \right) + \frac{\alpha^2}{4H} \cos 2\omega_e t \right] \theta_x = 0 \quad (2.20)$$

The roll natural frequency ω_x , is a function of buoyancy force and metacentric height which equal the rotational buoyancy stiffness and the moment of inertia in eq. (2.21). The roll inertia, I_{xx} is removed by dividing both terms in eq. (2.20) and substituting in eq. (2.21) and eq. (2.11) as represented in eq. (2.22).

$$\omega_x^2 = \frac{F_b \overline{GM}_0}{I_{xx}} \quad (2.21)$$

$$\frac{d^2\theta_x}{dt^2} + \omega_x^2 \left(1 + \frac{\alpha^2}{4HGM_0} - \left(\frac{\Delta GM\alpha}{2HGM_0} \right) \cos 2\omega_e t \right) \theta_x = 0 \quad (2.22)$$

The Mathieu equation is now introduced. It is a linear second order, homogeneous, differential equation with the general form of eq. (2.23) which solves for a transient response where β and γ are the independent varied and dependent response parameters respectively and a and q are real constants. This equation can be used to help describe the periodic motions of matter such as electrons, quantum pendulums and for this case floating bodies [59], [60].

$$\frac{d^2\beta}{d\gamma^2} + (a - 2q \cos 2\gamma)\beta = 0 \quad (2.23)$$

This equation characterizes two parameters and how an oscillating internal parameter can induce an increase in amplitude of the β parameter. If one interprets the generic parameters a and q of the Mathieu equation as eq. (2.24) and eq. (2.25) then it is apparent that eq. (2.22) is an instance of the Mathieu equation.

$$a \equiv \omega_x^2 + \frac{\omega_x^2 \alpha^2}{4HGM_0} \quad (2.24)$$

$$2q \equiv \omega_x^2 \frac{\Delta GM\alpha}{2HGM_0} \quad (2.25)$$

$$\frac{d^2\theta_x}{dt^2} + (a - 2q \cos 2\omega_e t)\theta_x = 0 \quad (2.26)$$

This derivation is confirmed in [58], [60] and the derivation shows how the rolling moment equation is a Mathieu type equation. This equation is known to experience instabilities in the response parameter when excited at the correct ratio to the natural frequency.

2.5 Test Case

To visualize and verify that rolling motion can be parametrically excited through the variation of the righting moment described previously, it was decided to demonstrate the roll response by numerically integrating different cases of the governing equation, eq. (2.27). The ODE was executed using an ODE function (ode45) within MATLAB, a numerical computing environment and proprietary programming language developed by MathWorks Inc. [61]. The ODE function, the same to be utilized within the simulation software, was used on the ODE to establish a data set of outputs for known inputs as shown in Table 1.

Table 1: Parameters for use in ODE

Parameter	Symbol	Value	Unit
Time	t	5400	seconds
Metacentric Height	GM	0.3	meters
Variation of GM	GM _{var}	0.83 – 33.3	%
Draft	H	1.65	meters
Displacement	α	0.005 - 0.2	meters
Excitation Frequency	ω _e	0.35 - 5.95	rad/s
Roll Frequency	ω _x	1.4	rad/s
Frequency Ratio	ω _{rat}	0.25 - 4.25	unitless

Equation (2.15) is used as the rolling moment for insertion into eq. (2.19), this rolling moment is before any assumptions are made and before any values are removed. The rolling moment of inertia is divided though and roll natural frequency from eq. (2.21) to produce the ODE shown in eq. (2.27). The ODE shown in eq. (2.27) is similar to the ODE shown in eq. (2.22) but contains no assumptions or identities.

$$\frac{d^2\theta_x}{dt^2} + \omega_x^2 \left[\left(1 + \left(\frac{\alpha}{2GM_0} + \frac{\alpha}{H} \right) \cos(\omega_e t) \right) + \frac{\alpha^2}{2HGM_0} \cos^2(\omega_e t) \right] \theta_x = 0 \quad (2.27)$$

The key ratios of frequency and variation of GM as presented in Table 1 resemble that of the system to be investigated in the work presented in Chapter 5 but are realized an approximations; the actual values need only to reflect the ratios of the test case. For this test case, a range of excitation frequencies (ω_e) were input from ¼x of the natural frequency (ω_x) to 4.25x the natural frequency (ω_x) and expressed as ω_{rat} as shown in eq. (2.28). The change in the metacentric height was varied as a proportion of the mean metacentric height and the variation of GM is shown in eq. (2.29).

$$\omega_{rat} = \omega_e / \omega_x \quad (2.28)$$

$$GM \text{ Variation} = \frac{\alpha}{2GM} 100\% \quad (2.29)$$

The resulting rotational displacement of the system (θ_x) is presented in Figure 19, where each plot shows the different excitation frequency, with all other inputs remaining constant in each sub-figure. It is worth noting that there is no damping in the test case simulation and the decrease in amplitude at particular frequencies is due solely to the excitation frequency not

internal dampening. The level of the response was correlated to the amplitude of deviation, α . Parametric excitation is demonstrated when the final oscillating displacement is much larger than the initial displacement meaning energy was added to excite the system. Values of displacement are calculated as the magnitude of the final oscillation and will often extend above the upper y-axis limit as the system has become unstable but this domain was kept in order to observe the responses of other frequencies; the information of concern is whether or not the system has increased or decreased away from the initial value.

As the variation of GM increases so does the amplitude of the response shown in Figure 19. Figure 19 only presents the response up to 5 times the initial condition but this is sufficient to demonstrate parametric excitation. When the GM variation is less than 0.83%, no parametric excitation was observed after 90 minutes of simulated time. Additionally, when the variation of GM was over 7% there was a single response at $\omega_{rad} = 2.0625$ as well as a small dip in magnitude following towards $\omega_{rad} = 2.25$. As the variation of GM grows the response migrates to the right to higher values of ω_{rad} and grows in both magnitude and bandwidth. This growth, both magnitude and bandwidth is similarly accompanied by a dip in magnitude immediately following although the magnitude is smaller and the growth in bandwidth is not as apparent. As the variation of GM climbs over 20% a second response, wider in bandwidth but smaller in magnitude, appears around $\omega_{rad} = 4$, more specifically from $\omega_{rad} = 3.5 - 4.25$. This growth is also accompanied by a dip in magnitude although counter to the previous response, this dip occurs prior to the response at frequencies around $\omega_{rad} = 3.0 - 3.5$.

The data shown in Figure 19 shows that the response generally occurs around a certain frequency but doesn't solely occur a specific frequency multiple and that the magnitude and bandwidth of response is correlated with GM variation. By analyzing the ODE equation it can also be said that the larger the draft (H) the less the response acting similarly as increasing the \overline{GM} Value and thus decreasing the effect of the $\Delta\overline{GM}$.

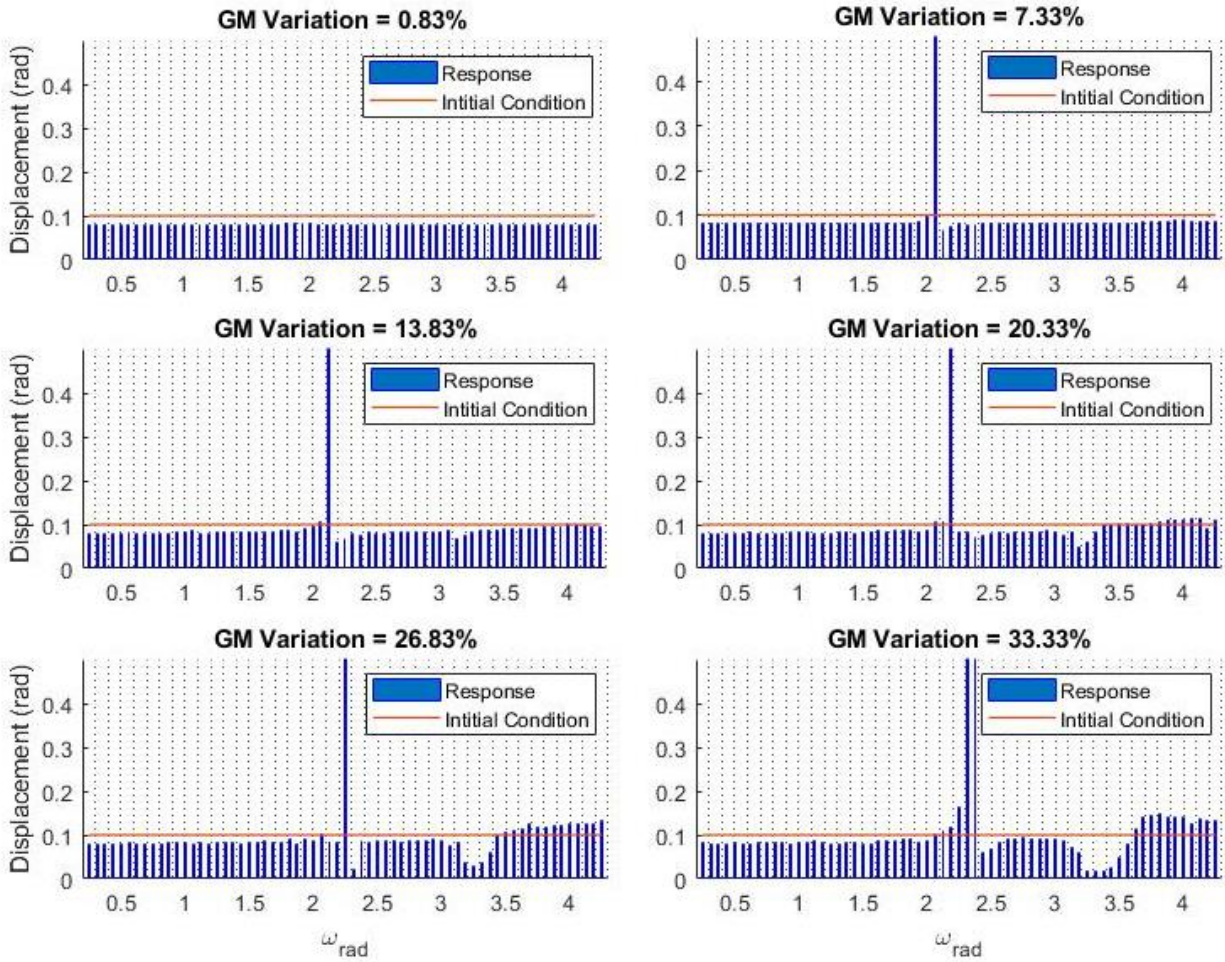


Figure 19: Mathieu Equation Test Case

Figure 20 displays the displacement of the system with a variation of GM of 20% for the first 60 seconds of $\omega_{rad} = 1.5 - 2.6$. The initial condition is also shown as 0.1 meters, both positively and negatively to show the bounds of the system, as the displacement grows outside these bounds the system is effected by parametric excitation. A multi-frequency response is also observed in all subplots, though not consistent across all subplots, the frequency of oscillation remains the same but the magnitude also oscillates at a second frequency. This second oscillation is apparent more so in subplots of $\omega_{rad} = 1.8 - 2.1 rad$ and $2.4 - 2.6 rad$, caused by the additional cosine term within the righting moment. After 60 seconds the system continues the trends seen in the first 60 seconds.

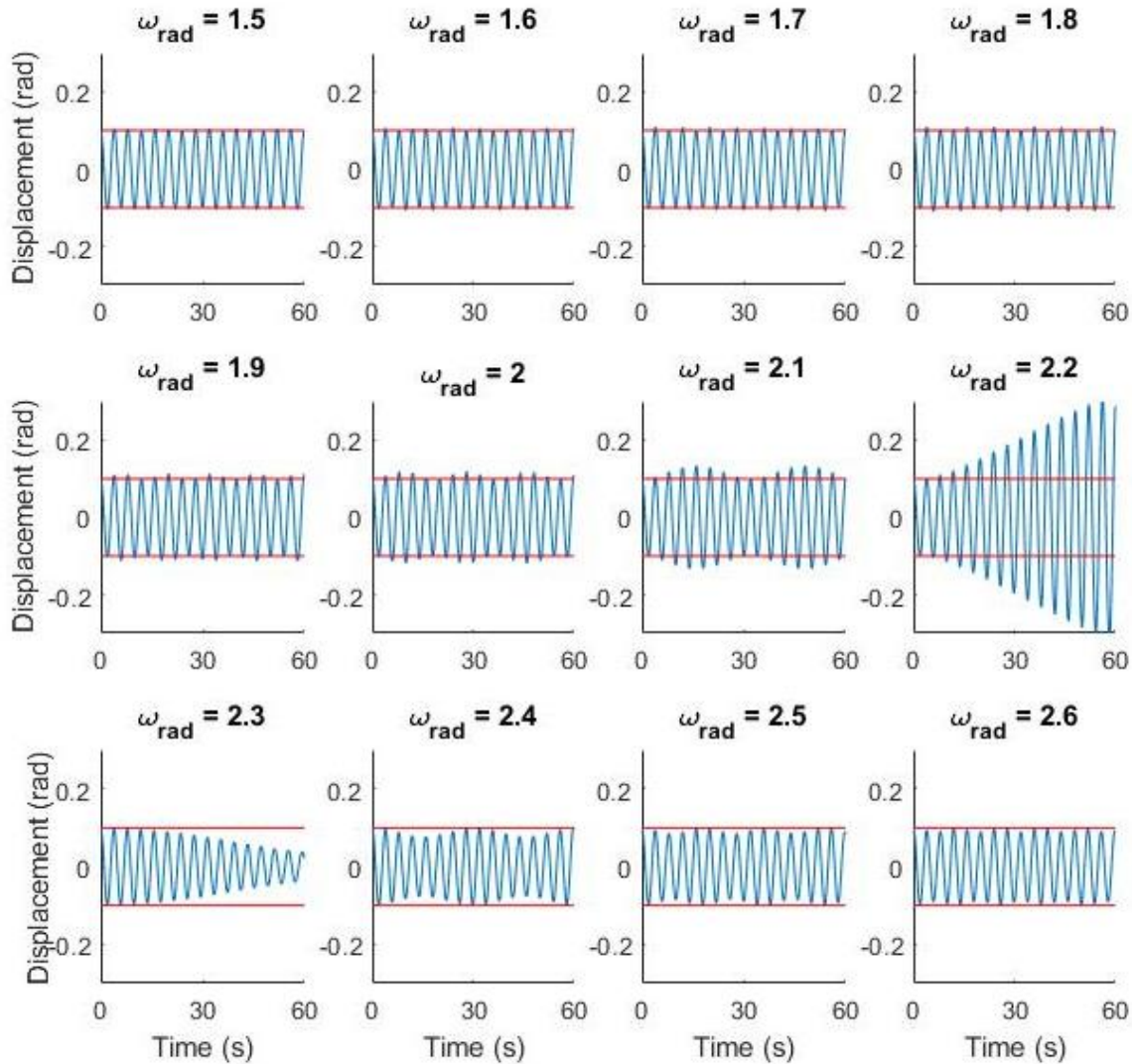


Figure 20: Time Domain plot of the Mathieu Equation Test with a GM Variation of 25%

2.6 Closing Remarks

In each of these applications, parametric excitation was shown to be preserved within the numerical modelling techniques used in their work. This work will use similar techniques to perform time domain numerical simulations assessing the power production implications of the geometric control scheme detailed in the following section, focusing on parasitic parametric excitation in the roll/pitch DoFs.

The dynamics of floating bodies can be more simply represented with the previously stated linear dynamics model but non-linear models are able to capture a more accurate representation of the system dynamics with the cost of higher complexity. Non-linear drag is an example of one of the common non-linear aspects of floating bodies, while linear drag is easily calculated the

non-linear representation tends to be more accurate but comes at a high computational cost. This thesis will use a combination of linear and non-linear dynamics in order to find a balance between accuracy and complexity to assess the implications of adding geometric control to a SRPA.

Chapter 3 Model Parameters

Chapter 3 will present the static parameters of the numerical representation of the 1/25th scale physical model and henceforth the term model/modelling will refer to the numerical model if not specified otherwise. Presented first is the role that numerical modelling plays in the realm of WECs followed by an introduction to modelling techniques used to analyze WECs, addressing the reasoning for using a numerically simulated model. The physical parameters that are to be implemented into the numerical model are presented next and will be split into three subsections: environmental parameters including simulation and fluid parameters, mass and surface geometry, and the VIS connections and friction. Following the physical parameters this chapter will outline the hydrodynamics to be used within the model outlining each contribution. Lastly the natural frequency of different configurations of the system are presented to give a reference point for comparison with the results with respects to parametric excitation. If parametric excitation follows previously presented theory, rolling motions should be present at wave frequencies twice that of the roll natural frequency of the system.

3.1 Role of Numerical Modelling for WECs

In the international context, there is no evidence of ocean energy breaching the commercial energy market on a purely competitive basis; it has been demonstrated, but such early stage operations have been short term, relatively small capacity and required a disproportionately high capital investment offset that was typically offset through public grants or subsidies. In the broader context of ocean energy (ocean winds waves and tides), relatively short term deployments have been funded from public grants, and tidal energy specifically has been subsidized by feed-in-tariffs such as those provided for in the Nova Scotia Marine Renewable Energy Act [2]. Device development of WECs are not largely being driven by iterative (trial and

error) learning process associated with real world deployments. Rather, numerical modelling techniques has been utilized to advance knowledge of how to improve or assess performance of a WEC design [62]. Validation is still achieved through scale physical modelling but design is typically performed with a type of numerical modelling. Numerical modelling provides a way to test technology without large capital investment, allows for development without the cost of prototyping.

The simplified illustrative test case studying the effects of an internally altered parameter studied in Chapter 2 is only a basic look at how a submerged cylinder could be susceptible to parametric excitation. In this chapter, the numerical model of the 2-body and 3-body WECs that are the focus of this work are described to contain a much higher level of complexity such as:

- Six degrees of freedom
- Three dynamically-coupled bodies – a float, spar and internal oscillating reaction mass.
- Damping in the PTO connected between the two bodies as well as relative travel constraints
- Both of the bodies and the waves are in motion
- Complex hull geometry – the spar has a non-uniform cross section resulting in complex distributing force of a moving fluid
- Dynamic waterplane area and thus a heave dependent buoyant force

All of these complexities must be preserved within the modelling method that is to be implemented so as to observe the system response to parametric excitation that is known to exist within the system. Recent work in the wave energy sector, detailed more in the following section, has shown that numerical models need not sacrifice the salient features of a complex ocean energy system. The goal of this work is to investigate the system response subject to all real-world complexities mentioned above.

For a numerical model there are several required parameters including physical parameters of size, shape and mass distribution as well as any controllable parameters to program into the numerical simulation software, ProteusDS, used for this work. The next two chapters will outline the numerical model developed and utilized in this work. Chapter 3 will first overview the modelling techniques used in WEC modelling then outline the static parameters of the system

while the following, **Error! Reference source not found.** will outline the dynamic control parameters.

3.2 WEC Dynamics Modelling

The dynamics modelling of a WEC can be completed at a multitude of fidelities, a few methods and performed in either the time or frequency domain delineating types of each method. Three major methods can be identified as analytical, empirical/physical and numerical.

Analytical methods are closed form solutions to the governing equations of motion of the system, where changes in the system or environment can be expressed as a mathematical functions often generalized or simplified. To complete these closed forms, the representation of the environment and body dynamics must be linearized and typically confined to a single DoF. Analytical methods are additionally largely contained in the frequency domain. Analytical methods tend to be quick as computers can execute closed form mathematical equations with great speed and precision although they are only as accurate as their mathematical approximations, limited to linear regular wave steady state response as to simplify the physics and DoFs. Bubbar et al. and Falnes et al. are the more recent analytical representations of SRPA type WECs in the frequency domain, limited to only the heave DoF and provide some insight into the PTO settings need to be adjusted to optimize power production. Orszaghova et al. is one of the few analytical analysis papers on point absorber type WECs that incorporates multiple degrees of freedom, providing insight into how parametric excitation presents itself within 2-DoF of a SBPA.

Empirical methods, or physical modelling, is modelling or calculations based on experimental or observational data using a physical representation. Empirical methods require a significant amount of testing to create the data needed and are only as accurate as the accuracy of the testing methods. Scale modelling is most common as it allows an economical way to test a design. The scaling of the design however requires a sacrifice of accuracy as all parameters cannot be scaled with equal accuracy, discussed more in Section 5.1. Additionally, sub-systems such as a PTO and VIS can often not be scaled down without compromising the dynamics with such aspects as friction which does not follow scaling laws. Physical modelling is performed under two conditions: regular and irregular waves. Regular wave testing results in a steady state response that is measured and considered to be a frequency domain analysis. Irregular wave

testing provides a more akin relation to actual wave environments and are considered to be a time domain analysis. Beatty et al. performed 6-DoF experimental testing coupled with numerical simulations on a moored SRPA type WEC with a comparison of the two methods showing it is possible to get numerical methods to match the results of experimental modelling [39].

Numerical models tend to require a significant amount of computing power to generate high fidelity models, are performed in the time domain and often incorporate aspects from analytical and empirical methods separated in different ‘layers’ or aspects of dynamics of the system such as separate hydrodynamic forces and representation of the PTO. For example accepted methods in numerical approaches involve using a Morison approximation to the drag and added mass, while at the same time using an inviscid fluid model to derive wave diffraction and radiation effects [63]. The layers are then assembled into one overall model of the interaction of device and fluid. Numerical methods, for time domain simulation, use a time-stepping procedure to propagate a mathematical system, with the inclusion of each layer, forward in time. Bailey et al., Kurniawan et al. and Henriques et al. performed numerical simulations of a floating oscillating water column, a complex system with compressible fluids (air) and wave interactions [63]–[65]. Beatty et al. performed numerical simulations on two similar but different types of SRPA WECs [39] while Babarit et al. performed numerical simulations on eight widely different WECs [66], both works simulated the WECs with moorings and full 6-DoF motion. Each of these examples incorporate the high complexity of each system, the interactions between different components and utilize numerical simulation to do so as it preserves the dynamics of all considered elements.

Computational fluid dynamics is another form of numerical modelling where the fluid domain is discretized and governing equations solved for each discretized point [67]. There are still limitations to accuracy based on the governing equations but this method tend to be computationally expensive and requires a significant amount of time [68]. For the wide range of regular waves to be analyzed in 6-DoF motion the time requirement would be too great to consider this type of numerical modelling as a viable option.

ProteusDS, developed by Dynamic Systems Analysis, is a semi-empirical mesh-based numerical solver which uses analytical and empirical data generated at a pre-processing stage to complete its hydrodynamic calculations. ProteusDS can assess the dynamics of floating bodies, mooring lines, and articulated assemblies of components by numerically solving each layer of

the system and then the system as a whole. Kinematic and dynamic constraints can be applied between bodies and cables in order to enforce the kinematic restrictions of the joints. The system state is advanced in time using explicit and adaptive time stepping techniques like the Runge-Kutta order 4-5 method (the same as MATLAB ode45) [69]. Typical time steps of the simulations in this work are 0.01 seconds taking an average of 35 seconds to simulate each second. Other works have generated their own numerical simulations in order to solve for their own complex systems, each one unique to their system and only usable for that system [34], [35], [38], [50], [52], [53], [70]–[73]. ProteusDS is flexible as it works in terms of the fundamental equations of motion for rigid bodies, and so it can be used to simulate the dynamics of a wide range of floating, articulated systems. The cost for the generality of application is a complex internal method of ‘joining’ bodies together. As the dynamic equations are not constrained to a specific system, it allows for a single platform to access each of these systems with repeatability and a known, well documented implementation of governing principles [69]

Other work such as Bailey et al., Roy et al. and Ortiz et al. have implemented complex WECs with active control and verified ProteusDS [40], [63], [68]. Given the complexity of the internal VIS system, and the goal of investigating a complex response phenomenon like parametric excitation, ProteusDS is an ideal platform from which to execute numerical simulations.

This work will use the software package ProteusDS to execute the hydrodynamic numerical simulations of the 2 and 3-body WEC previously outlined in Chapter 1. The following sections will outline the options and parameters used within ProteusDS to simulate the 3-body SRPA WEC dynamics.

3.3 Physical Parameters

This section is meant to provide an overview of how the ProteusDS model of the VISWEC is completed including the environmental and simulation parameters, Mass and geometry of each body and the implementation of the VIS. There will be some specific references to parameters in the ProteusDS software meant to inform future work on the system or that similar to it.

3.3.1 Environmental and Simulation Parameters

The model being investigated is a 1/25th scale model as stated in Chapter 1, the simulation will also be executed at 1/25th scale and thus a higher level of precision in the calculation of

some hydrodynamic effects, than that of full scale simulation, is necessary. Two general categories can be altered to obtain a higher precision: the numerical simulation parameters and environmental parameters. Typically numerical simulation parameters address stabilization of the system while environmental parameters address the precision of the fluid calculations.

Simulation Parameters

Simulation parameters include the type of integrator, maximum and minimum time step and truncation error. The parameter name, default value and value used are presented in Table 2 accompanied with an explanation of what the parameter controls. The start time and end time are chosen as to give enough time to allow the system to reach a steady state, a conservative number would be the default value of 60 seconds, 180 seconds would ensure a steady state and allow the final 60 seconds to be analyzed. The adaptive 4th/5th Runge-Kutta allows the time step to vary based in the truncation error value calculated by the difference between the 4th and 5th order approximation. The minimum and maximum time step define the range of time steps allowable by the integrator. The maximum time step was decreased in order to ensure no change in the dynamics were missed even by the 5th order approximation as well as match the update period of the fluid domain. The truncation error is used to capture high frequency dynamics typically seen in mooring lines where truncation error is reduced to $1e^{-8}$ although for rigid bodies the default value of $1e^{-4}$ is more than sufficient.

Table 2: Simulation Parameters

Parameter Name	Default Value	Value Used	Parameter Control
\$StartTime	0	0	Absolute time value of the start time of the simulation (seconds)
\$EndTime	60	180	Time at which the simulation will terminate (seconds)
\$IntregationType	1	1	Adaptive 4 th /5 th Runge-Kutta Index choses the type of integrator implemented (unit delineation)
\$MaximumTimeStep	1	0.01	Maximum time step allowable of the integrator (seconds)
\$MinimumTimeStep	$1e^{-15}$	$1e^{-15}$	Minimum time step allowable of the integrator (seconds)
\$TruncationError	$1e^{-4}$	$1e^{-4}$	Error tolerance in adaptive temporal integrators, smaller the value the conservative the time step shrinks to add high frequency dynamics (multi-unit)

Fluid Environmental Parameters

Environmental parameters outline the values to be used in the calculations of environmental forcing. This work will only consider the forcing of the wave field on the body, as such currents and wind are not considered. The parameters listed in Table 3 show the values that are altered from the default value with the exception of the wave height and period that are outlined in Table 11. The water depth is changed from default as to reflect a scale depth typical deployment and a depth typically of a wave testing tank. The water density is also changed as to reflect a wave testing tank as to allow validation with physical wave tank testing. The wave type is chosen as to reflect a regular airy wave to impose linear waves upon the bodies as investigate a single wave field. The precision of the fluid surrounding the bodies are defaulted to reflect the simulation of a full scale device although since the simulations will be at 1/25th scale the fluid discretization will need to reflect the scale. The fluid domain is increased by an order of magnitude reducing the size between calculated points from 0.01 to 0.001. The final parameter controls the time period that the discretized fluid domain, previous parameter, is updated and should be small enough to resolve the smallest wave periods or at least twice the wave period that may influence the system dynamics. Testing the meshes described in the following section revealed that without the precision parameters, previous two parameters, the meshes would not stabilize (i.e. transient and long lasting motions were large).

Table 3: Environmental Parameters

Parameter Name	Default Value	Value Used	Parameter Control
\$WaterDepth	1000	2	Water depth is used for wave calculation and specify seabed (meters)
\$WaterDensity	1025	1000	Density of water 1000 = fresh water (kg/m ³)
\$WaveType	0	1	Indicated the wave model used 1 indicates Airy waves
\$FluidDomainPrecision	2	3	Digits of precision used to specify the fluid domain discrete bin size (order of magnitude)
\$FluidDomainUpdatePeriod	0.1	0.01	Time period that the discretized fluid domain is updated (seconds)

3.3.2 Mass and Surface Geometry Models – Float and Spar

ProteusDS requires a separate specification of geometry and mass, meaning that any shape/size can be assigned any inertial properties. The surface geometry is used for hydrostatic and hydrodynamic force evaluations while the mass properties are used to quantify the reaction of the body. The design of the physical model of the Float and Spar was executed within SolidWorks where the geometry and mass of all components are specified, the 2-body and 3-body configuration having the same physical geometry and parameters [74]. The physical parameters of the system were extracted from this design including geometry, mass and center of gravity as shown in Table 4, Figure 23, and Figure 24. The mass and inertial properties presented in Table 4 show the mass of the Float and Spar as well as the moment of inertia in the roll (I_x), pitch (I_y), and yaw (I_z).

Table 4: Mass and Moment of Inertia

	Mass (kg)	Moment of Inertia (kg m ²)		
		I _x	I _y	I _z
Float	16.8	0.22	0.22	0.39
Spar	274.13	18.47	18.47	4.51

To be able to simulate a rigid body in ProteusDS, the geometry needs to be defined by a surface mesh comprised of discrete panel elements. Simpler shape meshes can be generated within ProteusDS though more complicated geometries require third party mesh generating software. Custom polyhedral meshes are typically comprised of triangles and quadrilaterals defined by nodes/vertices and edges/segments.

A panel representation of the surface is used inside the calculation of some hydrodynamic effects allowing for additional but more accurate calculations than that of a single equation for a generalized shape. As an example, a cube geometry can be divided up into panels and each panel's area evaluated individually, applied at its center of area, these forces are then summed to get a total force contribution.

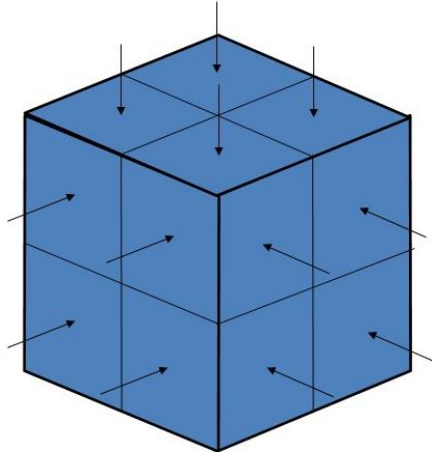


Figure 21: Example of panel based evaluation, if this cube was submerged the net buoyancy force could be evaluated by integrating the hydrostatic pressure over the surface

A mesh generating software, MultiSurf was used to generate the mesh of the hull to be used in ProteusDS [75]. Using the exterior dimensions, a cross section cut down the vertical axis was created in SolidWorks and exported to MultiSurf, shown in Figure 24 and Figure 24. The profile was then revolved around the same vertical axis with a specified number of rotations; i.e. four rotations would create a square, eight rotations an octagon as shown in Figure 22. Multiples of four were considered in attempt to keep each quadrant symmetric. This process created a rough geometry where the axial segments, or vertical segments would then need specification. The quantity of axial segments should conserve equilateral mesh panels as can be seen in Figure 23 and Figure 24 to capture the discretized fluid calculations. In order to import the mesh generated in MultiSurf, Rhinoceros 3D (another mesh editing software suggested by ProteusDS) was used to convert the file into a ProteusDS readable file type.

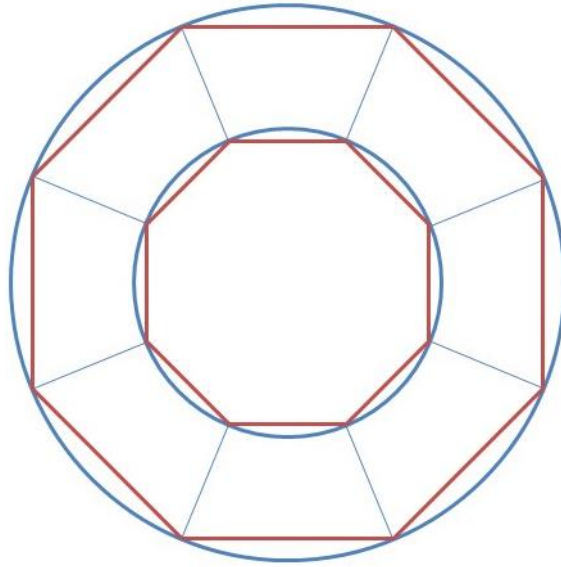


Figure 22: Circular shape represented by an octagon, this is an example of the top view of the Float represented by a mesh with eight radial segments

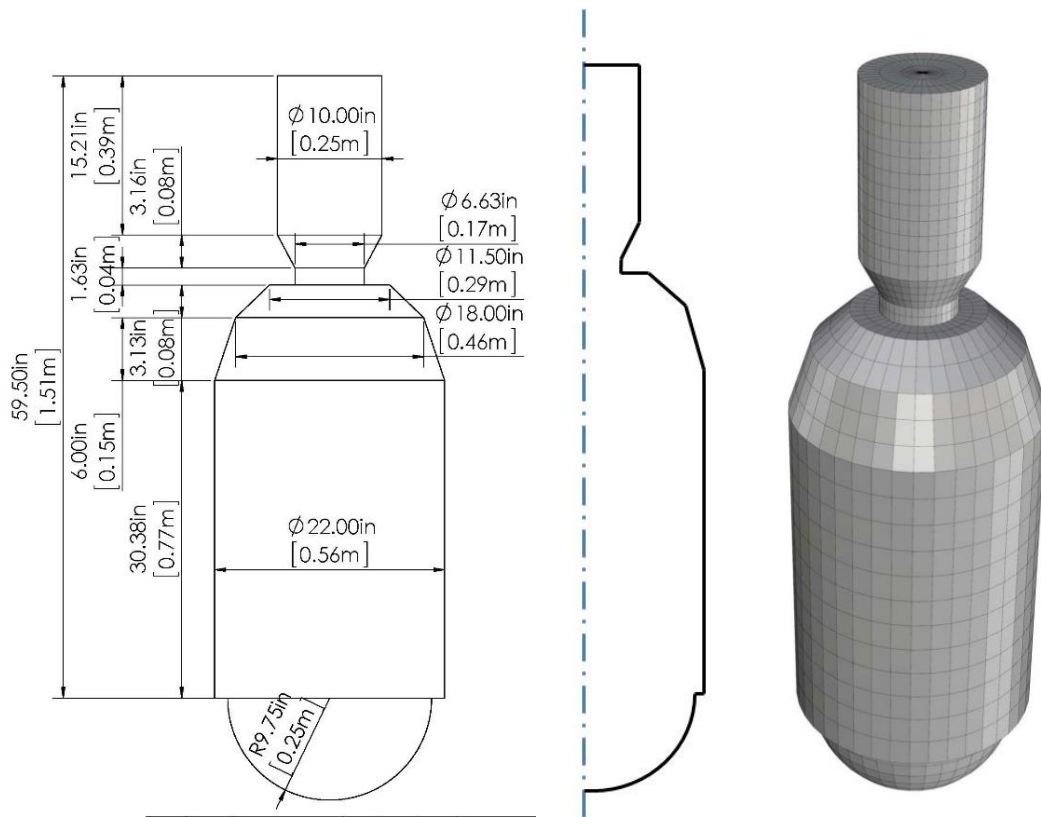


Figure 23: Physical geometry of Spar

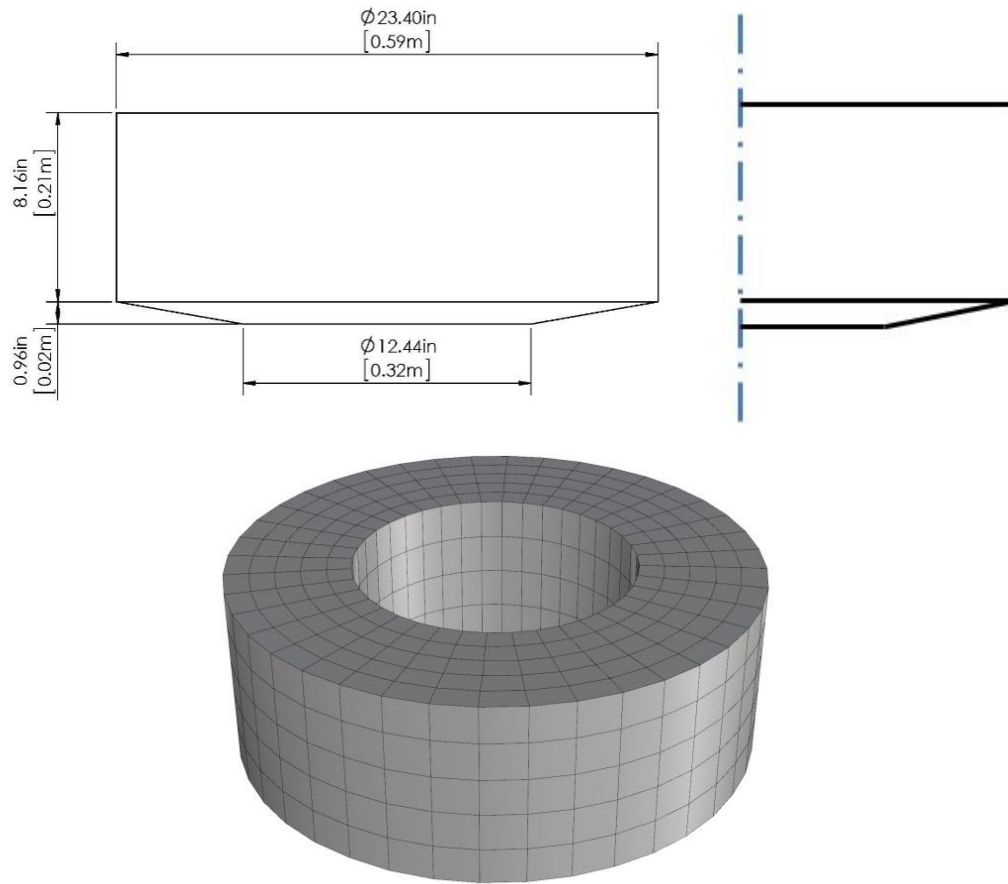


Figure 24: Physical geometry of Float

To ensure that a properly resolved mesh was used, a mesh convergence analysis was performed. For this analysis, a simple simulation with no waves, no current and no winds was initialized. The meshes were placed with zero initial displacements and allowed to move into its equilibrium condition over 180 seconds. Each simulation used the same hydrodynamic component models - discussed further in Section 3.4 Hydrodynamics. Each body, Float and Spar, were allowed to move separately as to allow for the possibility of each body having an optimal mesh. The comparison of the range of meshes considered for the model is shown in Table 5, Table each mesh is defined by the number of radial segments used. These simulations were then compared on the basis of:

- 1) The metric of maximum displacement is calculated by taking the distance of the mesh in its final state from the origin.

- 2) The yaw metric is a measurement in degrees of how much the mesh has rotated about the z-axis. Since the only resistive force in yaw is skin friction for an axisymmetric body, any uneven forcing on the mesh will cause the body to spin.
- 3) The volume difference in percentage originates from representing a circle with a polygon with as many sides as radial segments, as can be seen in Figure 22, the volume of the mesh was compared to the true volume of the shell and the percent difference recorded.
- 4) The number of polygons is a metric of size and effects the number of computations required for each iteration of the mesh.
- 5) Computation time is the amount of time to execute the simulation under identical conditions meaning the same processor with the same number of cores, same amount of random access memory (RAM) and no other programs running.

Table 5 : Mesh Comparison

Radial Segments	Float				Spar				Total Comp. Time (s)
	Max Disp. (mm)	Yaw (Deg)	Vol. (-%)	# of Polys	Max Disp. (mm)	Yaw (Deg)	Vol. (-%)	# of Polys	
12	47	38	38.7%	144	10	5	4.9%	276	859
20	28	165	36.7%	320	0	2	1.7%	980	1679
32	19	297	0.8%	640	28	0	0.7%	1600	5542
40	5	236	0.4%	800	21	0	0.4%	2000	2858
48	16	261	0.3%	1056	14	0	0.3%	4175	16443
60	5	234	0.1%	1800	3	0	0.2%	5576	8395
80	35	544	0.4%	3200	13	0	0.1%	7835	10489

The values in Table 5 are a result of approximation errors of the integration of hydrostatic force in the simulation and/or small inconsistencies in the mesh that can originate from approximation of decimal places in the conversion of mesh files. The Float has a smaller mass and hence is more easily moved hence the larger displacement values. Poor performance is indicated by the more red values.

The mesh with 40 radial segment was used as it performed best overall, being a balance between accuracy and computational expense. Additional drag in the yaw DoF was added into

the final simulations in order to reduce the amount of spinning about that axis, this is discussed more in Section 3.4.3 Drag. The time series of the final selection is shown in Figure 25. The instabilities experienced within the final selected mesh reflects the difficulty ProteusDS experiences due to integration errors of hydrostatic buoyancy. Even with these errors the mesh is able to remain within 25 cm of the original position and 0.2 degrees of the original orientation save for the yaw of the Float.

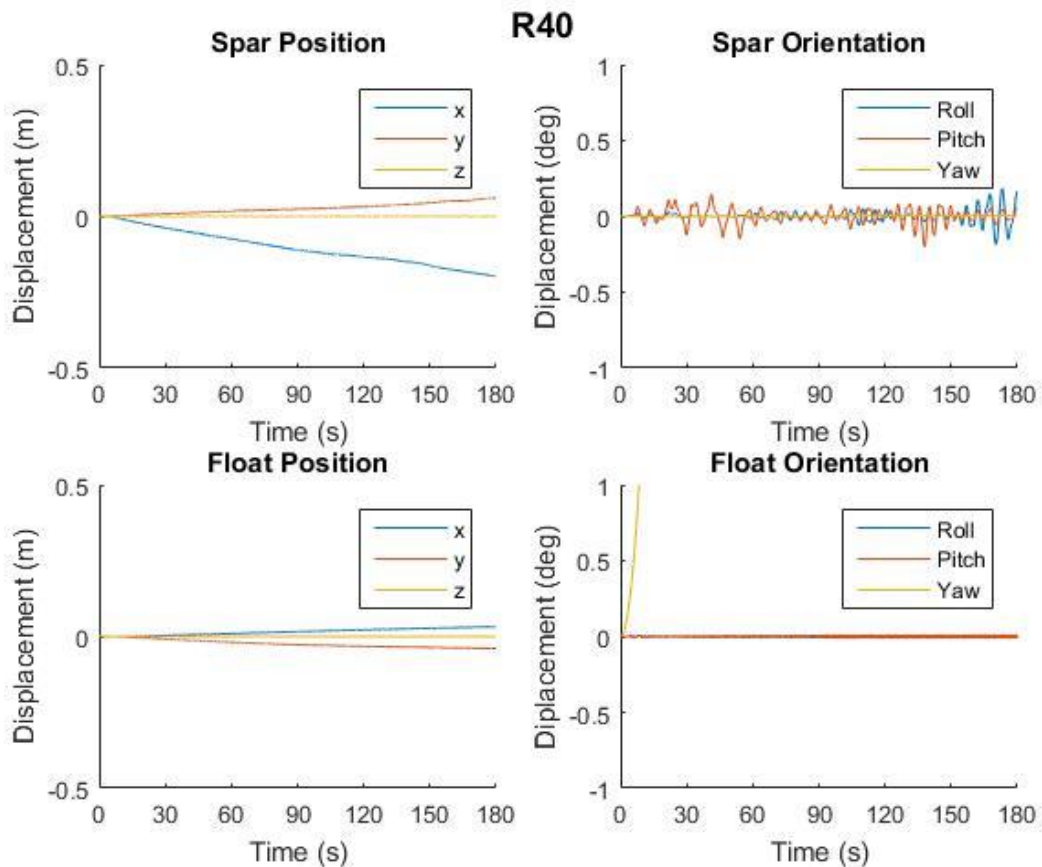


Figure 25: Results of the chosen mesh in the time domain

3.3.3 Variable Inertial System

The VIS is defined by the physical parameters and the connections that exist between the components within. Within the connections exist a quantifiable amount a friction that will dampen the motion of the VIS. This section will be split into two sub-sections, first defining the connections and physical parameters and second the friction contained within the system.

Connections

The 2-body configuration is accomplished by locking down the VIS so that the Spar and VIS react as a single body. The VIS, in the physical model, as described in Section 1.5.3, has a Reaction Mass weighing 132.86 kg, supported by three springs. Each spring has a constant of 1996.3N/m for a total of 5889.6 N/m connected between the Spar and the Reaction Mass.

The addition of the VIS into the ProteusDS model of the point absorber system required two additional rigid bodies, the Reaction Mass and ballscrew, and three additional connection constraints defining how these two rigid bodies were linked kinematically to the motion of the central spar. The Reaction Mass is connected to the Spar via the spring linearly guided and connected to the helical ballscrew. The ballscrew, with variable rotational inertia, is connected to the Spar through ball bearings allowing rotation around the z-axis. Proteus has two main types of connections for rigid bodies, articulated-body-algorithm (ABA) joint connections and force constrained connections.

The ABA type connection refers to a joint connection with specific degrees of freedom allowed between the two connected bodies. Every ABA joint has a ‘master’ body and a ‘follower’ body – the motion of the follower is such that it matches the motion of the master plus additional translations or rotations due to the joint. Those additional motions are determined using the articulated-body-algorithm which determines the inertial resistance to those joint motions due to the particular pose of the system. Similar to a guide rail, a Prismatic joint can only slide along a single linear axis and a Revolute joint would be like a bearing only able to rotate around a single axis with no other movement. A helical joint defines the amount of rotation per linear unit between the two bodies. Within these connections in ProteusDS, joint properties can be specified to achieve any stiffness, damping, end stops, and actuating forces. The limitation of the ABA joint is that there cannot be a full loop of ABA joints. That is only a tree-like kinematic relationship can exist between those of a series of rigid bodies.

Force connections, like ABA connections, exist across specific degrees of freedom between two bodies although there is no master and follower relationship. Rather, stiffness and damping coefficients assigned to the joint DoF create an action-reaction force (or moment) pair between the connected bodies. Force joints can be used to achieve pseudo-rigid connections if stiffness and damping coefficients are applied that are large enough to prohibit unwanted movement between the two bodies; however if these values are too large it can cause computation time to

increase greatly due to high frequency, low amplitude vibrations in the joint between the two bodies. A force connection is required to complete the loop of connections within the VIS as shown in Figure 26 overcoming the limits of ABA connections.

The connections in the VISWEC system can be visualized in Figure 26 and the properties that correspond in Table 6. The PTO and rotational inertial of the ballscrew values are discussed in Chapter 4. The spring stiffness value of connection 2 matches the spring stiffness value of the physical model and the dampening friction is discussed in the following section. The lead of the helical connection matches the ballscrew used in the physical model of 0.032 meters per revolution and the stiffness and dampening of connection 4 was chosen based on a quick sensitivity test to ensure no unwanted movement as well as a reasonable simulation time.

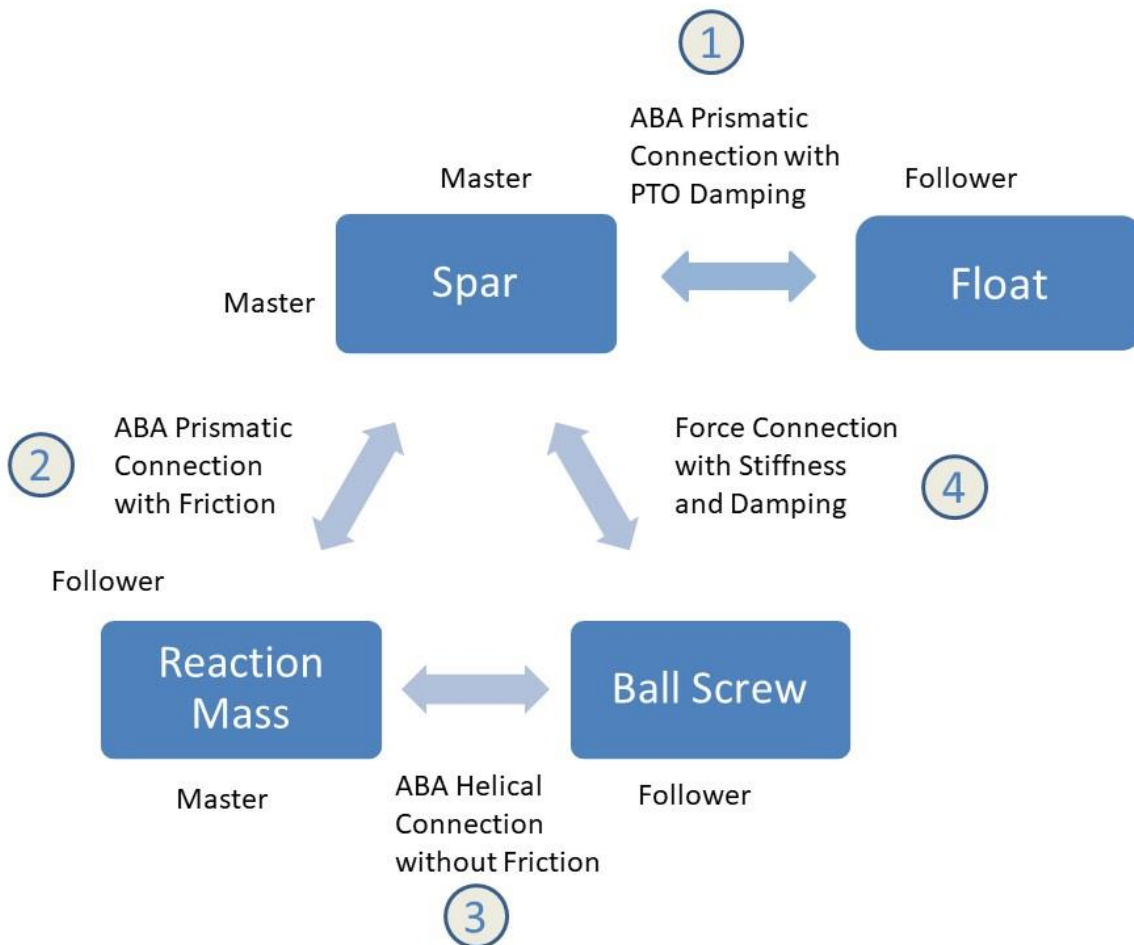
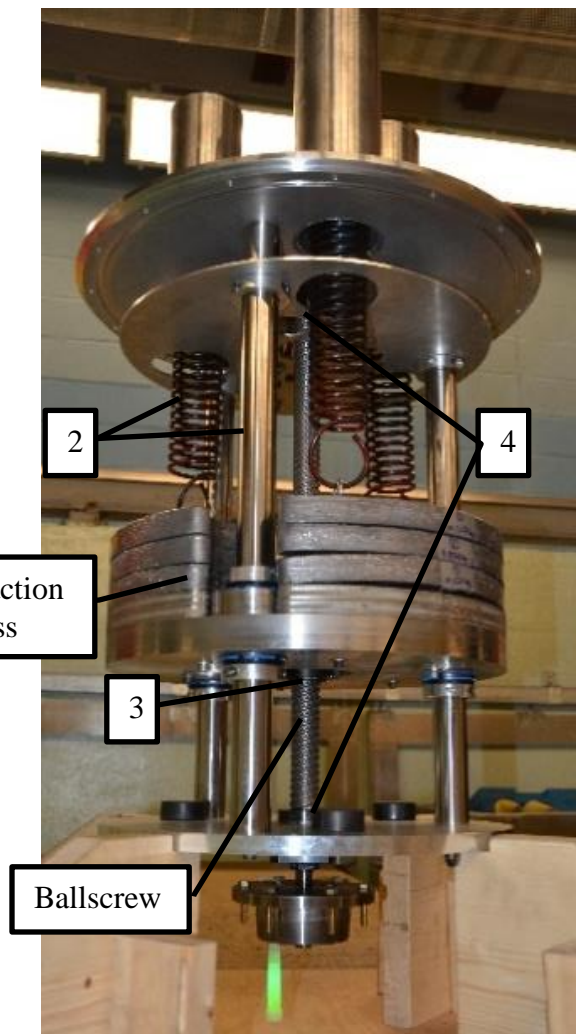
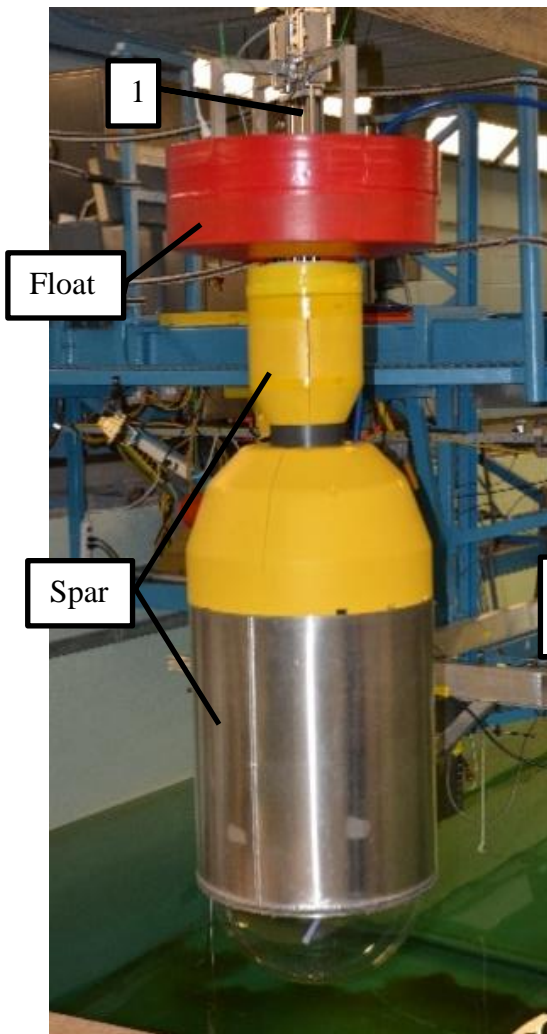


Figure 26: Connection layout with corresponding numbers to Table 6

Table 6: Point Absorber and VIS Connection Properties

#	Connection	Type	Master	Follower	Properties	Value
1	ABA	Pismatic z-axis	Spar	Float	Damping	PTO Value
2	ABA	Pismatic z-axis	Spar	Reaction Mass	Spring Stiffness Damping Friction	5889.6 N/m 84.32 Ns/m
3	ABA	Helical z-axis	Reaction Mass	Ballscrew	Lead Damping Friction	0.032 m/rev None
4	Force	Unconstrained z-axis	Spar	Ballscrew	Spring Stiffness Damping Lead	100,000 N/m 1,000 Ns/m 0.032 m/rev

a)



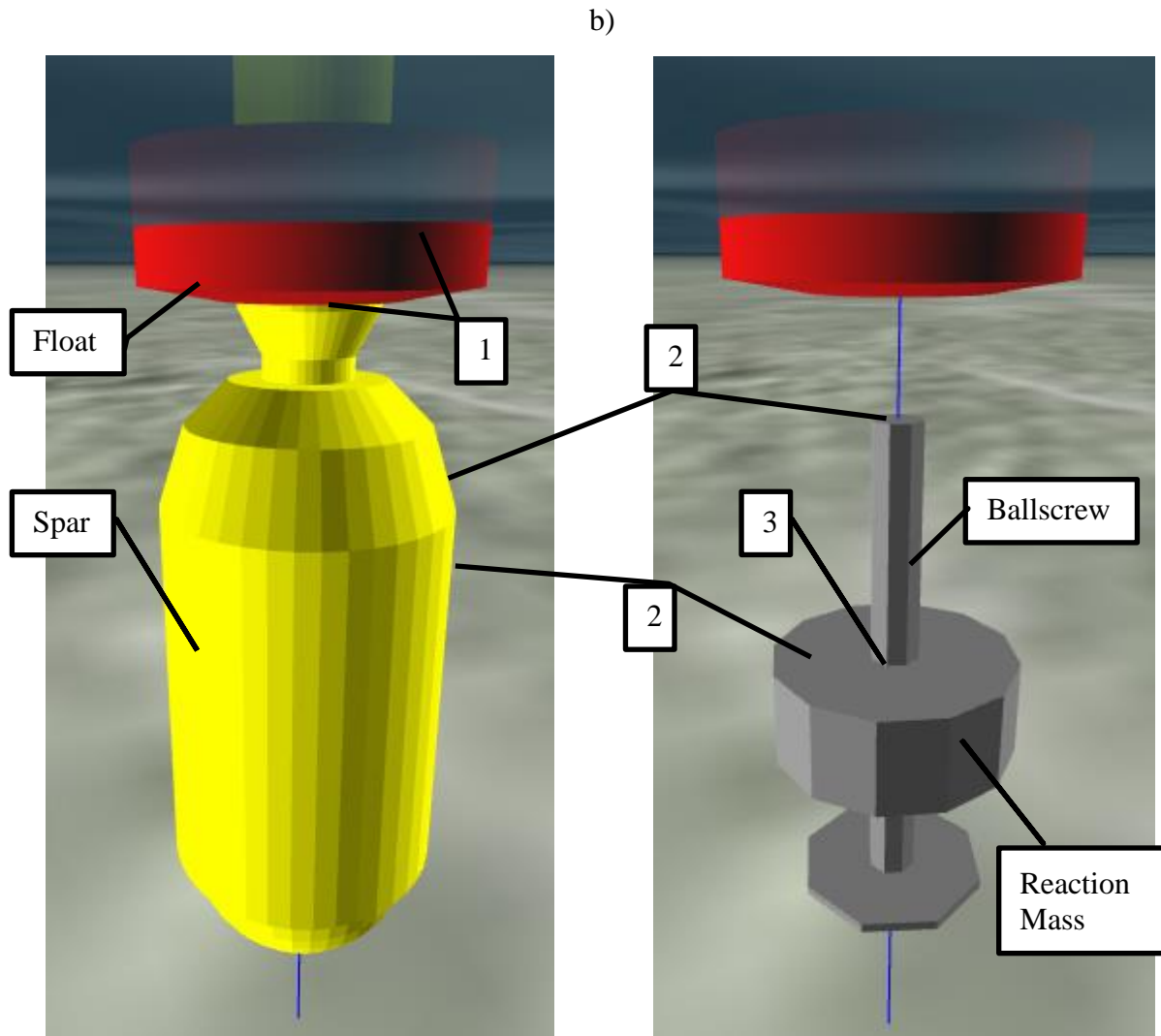


Figure 27: The full VISWEC and VIS with labeled bodies and connection numbers shown as a) physical model and b) ProteusDS model

Linear Friction Calculation

The damping friction value in connection 2 is representative of all of the friction in the VIS. To quantify the friction in the system, a series of experimental decay tests was performed logging the position over time at four different settings to get a domain of a range of settings. The setup was then replicated in ProteusDS with the connections shown in the previous section and a linear friction damping value chosen to closely match the decay of the experimental decay test. A value of 84.32 Ns/m was found to most closely match each of the settings, the value was gradually increased until the peaks matched the experimental results. The deviation from the experimental results at the low amplitude oscillations toward the end of the decay are due to the

growth in coulombic friction, or static friction, which is modeled as a constant resistive force. Static friction was omitted from the simulation for two reasons; first, the inclusion of this friction would reduce the effects of the VIS and thus dilute the final results and the goal of this work. Secondly, in the full scale model static friction would be proportionally less.

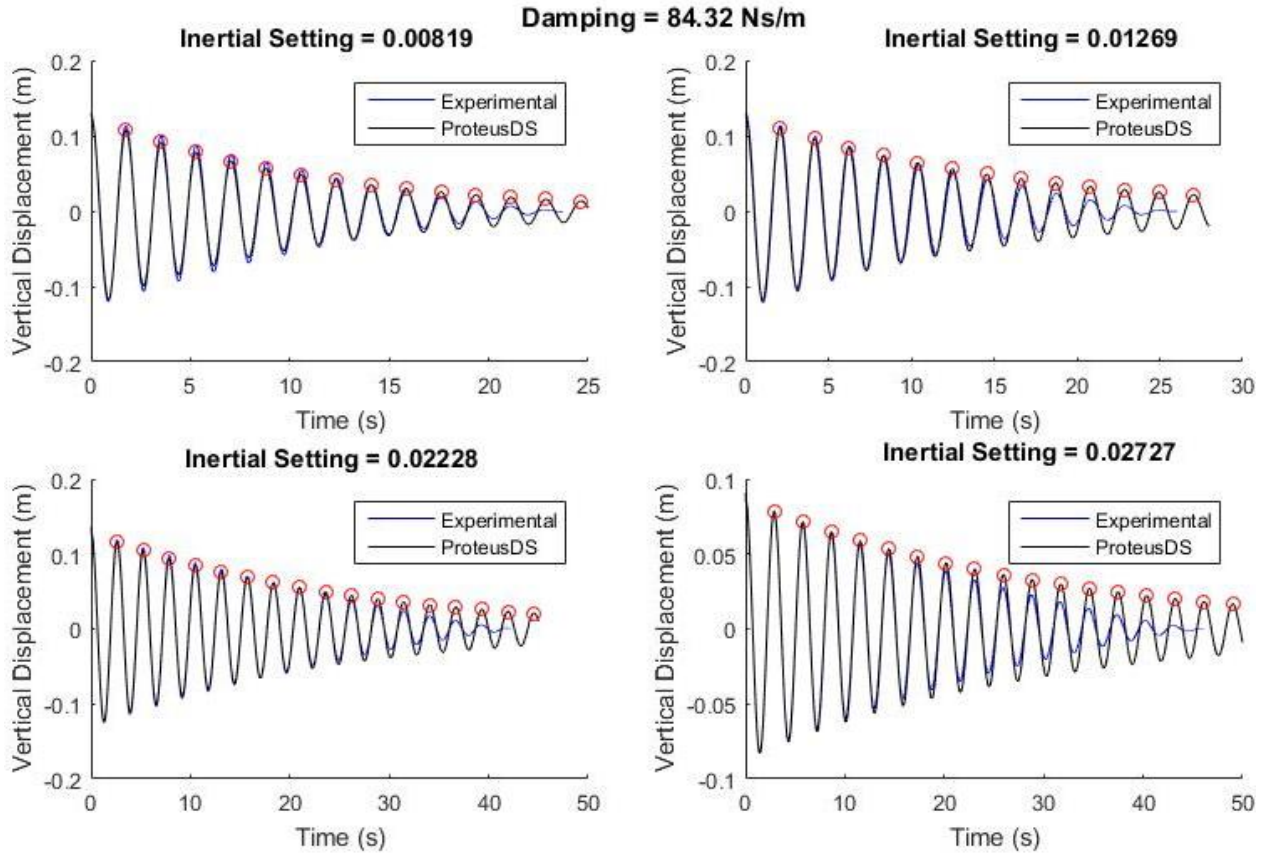


Figure 28: Linearized Friction in VIS the blue lines are the experimental tests and the black line with red circles at the peaks are the ProteusDS simulations of the system. The plots are arranged by inertial setting (kg m^2) of the VIS. Time scales are varied as to full display each plot's full cycle.

3.4 Hydrodynamics

ProteusDS is able to reproduce the Airy wave kinematics that were described in Chapter 2. Within the ProteusDS simulations conducted in this work, the forces generated on a rigid body through the fluid structure interaction are summarized in eq. (3.1):

$$F_T = F_{buoy} + F_{excit} + F_{diff} + F_{rad} + F_{drag} \quad (3.1)$$

where F_{buoy} is the hydrostatic buoyance force contribution, F_{excit} is the wave excitation force contribution, F_{diff} is the contribution from diffraction/scattering, F_{rad} is the contribution from

the radiation force, and F_{drag} is the force contribution from the drag, summing up to the total force on the system F_T .

Each force contribution is individually explained in the following subsections – in terms of both the physical origins of the force and the calculation method ProteusDS uses on each evaluation of the system dynamics. Some hydrodynamics can only be captured within the ProteusDS software package with help of coefficients calculated using external software in a pre-processing stage. As an example, a boundary element method solver such as Wave Analysis Massachusetts Institute of Technology (**WAMIT**) [76] provides data that can be used to determine the frequency based coefficients that are subsequently used in the time domain code ProteusDS to evaluate the radiation forces.

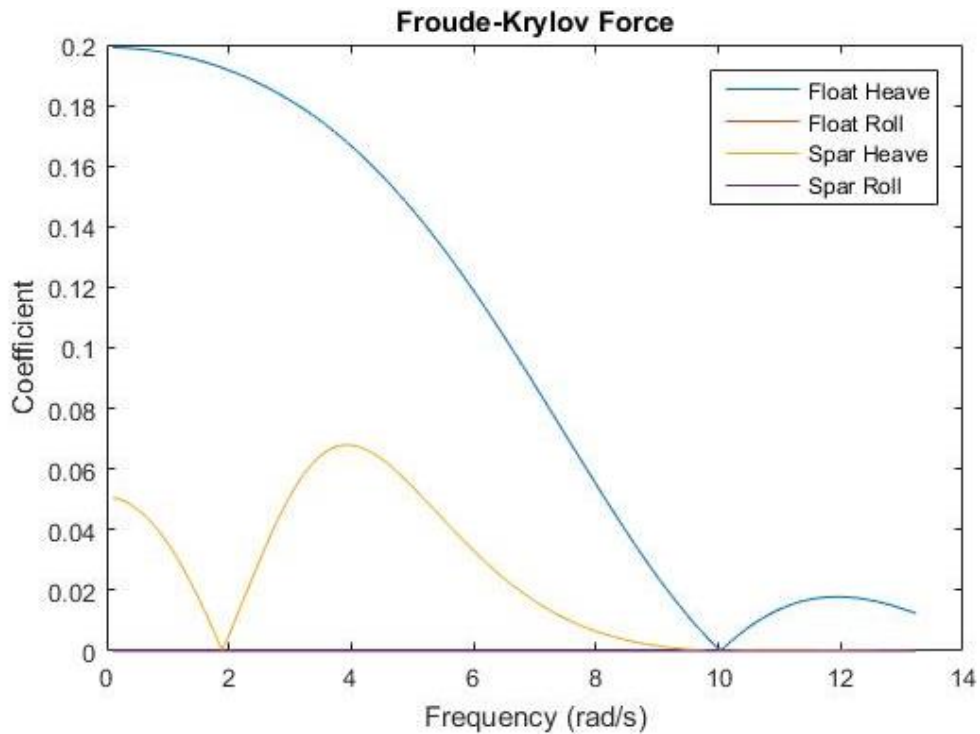
3.4.1 Hydrostatic Buoyancy and Wave Excitation Force

ProteusDS calculates buoyancy and wave excitation by calculating the total pressure contribution at each panel that comprises the surface mesh as described in eq. (2.4). Hydrostatic buoyancy force is the upward force that the fluid exerts on a body through the pressure acting on it after displacing the fluid at a free surface water line. ProteusDS can calculate how much of the structure is wetted, or submerged, as well as the pressures acting upon it from the weight of water. Since pressure is dependent on depth as can be seen in the first part of eq. (2.4), there are different pressures over the structure's exterior geometry. The hydrostatic pressure contribution on each panel of the structure's mesh is calculated, summed and applied to the center of mass. Panels that are partially submerged are split at the waterline and treated as 2 separate panels; this allows for smooth forcing as the waterline changes.

In ProteusDS the contribution of the excitation force from the incident wave is calculated by taking the undisturbed wave pressure field, the second part of eq. (2.4), at the center of each surface mesh panel and multiplying it by the panel area. These forces are then integrated over the surface area, summed and applied to the center of mass. This is total term with the hydrostatic and wave excitation term results in a term referred to as the Froude-Krylov force within the ProteusDS Manual [69] as displayed in Figure 29a. As each panel's contribution is transformed to be applied at the center of mass there is an accompanying moment, this moment is calculated within ProteusDS.

The diffraction, and/or scattering, force is a result of the change in the Airy wave pressure field due to the deformation of the wave field as it passes around an impermeable structure.

These frequency dependent coefficients for the diffraction forces are calculated with WAMIT by running regular waves by a static structure and monitoring the additional velocity potential that must be added to the original one to ensure that the impermeable condition is satisfied. That new potential is then translated into a pressure field through Bernoulli's equation. WAMIT outputs the frequency based force coefficient that scale the wave free surface elevation function to result in the force contribution to the hydrodynamics as displayed in Figure 29b. The values for heave and roll are presented in the following figures to provide examples in relevant DoFs pertaining to parametric excitation.



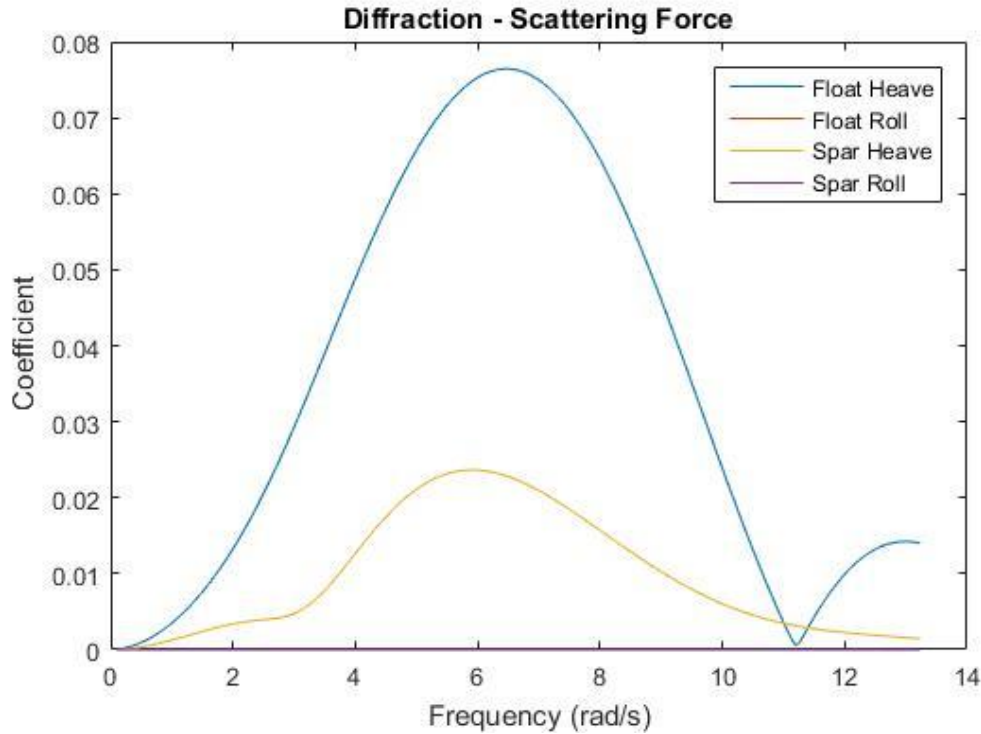


Figure 29: a) Froude Krylov Force coefficient over a span of frequencies b) Scattering Force over a span of frequencies.

3.4.2 Radiation

Radiation forces are calculated at each time step based on the instantaneous body motion and two frequency coefficients provided from WAMIT, added damping $B(\omega)$ and added mass $A(\omega)$ as can be seen in eq. (3.2). There are entries of coefficients output by WAMIT for a 6x6 matrix relating each of the DoFs to each of the others.

In WAMIT the radiation force is calculated by oscillating the body at different frequencies when no waves are present and measuring the resulting force between it and the fluid around it. For a linear system the radiation can be separated into a term based on added mass and a term based on added damping. Added damping is multiplied by velocity and can be visually seen as the waves radiating away from the body. Added mass forms an acceleration dependent force and is a result of fluid moving with the body. WAMIT outputs frequency based coefficients, B and A , for both of these contributions as is displayed in Figure 30. Default values (1) for added mass were changed to zero within ProteusDS due to the implementation of added mass from WAMIT.

$$F_{rad}(\omega) = \omega iB(\omega) + A(\omega)\omega^2 \quad (3.2)$$

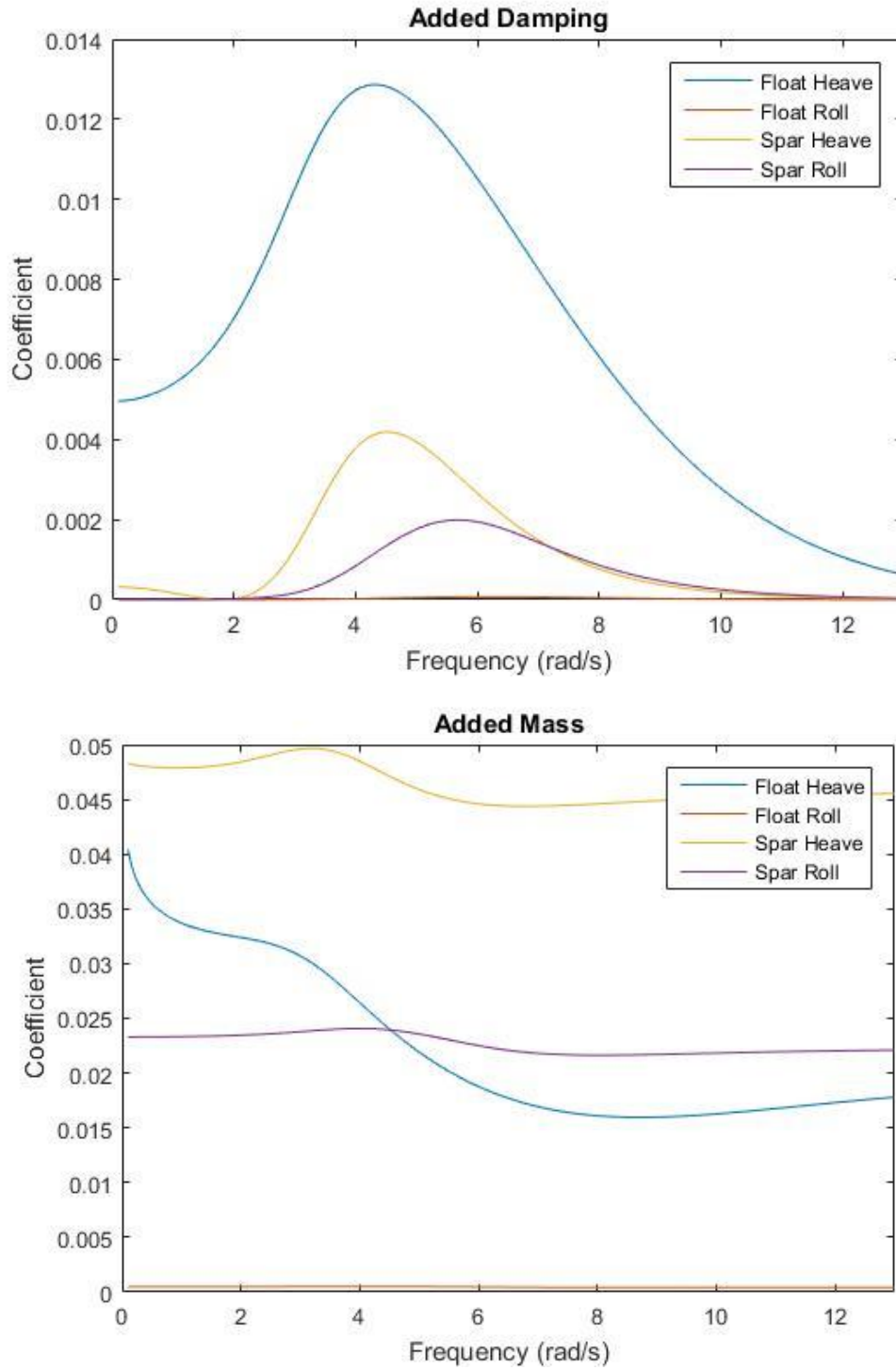


Figure 30: a) Added Damping coefficient and b) Added Mass coefficient for the Float and Spar in roll/pitch and heave over a range of frequencies.

3.4.3 Drag

There are many ways to consider drag force development on the rigid bodies; linear drag force relates a force to a coefficient dependent on the velocity while quadratic drag defines the force using a coefficient multiplied by the square of the velocity. Proteus has the capability to numerically model both linear and quadratic types of drag, implemented by a 6x6 matrix of linear and/or quadratic drag coefficients that use the body's overall velocity to compute the force contribution. Proteus can also calculate the quadratic drag on each panel based on the relative velocity between the water and the individual panel and the projected area.

Quadratic drag is mainly used in the analysis of the WEC and is generally calculated by eq. (3.3), on a panel by panel basis. This creates a distributed series of small forces (one per panel). These forces are summed vectorally to create an overall drag force. Each force also create a moment at the CG and these moments are also totaled. Limitations arise when considering rotational drag as the path of the fluid when compared to a slender or wide object vary from linear to more curved, consider Figure 31, this is discussed more within the Proteus Manual [69].

$$F_{dq} = \frac{1}{2} \rho D_q A_{proj} v |v| \quad (3.3)$$

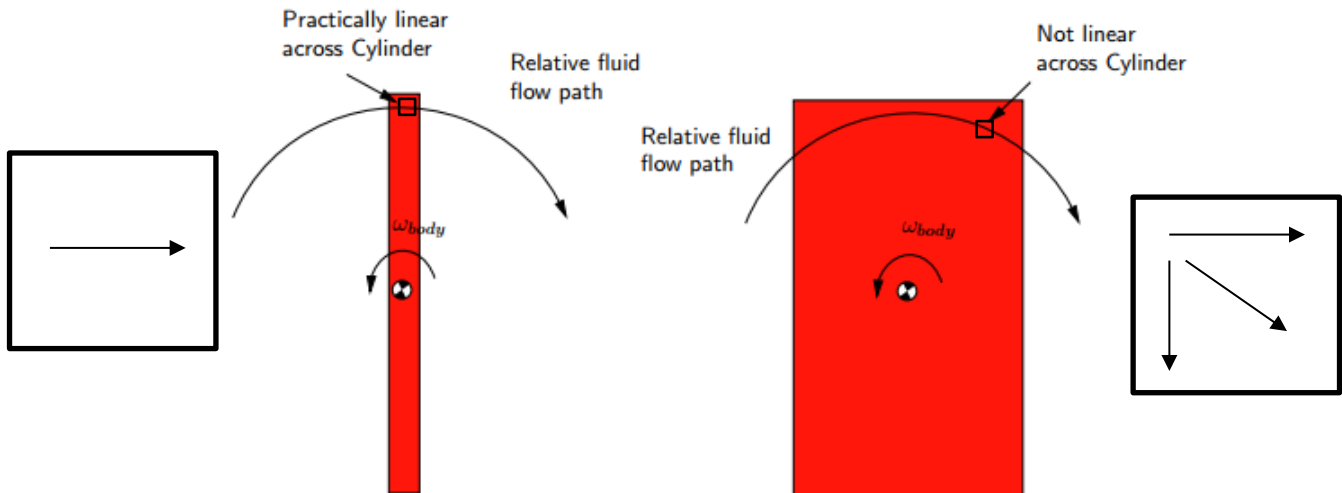


Figure 31: Rotational Limitation, as the width of a rotating body grows the approximation of path begins to not hold, if the body is discretized into panels each panel can be calculated with a linearized assumption [69]

In order to determine a heave drag coefficient to this geometry a series of experimental natural decay tests were necessary where an initial displacement in heave was provided and then allowed to naturally decay. The position was captured with a laser sensor that outputs the distance to a flat surface attached to the Spar. The experimental setup required linear guides to restrict the body to only heaving motions. Within the implementation of the linear guides there was a significant amount of dry friction shown by the drastic decay and gradual decrease in oscillation period of the contaminated experimental results in Figure 32. Dry friction would not be present in the true system and not a desired effect to be modeled in the simulations thus, is ignored in the characterization of drag. The drag coefficients shown in Table 7 were used to produce the simulated results in Figure 32. Skin drag is another type of linear drag but instead of flow into or out of a panel as with traditional quadratic drag, skin drag is based on tangential flow and default values will be used.

Linear drag is added to the yaw DoF due to the rotation experienced in the mesh comparison simulations, this implementation of drag will not affect the dynamics of the system while still limiting the amount of rotation. The other degrees of freedom's drag were left at default values (1) within ProteusDS.

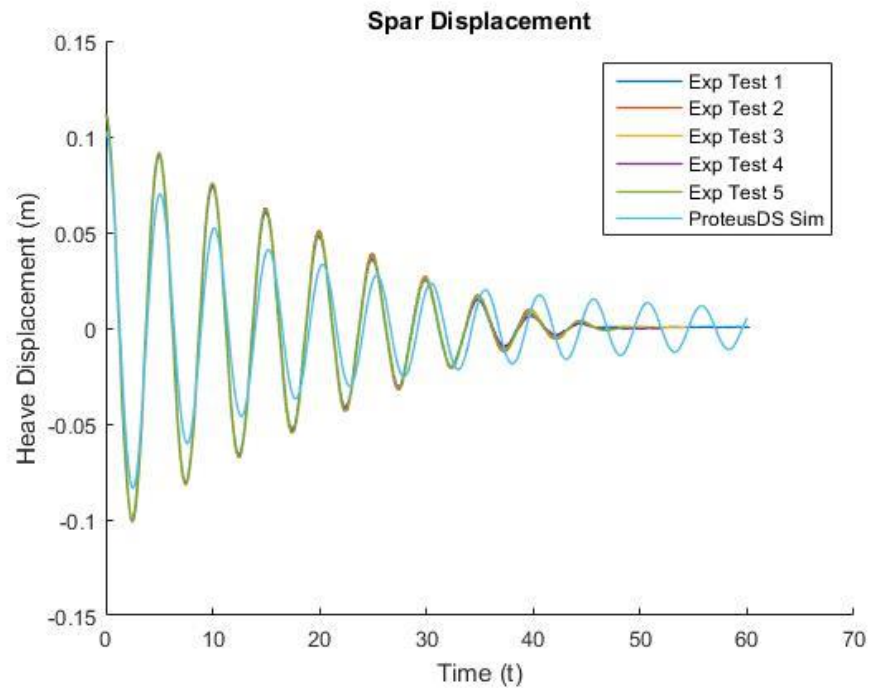


Figure 32: Heave decay plot of experimental results and that of the drag matching achieved through ProteusDS simulation

Table 7: Drag Coefficients

Body	Quad Drag Coeff (x)	Quad Drag Coeff (y)	Quad Drag Coeff (z)	Skin Drag Coeff	Yaw Lin Drag (ψ)
Spar	1	1	1.8	0.2	50
Float	1	1	1	0.2	50

3.5 Natural Frequency

There are two modes of natural frequency that are of concern for parametric excitation and hence this work: heave and roll/pitch. Since both bodies are axisymmetric both the roll and pitch natural frequencies will be equal. There are three cases that can define the limits of the system for these two modes of motion: the two bodies connected axially and concentrically along the z-axis and no resistance, same conditions although rigidly at the point of equilibrium, and the two bodies standing alone.

The testing conditions were setup within ProteusDS using connections for constraints, rigid connection for the locked case, prismatic connection along the z-axis for the connected condition and no connection for stand alone. Hydrodynamic data was implemented akin to the simulations for power production to reflect natural frequencies in the results. Initial conditions of 0.13 meters and 10 degrees perturbation from equilibrium were used for heave and roll/pitch respectively for each body. Simulations were executed with no waves, wind or currents. Natural frequencies were calculated by taking an average frequency (rad/s) between the peaks in oscillation and the results can be seen in Table 8. If the work from Chapter 2 generally holds the results should show parametric excitation at wave frequencies around 2.56 – 2.72 rad/s, twice the natural frequency of pitch/roll. The locked heave natural frequency (2.54 rad/s) will also show where large variations of \overline{GM} will occur. The fact that these two parameters are close may point towards a large response in roll due to parametric excitation.

Table 8: Natural Frequencies Under Different Constraints

Condition	Connected		Locked		Stand Alone	
	Heave	Pitch/ Roll	Heave	Pitch/ Roll	Heave	Pitch/ Roll
Spar	1.24	1.28	2.54	1.36	1.24	1.34
Float	7.97	1.28	2.54	1.36	7.97	8.36

Chapter 4 Model Settings

To properly compare the motions and power production between a 2-body WEC and the new 3-body WEC, it is essential to eliminate inconsistencies between the test conditions of each system. By doing so, changes in performance could be attributed to the internal VIS mechanism. One of the challenges in maintaining consistency between the 2-body and 3-body system tests is in properly setting the PTO damping level. The scheme for choosing the PTO damping value, for a given wave frequency, is based on the particular dynamics of the system. Thus, to ensure a fair comparison, the PTO must be properly set for each of the 2-body and 3-body systems. In this chapter, a brief review of the strategy for tuning, or controlling, a point absorber WEC is presented with a focus on the *master-slave* relationship between the VIS mechanism and the PTO; the VIS system provides a change to the system dynamics (called geometric control) that is the *master* phase, and the PTO damping is adjusted to follow in the *slave* phase. In order to avoid computationally expensive optimization, an analytical solution is sought for each device's tunable parameters. For the 3-body system these parameters are the effective mass of the VIS system and the PTO damping.

4.1 Mechanical Impedance and WECs

As described in a series of works by Bubbar [25], [31], [77], the heaving dynamics of a point absorber WEC in a simplified ocean wave environment can be described using mass, stiffness and damping coefficients. This approach is valid when wave heights are small, when the degrees of freedom of the converter are limited to heave only, and when the waves are regular. In this situation, the system dynamics can be represented using a mechanical circuit

which is analogous to an alternating current circuit where force (F) is the current alternating with a frequency (ω). The voltage at a point in the circuit is analogous to velocity.

Each body in the WEC has an impedance comprised of by mass, damping and stiffness contributions, and each of these contributions has itself several components. As an example, the mass of the spar is composed of true mass plus added mass. Damping of the spar is formed from drag and radiation. Stiffness has its most significant contribution from the hydrostatic force. These impedances (Z) are mapped as components in a circuit and have both real and imaginary parts. The form of the impedance for different types of mechanical elements is shown in Figure 33 which has been reproduced from [25]. In Figure 33, \hat{u} is velocity, stiffness is given by k , and damping is represented by B and $i = \sqrt{-1}$. The subscripts are representative of nodes in the physical system, or bodies, that are on either side of the physical element and possess a velocity amplitude \hat{u}_i . These components are arranged in series or parallel based on the configuration of the bodies in the point absorber system. A single body's parameters are modelled in parallel while each body and its connection is modelled in series. The excitation force is the driving force behind the circuit driving the oscillation current source.

Mechanical circuit elements.

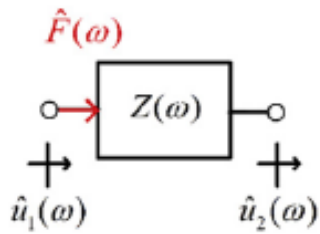
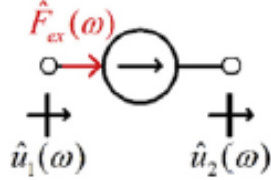
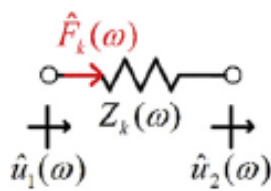
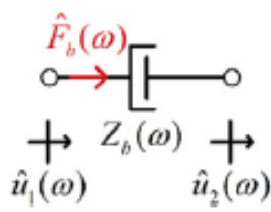
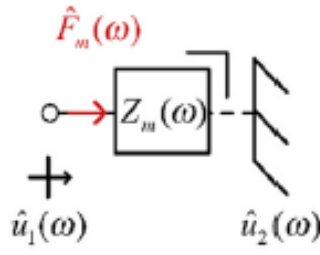
Element Description: Circuit Element	Constitutive Equation
<p>Generic Mechanical Impedance</p> 	$Z(\omega) = \frac{\widehat{F}(\omega)}{\widehat{u}_1(\omega) - \widehat{u}_2(\omega)}$
<p>External Force Source</p> 	$\widehat{F}_{ex}(\omega) = Z_{F_{ex}}(\omega)[\widehat{u}_1(\omega) - \widehat{u}_2(\omega)]$
<p>Ideal Mechanical Spring</p> 	$Z_k(\omega) = -\frac{ik}{\omega}$ $\widehat{F}_k(\omega) = Z_k(\omega)[\widehat{u}_1(\omega) - \widehat{u}_2(\omega)]$
<p>Ideal Mechanical Damper</p> 	$Z_b(\omega) = B$ $\widehat{F}_b(\omega) = Z_b(\omega)[\widehat{u}_1(\omega) - \widehat{u}_2(\omega)]$
<p>Ideal Mechanical Mass</p> 	$Z_m(\omega) = i\omega m$ $\widehat{F}_m(\omega) = Z_m(\omega)[\widehat{u}_1(\omega)]$

Figure 33: Mechanical Circuit Elements. Reproduced from [25]

Using these mechanical circuit elements, the simplified (e.g. regular waves and heave only motion) WEC body dynamics can be cast in a mechanical circuit [31]. Falnes exploited this concept and used Thevenin's theorem of simplifying circuits to derive governing equations on how to set the internal mechanics of the PTO in a SBPA. Falnes showed that (for simplified conditions and system dynamics) the PTO should be impedance-matched to the WEC [23]. Bubbar later showed that Falnes' derivations corresponded to the case of a 'canonical form' that

could be formed for any multi-body point absorber, such as a two-body or 3-body VISWEC systems studied in this work, by reduction of the mechanical circuit of the original WEC. The resulting simplified circuit contains impedance blocks that are functions of both wave frequency as well as the original WECs physical parameters, morphing the canonical form into different devices at each frequency but has the same simple structure as the circuit of an SBPA [25], [31]. That SBPA has a geometry, hydrodynamic and inertia properties that are ‘equivalent’ to the original WEC in terms of the system response to a regular wave at a given frequency. In the canonical form, the PTO impedance is in parallel to the original WEC’s transformed SBPA impedance. Thus to maximize power dissipation over the PTO, its impedance should be matched to the complex conjugate of the WEC impedance following the same simple principles recognized by Falnes in [23]. This technique has been referred to as impedance matching or ‘complex-conjugate PTO control’ [23], [77].

Using Bubbar’s approach, the different configurations of the VISWEC device, 3-body and 2-body, are shown in circuit form in Figure 36 through Figure 38. In these circuits, each body’s hydrodynamics, hydrostatics and inertia are characterized by a spring, damper and mass elements connected to ground, while the generalized PTO connecting the two bodies is characterized by a spring and damper – the damper’s energy dissipation being the model of energy extraction. The specifics on the simplification of a mechanical system of both a 2-body and 3-body configuration can be found in Bubbar’s work [31].

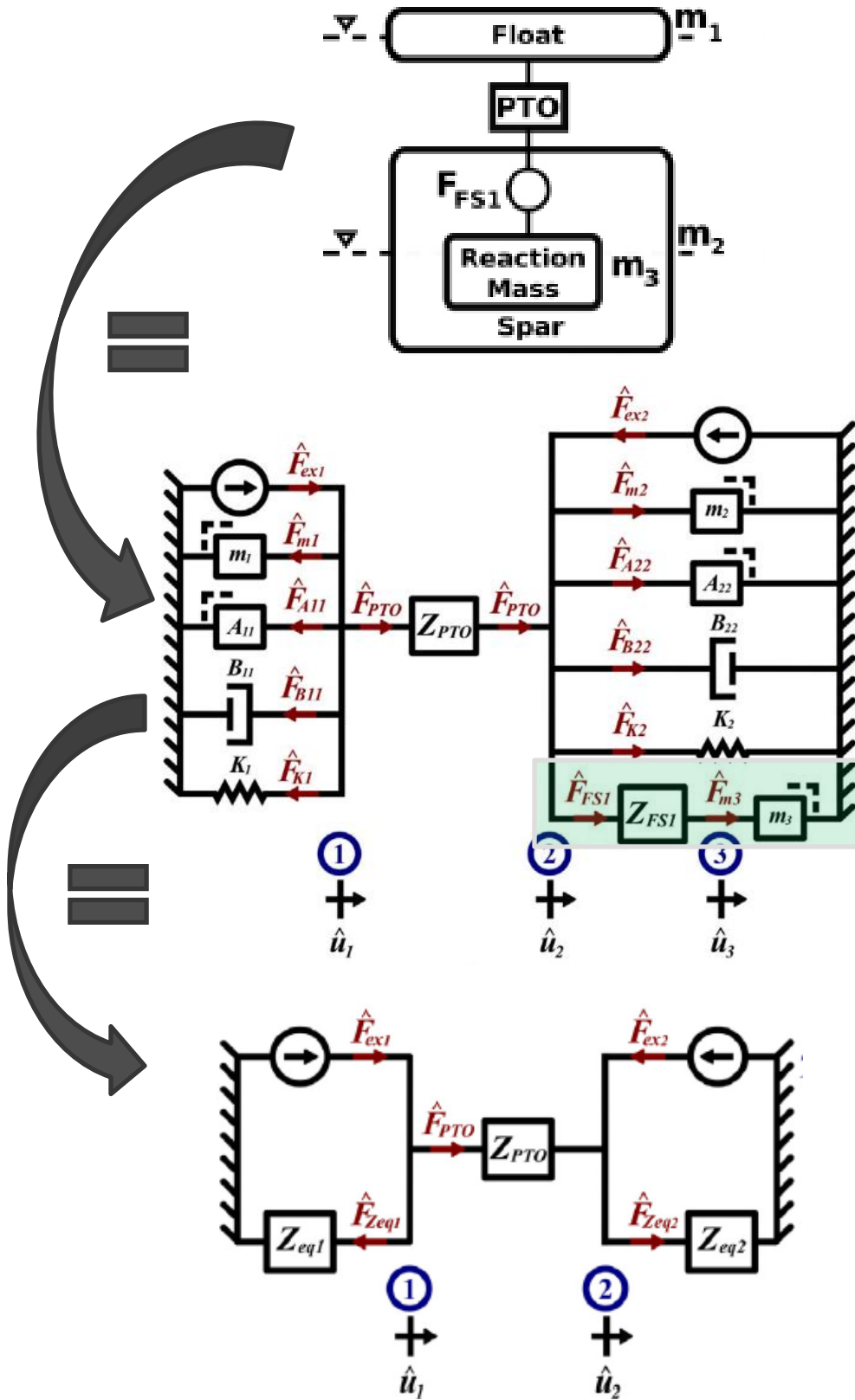


Figure 34: 3-Body SRPA Circuit Impedance reduced using Thevenin's theorem where body 1 is the Float and body 2 is the Spar [25]

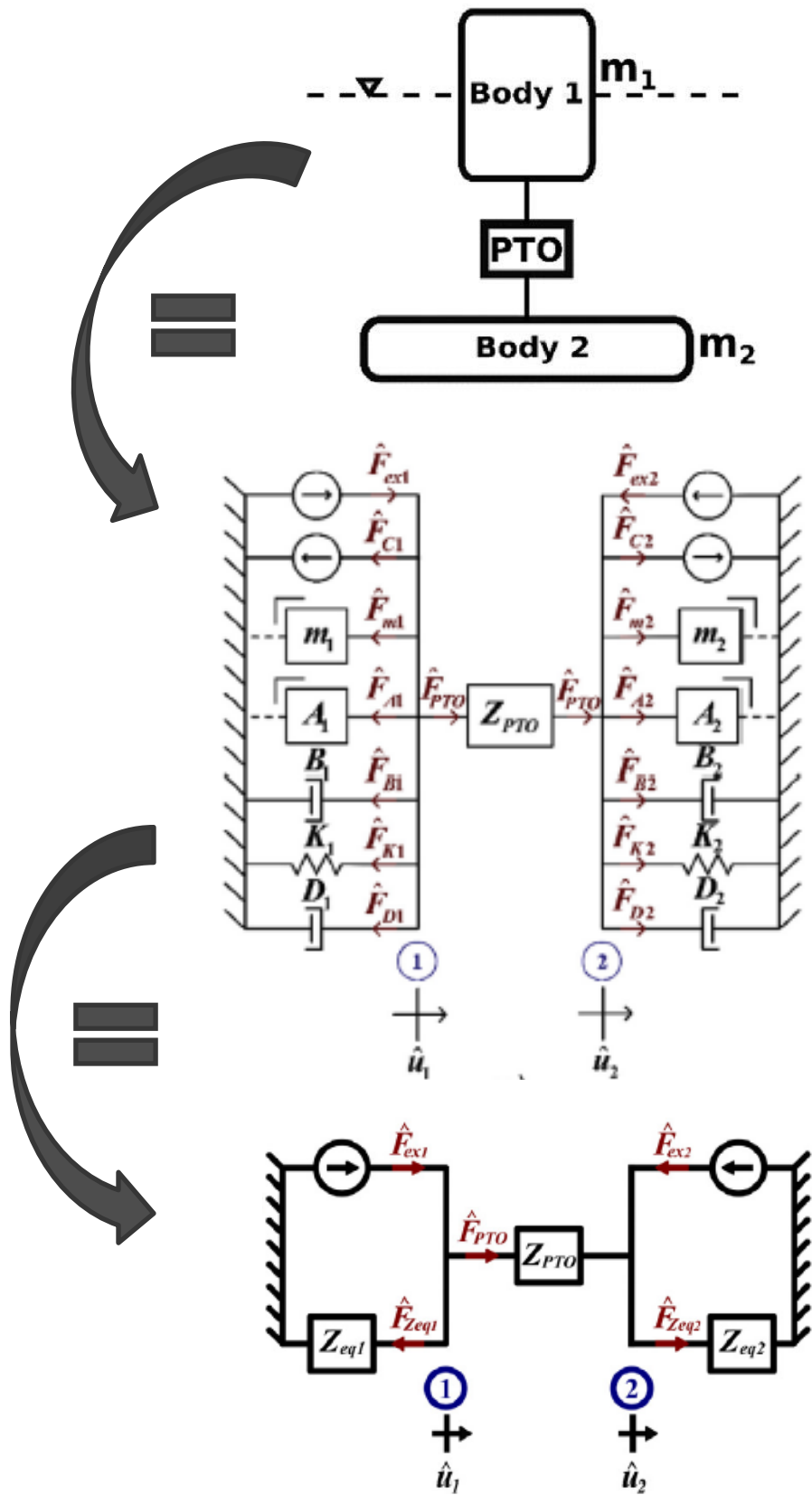


Figure 35: 2- body SRPA Circuit Impedance [25]

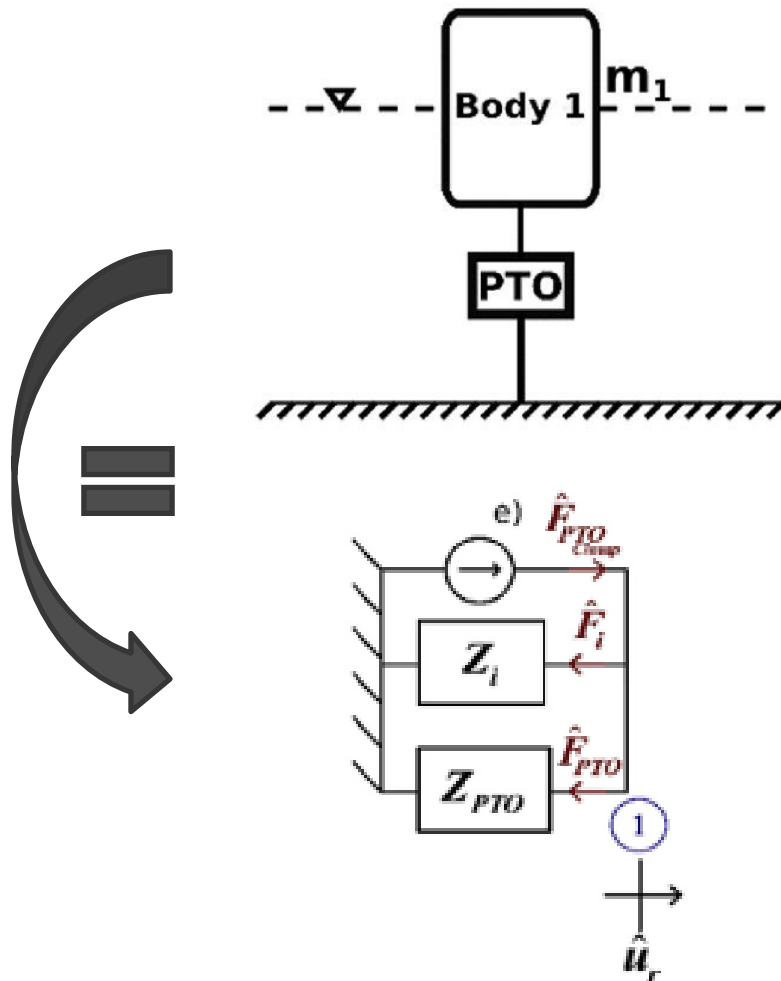


Figure 36: Single body point absorber circuit impedance [25]

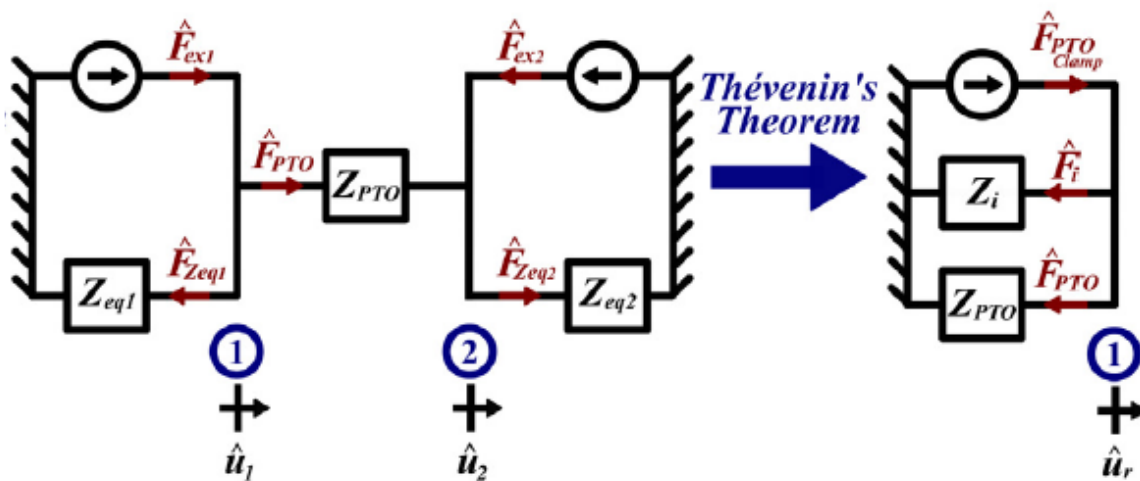


Figure 37: Conversion of a typical Thévenin's Theorem [25]

The VIS component of the 3-body VISWECs, shown in Figure 34, allows us to control the inertia of the ballscrew, moreover the impedance, of one of the bodies, highlighted in green. While this adds complexity to the system there is only one optimal setting at each frequency for the 3rd body meaning it still acts like 2-body system albeit a different 2-body system at each frequency. In this context, ‘different’ means that the spar has effectively changed geometry, or physical impedance, between adjustments of the VIS system. Each of these systems can be simplified to a single body using Thévenin’s theorem displayed in Figure 37. Having sequentially reduced the 3-body system down to a single body SBPA, or canonical form, the PTO of the 2-body system can be impedance matched with the incident regular wave.

4.2 Impedance Matching

The PTO Impedance is quantified with complex numbers with the real component being equal to the damping value of the PTO and the imaginary component being realized through some combination of spring stiffness and inertia, or reactance. The principle of impedance matching takes the complex conjugate of the equivalent impedance of the system, the difficulty being the determination of the equivalent system. Bubbar extended Falnes’ work to include the detailed simplification of a 2-body and 3-body system with the extension of the total impedance equation as will be presented in the following subsections.

4.2.1 Single Body Impedance Matching

In Bubbar’s notation, the impedance of a single floating body is comprised of three major contributors; a dampening term (constants B and D), an inertial term ($i\omega$) and a spring or stiffness term ($\frac{-i}{\omega}$) as shown in eq. (4.1), the indices i refers to the body number.

$$Z_i(\omega) = (B_i(\omega) + D_i(\omega)) + i \left(\omega[M_i + A_i(\omega)] - \frac{c_i}{\omega} \right) \quad (4.1)$$

where B is the added dampening coefficient, D the drag coefficient, c is the buoyancy stiffness, M the mass and A the added mass of the single body. The optimal PTO damping value is set by taking the complex conjugate of the total impedance of the SBPA, the complex conjugate of a complex number has an equal real part and equal imaginary part but the imaginary part has the opposite sign.

The reactance correlates to a spring stiffness within the PTO that when multiplied with the original complex number will eliminate the imaginary part. Since this work will only consider

the damping value of the complex conjugate, the optimal PTO term can be calculated as the absolute value of the total impedance, known as amplitude control.

$$Z_{PTO} = |Z_i| \quad (4.2)$$

4.2.2 Two-body SRPA Impedance Matching

The total impedance of an SRPA is shown in eq. (4.3) as impedances of each body Z_1 and Z_2 .

$$Z_{eq}(\omega) = \frac{Z_1(\omega)Z_2(\omega)}{Z_1(\omega) + Z_2(\omega)} \quad (4.3)$$

Z_1 and Z_2 are the complex impedances of the Float and Spar respectively, and each body's impedance is calculated the same as eq. (4.1) but with values specific to the Float and Spar geometries. This total impedance is the single body equivalent of a 2-body system and the PTO value can be calculated similarly as:

$$Z_{PTO}(\omega) = |Z_{eq}(\omega)| \quad (4.4)$$

4.2.3 Three-body SRPA Impedance Matching

While a purely resistive control scheme, such as the one considered in this work, only affects the magnitude of the response, the 3-body system controls the phase of the response. A reactive PTO uses spring and dampening forces to control both the phase and amplitude of response thus contaminating the analysis of the 3-body system. Since the VIS parameters, particularly the rotational inertia of the ballscrew, flow through into the Z_2 term of eq. (4.4), the VIS physical parameters must first be determined prior to the PTO impedance calculation.

The goal of a 3-body VISWEC system is to have the inertia of the VIS set so that the imaginary component of Z_{eq} in eq. (4.3) is driven as close to zero as possible so that the application of eq. (4.4) is as close to the ideal 'impedance matching' strategy as possible. The algebraic and complex expressions for Z_1 , Z_2 and Z_{eq} make it very difficult to reveal what the value of that inertia should be at each frequency through analytical manipulation. As mentioned before the third body tunes the second body to react at an optimal phase, this optimal setting achieves the same goal as the reactive setting of the PTO.

The impedance contributions of the *effective mass* of the VIS system to the overall system impedance is calculated using M_{eff} as the function of the Reaction Mass ($M_{eff} = M_{RM}JL$), where M_{RM} is the mass of the Reaction Mass, J is the rotational inertia of the ballscrew and

variable inertial mass and L is the lead of the ballscrew. B_{Meff} is the linearized damping of the VIS, quantifying the friction in the linear guides and ball screw as characterized in Section 3.3.3 Variable Inertial System, and k the spring stiffness force between the Spar and Reaction Mass. The impedance of the VIZ is calculated as

$$Z_{Meff}(\omega) = i\omega M_{eff} + B_{Meff}(\omega) - \frac{i}{\omega}k \quad (4.5)$$

Z_{Meff} represents the impedance contribution from the mass modulation scheme highlighted in green in Figure 34, within the second body, the Spar. It should also be noted that the mass value for the spar has changed to reflect the removal of the reaction system, values shown in Section 3.3, and is accounted for with the addition of the mass term (Z_{Meff}), in eq. (4.6), the equivalent system impedance.

$$Z_{eq}(\omega) = \frac{Z_1(\omega) (Z_2(\omega) + Z_{Meff}(\omega))}{Z_1(\omega) + Z_2(\omega) + Z_{Meff}(\omega)} \quad (4.6)$$

This total equivalent impedance follows logic as the second body equivalent is the addition of the original spar geometry, minus the mass of the *effective mass*, plus the impedance of the VIS, altering the impedance of the second body. To search for optimal values of the effective mass a numerically exhaustive search is required, given in Section 4.5.

4.3 Assumptions

The theory of mechanical impedance and impedance matching assumes that the system contributions are all linear meaning small amplitudes of body motions. It also assumes that there are no significant impedances resulting from hydrodynamic interactions between the float and spar. In this work, the WAMIT hydrodynamic coefficients provide frequency based hydrodynamic coefficients for all characteristics needed in this calculation. There is one damping value the WAMIT can tell us nothing about, drag, frequency based drag contribution will need to be included These calculations are applied to a single DoF, the heave DoF.

Table 9: Parameters for use in impedance calculation based on actual 1/25th physical model

Body	Parameter		Symbol	Impedance	Origination	Strategy
Float	Mass	Physical Mass	M_1	$i\omega M_1$	Physical	Pulled from physical model
		Added Mass	A_1	$i\omega A_1 * \rho$	WAMIT	Linear Coefficient calculated within WAMIT
	Stiffness	Buoyant Stiffness	C_1	$(-i/\omega)C_1$	Physical	(Waterplane area)(density of water)(gravity)
	Damping	Added Damping	B_1	$B_1 * \rho \omega$	WAMIT	Linear Coefficient calculated within WAMIT
		Drag	D_1	D_1	Linearized	Linearized calculation based on water velocity
Spar	Mass	Physical Mass	M_2	$i\omega M_2$	Physical	Pulled from physical model
		Added Mass	A_2	$i\omega A_2 * \rho$	WAMIT	Linear Coefficient calculated within WAMIT
	Stiffness	Buoyant Stiffness	C_2	$(-i/\omega)C_2$	Physical	(Waterplane area)(density of water)(gravity)
	Damping	Added Damping	B_2	$B_2 * \rho \omega$	WAMIT	Linear Coefficient calculated within WAMIT
		Drag	D_2	D_2	Linearized	Linearized calculation based on water velocity
VIS	Mass	Physical Mass	M_{eff}	$i\omega M_{eff}$	Physical	Pulled from physical model
	Stiffness	Spring Stiffness	k	$(-i/\omega)k$	Physical	Pulled from physical model
	Damping	Friction	B_{eff}	B_{eff}	Linearized	Experimentally Matched Linear Approximation

The assumptions made in some of the parameters in the above table lead to errors in the impedance calculation. The stiffness parameter is linearized by taking the waterplane area for a buoyant stiffness coefficient and multiplied by the density of the water and acceleration due to gravity. This is not the actual buoyancy stiffness but matches closely for bodies with vertical sides at the waterline. The linear representation for the float will result in less error than the Spar.

The stiffness of the VIS is taken from the stiffness of the springs connecting the Reaction Mass and Spar, the representation is linearized and the physical spring are close to linear within the limits they are being used, there is some deviation but nothing significant. The friction in the VIS is a linearized approximation as previously shown which is a close approximation but can deviate if there is any coulombic friction.

Physical mass is taken from the physical model and is set firmly, only source of error could be miss-measuring, although the added mass element, stemming from the hydrodynamics, is calculated within WAMIT using linear wave theory which can only be as accurate as the linear approximation with limitations noted in Chapter 2. The term that WAMIT outputs is normalized and needs to be multiplied by the density of water. The limitations of the added mass coefficient pertains to the added damping value as well but needs to be multiplied by frequency as well as the density of water.

The other component of the total damping value, drag, has yet to be account for within the impedance calculation. Drag is implemented as quadratic drag, since impedance is a linear

approximation there needs to be a method to implement a linearized drag that can closely approximate the quadratic drag implemented within ProteusDS.

4.4 PTO Damping Calculation for the 2-body System

Without the consideration of drag in the total impedance, the analytical solution for optimal PTO will greatly overestimate the amplitude of motion of each body, likely leading to erroneously large PTO resistance (damping) values. This overestimation will result in an over prediction of the required PTO impedance, and subsequently the two bodies (Spar and Float) will be almost rigidly connected leading to a vast reduction in power production. In order to incorporate drag into the impedance, a method was needed to linearize the drag force, preferably without prior knowledge derived from simulation studies.

4.4.1 Drag Linearization & PTO Impedance Calculation

Clauss outlined a method to quantify drag on a stationary vertical cylinder based on the particle velocity associated with linear wave theory and known quadratic drag coefficients for a cylindrical shape [78]. The technique presented by Clauss was applied to a cylinder in the surge degree of freedom for floating spar piling structures in a seaway. The technique is applied to the heaving degree of freedom in this work because the amplitudes of rotation of the waves compared to the size of the structure is roughly similar to that in surge. Clauss' equation for the linearized drag coefficient can be seen in eq. (4.7) where D_l is the coefficient for linearized drag, D_q is the quadratic drag coefficient and $u_a(\omega)$ is the amplitude of the oscillating velocity as shown in eq. (4.8)

$$D_l(\omega) = \frac{8}{3\pi} D_q u_a(\omega) \quad (4.7)$$

$$u_a(\omega) = h\omega e^{\kappa z} \cos \omega t \quad (4.8)$$

The peak velocity in the heaving direction ($u_a(\omega)$) is a function of the wave height (h) the wave frequency (ω), the depth location (z) and the wave number (κ). The location chosen for water velocity is the maximum velocity where $z = 0$ this drives the term $e^{\kappa z}$ to 1 leaving the peak velocity a function of waveheight and frequency. A wave height of 0.11 m was chosen as this is the predominant wave height in the environmental conditions described later in Chapter 5.

Additionally, the linearized drag coefficient must be scaled by the area it is applied over and by the density of the fluid. This calculation is shown in eq. (4.9). The subscript i is for the indices for the first (float) or second (spar) body.

$$D_i = D_l \frac{\rho}{2} A_0 \quad (4.9)$$

Clauss noted that the actual peak velocity experienced also depends on the body's velocity [78]. Clauss considered three different methods to evaluate the peak velocity. First, the water particle velocity is used on its own; second, the body velocity is used on its own; third, the relative velocity between the body and the water particles is applied.

While water velocity can be calculated with linear wave theory and accomplishable without knowledge of the bodies present, the body velocity and relative velocity are calculated by running simulations with the PTO value set to zero and evaluating the velocities of the bodies and their relative movement to the water. Observing the resulting body motion, the drag coefficient can be linearized in each of these three ways.

Running the simulation to determine body velocity at each frequency is an expensive requirement but it was still considered in order to test if the addition of the body velocity would provide a closer approximation. The Drag coefficients determined with eq. (4.9) under each velocity consideration are presented in Figure 38.

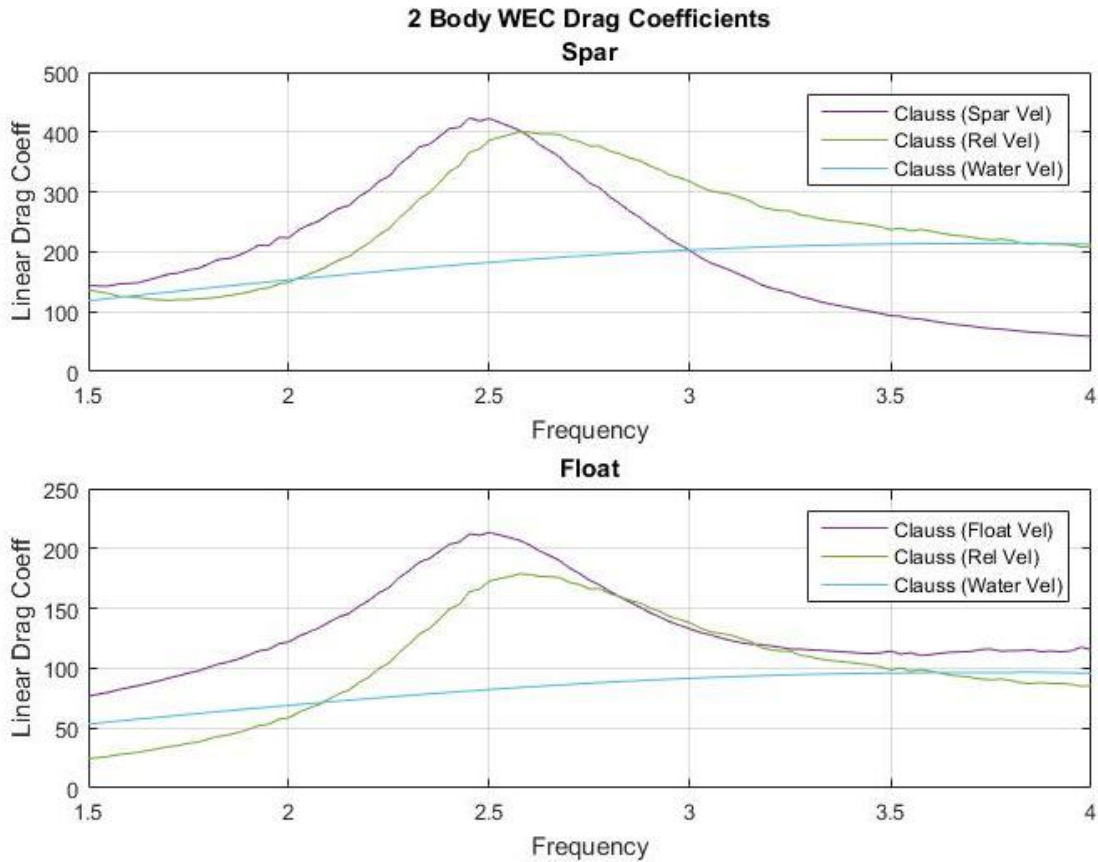


Figure 38: Linearized drag coefficients of each body determined by three different velocities over a span of frequencies

To complete the calculation of the PTO damping, each of the three different estimates of the linear drag coefficient shown in Figure 38 were inserted into the calculations of the equivalent impedance, Z_{eq} , for the two body system. The resulting schedules for the PTO damping are shown in Figure 39.

The 2-body PTO damping value with no drag consideration can be seen to be significantly larger than each of the others peaking at a single frequency (~ 2.6 rad/s) but all PTO values with consideration of drag seem to mostly converge outside of this frequency (2.2 – 3.0 rad/s). This comparison is useful as it shows how the PTO value can be overestimated if drag is not considered. PTO value is increasing likely due to increasing tendency for relative motion (some form of resonant mode of vibration of the 2-body system), this range of frequencies is considered the ‘systems natural frequency’.

The results of Figure 39 raises the question how close are the PTO values with each drag consideration near the systems natural frequency, as they diverge in this area. The way to

determine which drag linearization is more applicable is to complete an exhaustive numerical search for the optimal PTO value using the numerical simulation with the model described in Chapter 3.

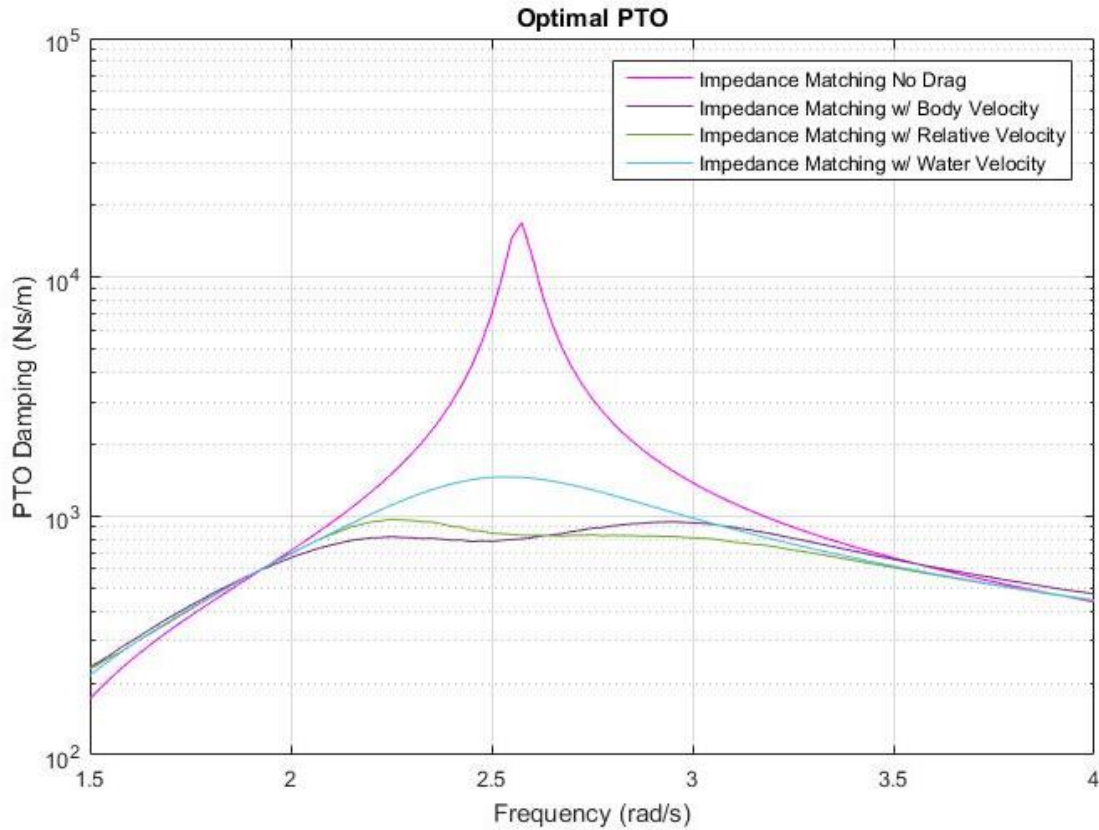


Figure 39: PTO values from different considerations for a drag term within the analytical solution for optimal PTO

4.4.2 Direct PTO Optimization

A brute force optimization of the PTO value over 51 frequencies between 1.5 and 4 rad/s was completed in the heaving direction only using the numerical simulation of the 2-body VISWEC system. For this optimization, the same wave height of 0.11m was applied as in the drag linearization calculations. The simulation was kinematically constrained to only heaving motion and all other hydrodynamic effects described in Chapter 3 were considered. Fifty evenly spaced PTO damping values between 0 to 16,000 Ns/m were tested.

The second round of brute force optimization took a range from one value below the rough optimization maximum to one value above and considered 50 values between them. The results

were plotted on the same graph as Figure 39 and are displayed in Figure 40. The dots indicate the optimal PTO value determined through the optimization.

From these results it can be seen that Clauss's original quantification of linearized drag using water velocity was the best overall fit. While this may not hold true for all types of devices it can be stated that it is the best choice for a 2-body SRPA WEC because it follows the optimization the closest.

From this point moving forward the drag coefficient using linearized drag with water velocity is used as it is the closest approximation and only uses the velocity of the wave determinable without previous knowledge of the system dynamics. Since the hull geometry of the Spar and Float does not change between the 2 and 3-body cases, the drag values in Figure 38 can be used to determine the PTO damping value of the 3-body system.

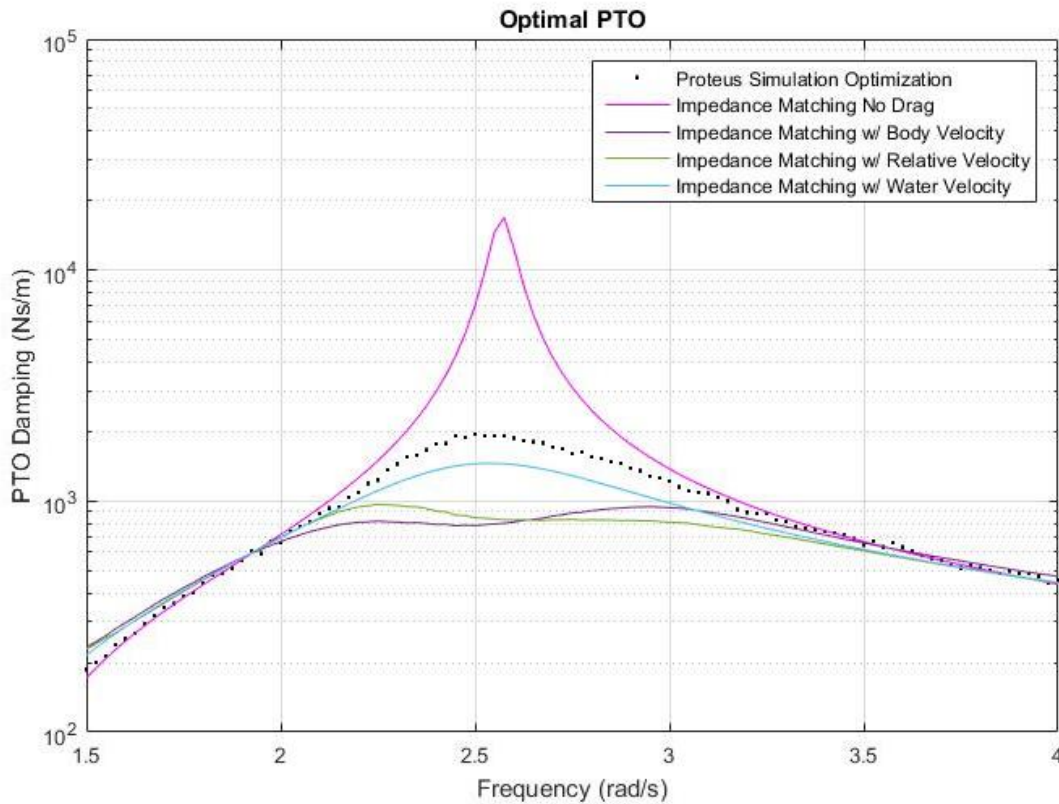


Figure 40: PTO values from different considerations for a drag term within the analytical solution for optimal PTO

4.4.3 Power Sensitivity to PTO Damping

While the previous section established that the drag linearization based on only the water particle velocity leads to a predicted PTO damping level that best matches the optimal PTO damping, it is still unclear how sensitive the power conversion performance is to the PTO damping values. To determine this sensitivity, power was calculated using the method described in Section 5.2.2 for all the simulations run in the second round of PTO value brute force optimization.

Figure 41 shows the optimal PTO damping and the PTO damping level as predicted using the linearized drag. The color scale on the plot, shown in legend as a black dot, indicates the power production at any damping-frequency point on the graph. The power is seen to not be critically sensitive to power production. It is seen that the linearized drag term is an adequate choice, although at frequencies close to the natural frequency of the system the value falls short which will allow more motion between the two bodies leaving unutilized power in the system, it still shows similar power productions across these frequencies. This means that the metric, or a way to measure, by which the systems will be evaluated will continue to be a valid metric for comparison.

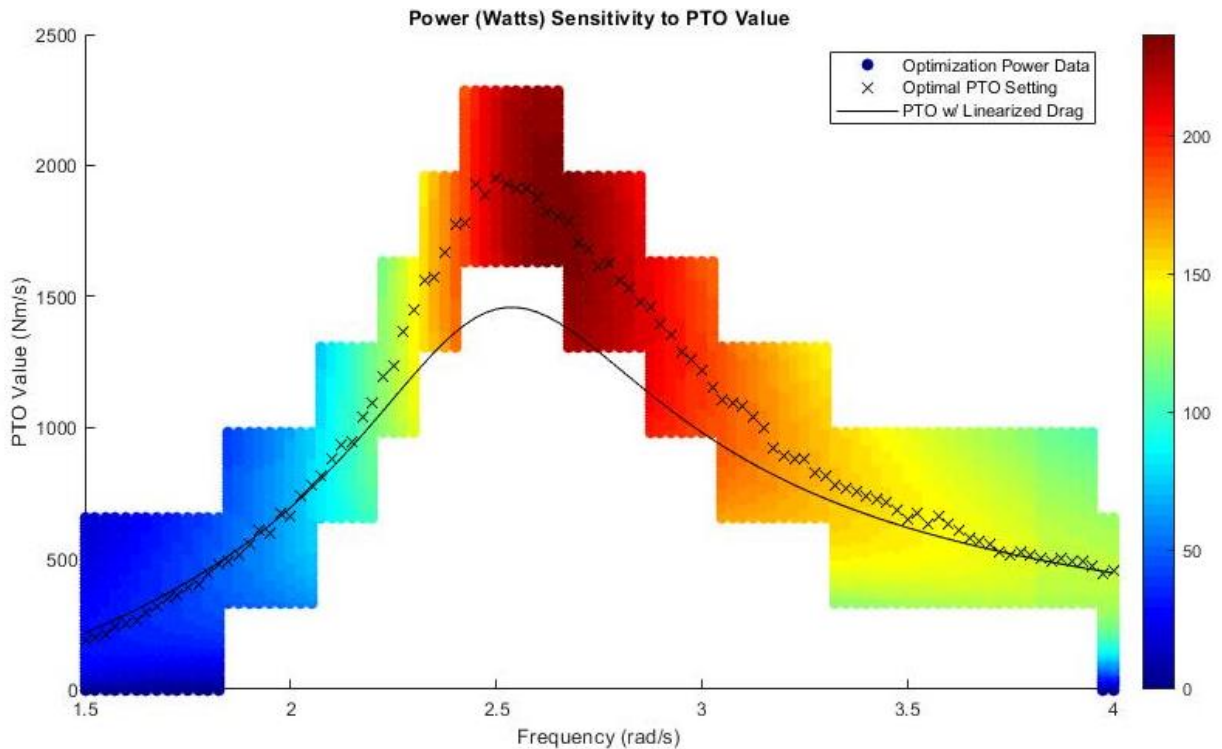


Figure 41: Power sensitivity (color) to PTO value with refined optimal PTO (x) and the chosen PTO value from consideration of linearized drag using water velocity (-)

4.5 PTO Damping Calculation for the 3-body System

Using the method described in Section 4.2 with the contributions from Section 4.4, optimal settings for each configuration are obtainable. Section 4.4 illustrated how a PTO damping value was calculated for each frequency of wave for the 2-body VISWEC system. In the 3-body case, the equivalent spar impedance has an additional contribution from the VIS component and the value of the effective mass, M_{eff} , has significant influence on the spar impedance. As a result, M_{eff} has significant influence on the overall canonical form impedance and thus the PTO damping level.

To determine the optimal setting of the impedance of the VIS, Z_{Meff} , a power calculation is required using the impedance mapping method described in Section 4.2. Bubbar outlined an equation to calculate power using excitation values (F) determined through WAMIT [25]. The equation is presenting in eq. (4.10) shows the excitation through the PTO where F_1 and Z_1 is the frequency dependent excitation and impedance of the Float and F_2 and Z_2 that of the Spar. The frequency dependent power is calculated with eq. (4.11), described more in Bubbar's work [25], where the impedance of the PTO, Z_{PTO} , is calculated by eq. (4.2).

$$F_0(\omega) = \frac{F_1(\omega) \left(Z_2(\omega) + Z_{Meff}(\omega) \right) - F_2(\omega) Z_1(\omega)}{Z_{eq}(\omega)} \quad (4.10)$$

$$P(\omega) = \frac{|F_0(\omega)|}{8Z_{PTO}(\omega)} \quad (4.11)$$

Figure 42, shows the optimal inertial settings within the limits of the VIS (0.027 – 0.007 kgm²), set by the limits of the scale physical model. The inertial setting is presented as this is the frequency dependent value that will be implemented in the simulated model. These values were calculated using a global optimization routine (particle swarm within MATLAB) that optimized maximum power production using eq. (4.11) as the objective function with the single input of VIS inertia. As the PTO value is determined by the systems total impedance the only input value is the rotational inertia.

Figure 43, shows the correlating PTO damping setting for the 3-body system using rotational inertia to determine Z_{Meff} and drag values determined in the previous section. Additionally, the 2-body PTO damping value is presented for easy comparison, it should be noted that the two PTO damping values are equal at approximately 2.5 rad/s.

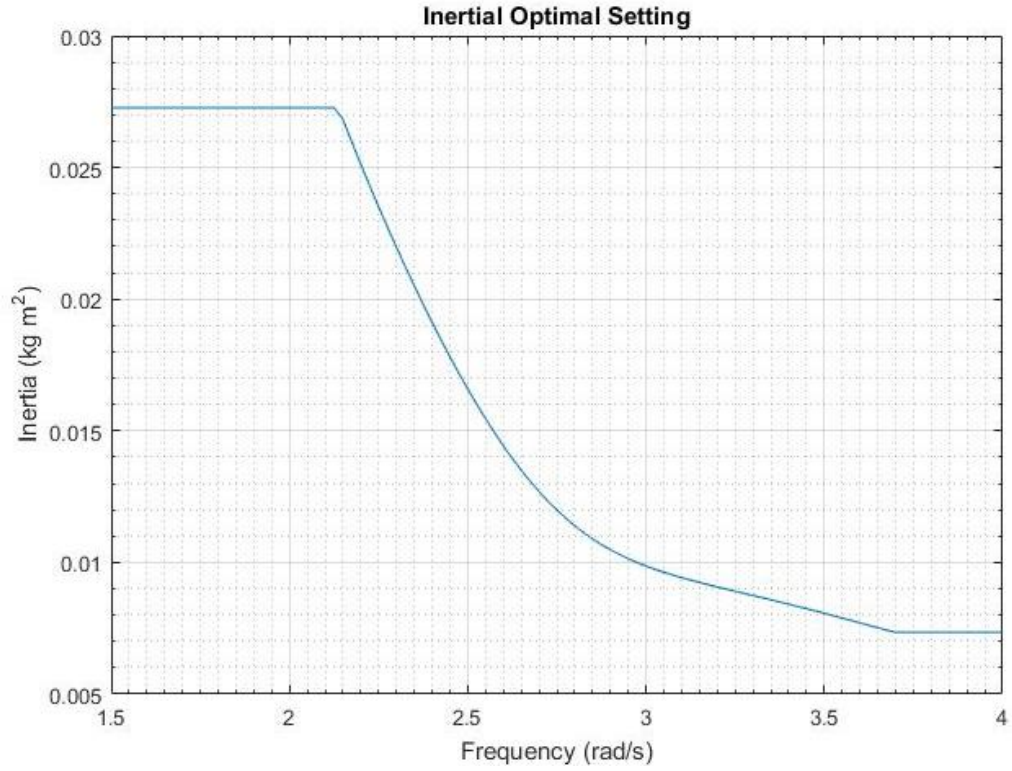


Figure 42: Optimal inertial setting for geometric control configuration

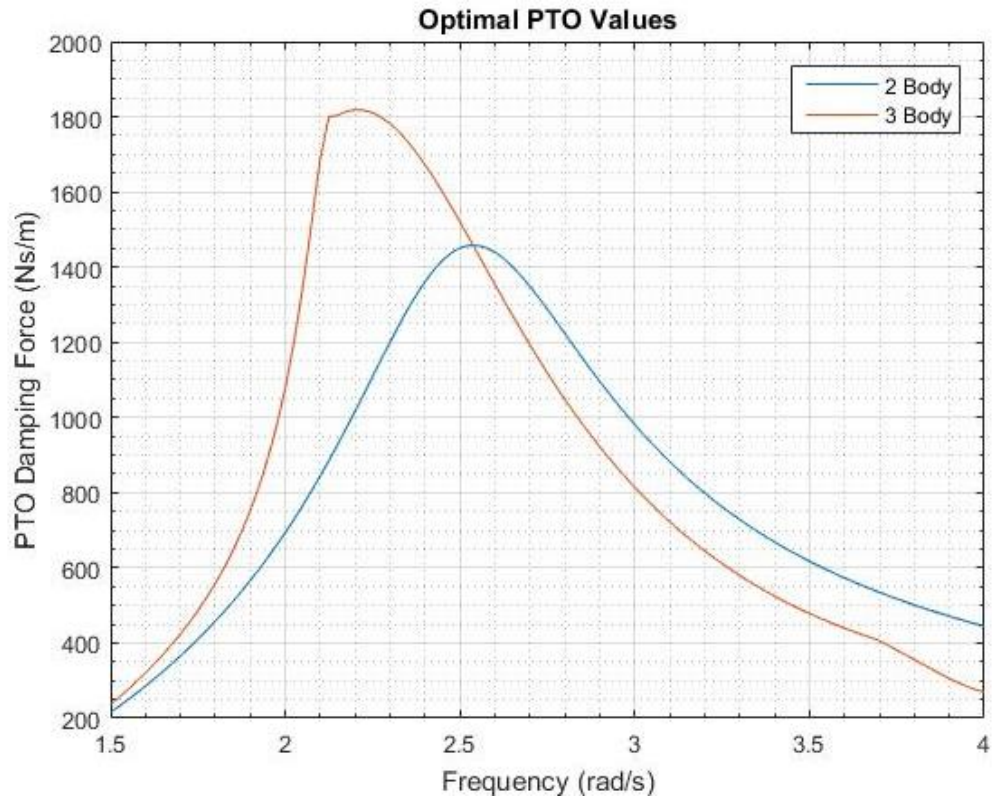


Figure 43: Optimal PTO values for both configurations

Chapter 5 Testing Conditions and Results

In this chapter, the results of the investigation of the simulation based investigation of the VISWEC performance are presented, with consideration on both the parametric excitation of rolling motion and power conversion performance. This investigation is completed for a wide range of environmental parameters, and these parameters including the regular wave heights and periods, are established prior to the presentation of the results. Additionally, a series of different kinematic (i.e. motion) constraints are applied on the VISWEC device which is configured to act as a 2-body or 3-body by locking down or allowing the VIS to move. These constraints are used to increment the complexity of the testing and help identify how performance changes are associated with particular DoFs of the system.

The first section of this chapter outlines the range of environmental parameters and how they were chosen based on full scale data for wave conditions off Vancouver Island. The second section will outline the kinematic constraint scenarios applied to the system in order to isolate certain degrees of freedom. For each successive stage of testing, additional DoF are added until the full 6-DoF motion of the VISWEC device is considered. The remainder of the chapter will compare the simulation results for the 2-body and 3-body systems in each scenario and comment on the findings.

5.1 Wave Parameters

Previous studies at UVic on point absorber dynamics and performance have been subject to limits on the wave parameters considered. The UVic research group's focus is the coastal zone off Vancouver Island (it is an energetic wave resource that can provide a fertile testing ground for full scale WECs), and so conditions prevalent in this region are the primary focus. In

addition, UVic based point absorber research to date has been executed through experimental testing of physical scale models, and so the limits of the wave generators at the test tank further constrain the testing conditions. As an example, in the work of Beatty et. al., the wave testing tank imposed frequency limits of 1.5-4.0 rad/s and wave heights of 0.01 – 0.05 meters [73]. The corresponding full scale limits equate to frequency limits of 0.3 – 0.8 rad/s, period of 7.85 – 20.94 seconds, and wave height limits of 0.25 – 1.25 meters covering only a small portion of full scale measured ranges. A wider range of wave parameters were considered in Bailey et. al. where the wave field was used to calculate power production off the coast of Vancouver Island, more specifically Amphitrite Bank [63].

To aid in the characterization of the wave climate off the west coast of Vancouver Island, wave measurement buoys have previously been deployed at strategic locations. Robertson et al. [17] and Hiles et al. [79] used these measurements to verify coastal wave model predictions of the near shore wave field, and subsequently characterized the wave field with a histogram based on combinations of significant wave heights and energy periods. Both authors found that the majority of occurrences occurred between energy periods of 8-11 seconds and significant wave heights of 1-5 meters. These statistical descriptions of wave period and height are extracted from measured or calculated (if using a coastal model) irregular wave spectra which are decomposed into a collection of regular waves with random individual phases. The significant wave height and energy period histogram of Amphitrite Bank is presented in Figure 44 taken from Robertson et al. [17]. The total hours of occurrence in a year are displayed in each bin and the percentage of total annual power delivered presented using the color scale in each bin. These values are full scale calculations from measurements of the real-world environment. To be applied in this work, the wave heights and periods need to be scaled to match the scale of the VISWEC device being studied.

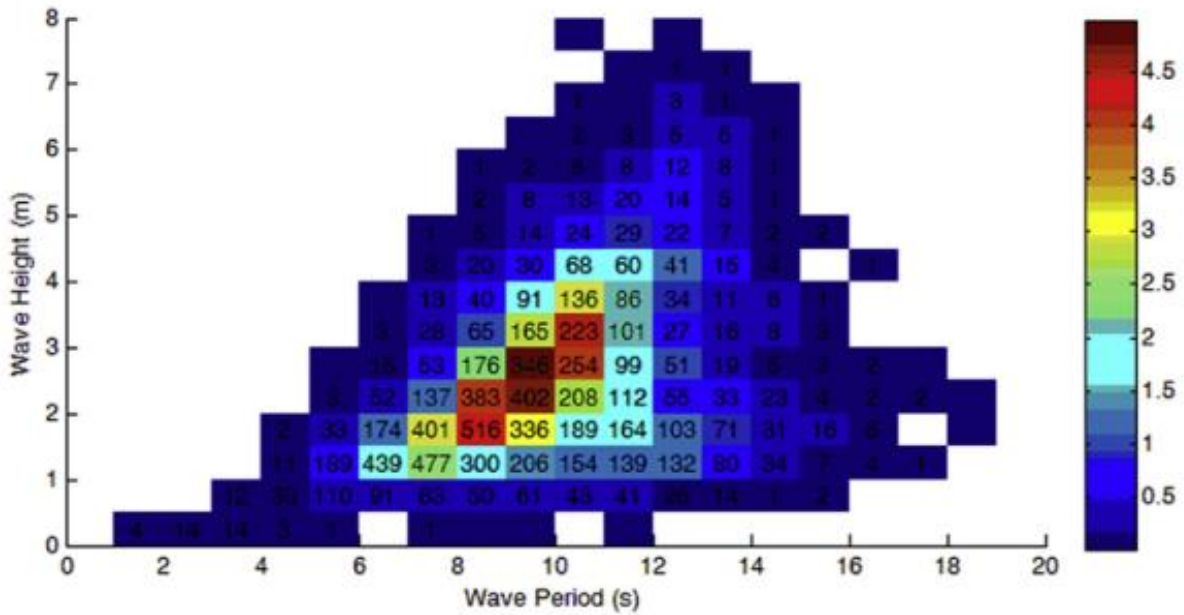


Figure 44: Histogram of significant wave height and period at Amphitrite Bank off the west coast of Vancouver Island [17]

The two main scaling techniques used to preserve system dynamics in a viscous environment are Froude and Reynolds scaling. Generally Froude scaling is used when the gravitational forces are dominant in the system with viscosity having a lesser impact. Reynolds scaling is used when viscous forces dominate while gravitational forces are less significant. Since the system in this work is dominated by gravitational and inertial forces, Froude scaling is the better option but it is still difficult to ideally scale every physical effect in the system (e.g. mooring lines). The table below outlines how each dynamic quantity is ideally scaled, where Λ equals the geometric scaling factor, which is $1/25$ in this work. The variables L , T and M are the length, time and mass indicators, respectively.

Table 10: Froude Model Scaling

Scale Ratios for Froude Scale			
Parameter	Dimesion	Froude Scale	Model 1:25
Geometric			
Length	L	Λ	1/25
Area	L^2	Λ^2	1/625
Volume	L^3	Λ^3	1/15,625
Rotation	-	1	1
Kinematic			
Time	T	$\Lambda^{1/2}$	1/5
Velocity	LT^{-1}	$\Lambda^{1/2}$	1/5
Acceleration	LT^{-2}	1	1
Dynamic			
Mass	M	Λ^3	1/15,625
Force	MLT^{-2}	Λ^3	1/15,625
Pressure	$ML^{-1}T^{-2}$	Λ	1/25
Energy	ML^2L^{-2}	Λ^4	1/390,625
Power	ML^2T^{-3}	$\Lambda^{7/2}$	1/78,125

The scaling of the wave environment is mandatory since the VISWEC device being studied is already at 1:25 scale. While no full scale device yet exists, the scale factor can be set based on the expected draft of the system at full scale (approximately 32.5 meter at full scale, 1.3 meters at scale). While the current work is to be completed through numerical simulation, wave tank limits constrain the range of wave frequencies allowed in experimental testing. If this work is to be validated or compared with experimental physical scale model tests then the conditions considered here need to be repeatable in the wave tank. The range (1.5 – 4.0 rad/s) was used for simulation which covers 2x the roll natural frequency of approximately 2.6 rad/s which should be the response frequency of parametric excitation. Additionally this range of frequencies allows for a wide consideration to induce and investigate parametric excitation.

In terms of wave height limits, the minimum wave height testable within the wave testing tank is 0.01 meters which corresponds to a very conservative full scale wave height of 0.25 m. Since parametric excitation has been shown to be enhanced with wave height, the testing in this work needed to extend into larger wave heights than those limited by the testing tank.

The range of frequencies and wave heights chosen is shown in Table 11. Each parameter shows the range and incremental values used at scale as well as the correlating full scale

parameter determined using Table 10. The increments show that a total of 2020 regular waves (20 wave height and 101 frequencies) will be considered for each case. The histogram shown in Figure 44 is provided again in Figure 45 with a box outlining the full scale wave period and height range considered in this work. The extremes of this rectangular domain seen at the top and the far right are included for consideration of parametric excitation, while the portions of the test domain overlapping with the majority of occurrences in the histogram will provide insight into not only parametric excitation but also power production in regular waves comprising the wave climate off Vancouver Island.

Table 11: Environmental Model Settings

Model Settings						
Parameter	Used (1/25 th scale)			Full-scale		
	Min	Max	Inc.	Min	Max	Inc.
Frequency (rad/s)	1.50	4.00	0.025	0.30	0.80	0.005
Frequency (Hz)	0.24	0.64	0.004	0.05	0.13	0.001
Period (s)	1.57	4.19	0.026	7.85	20.94	0.131
Wave Height (m)	0.02	0.40	0.020	0.50	10.00	0.500

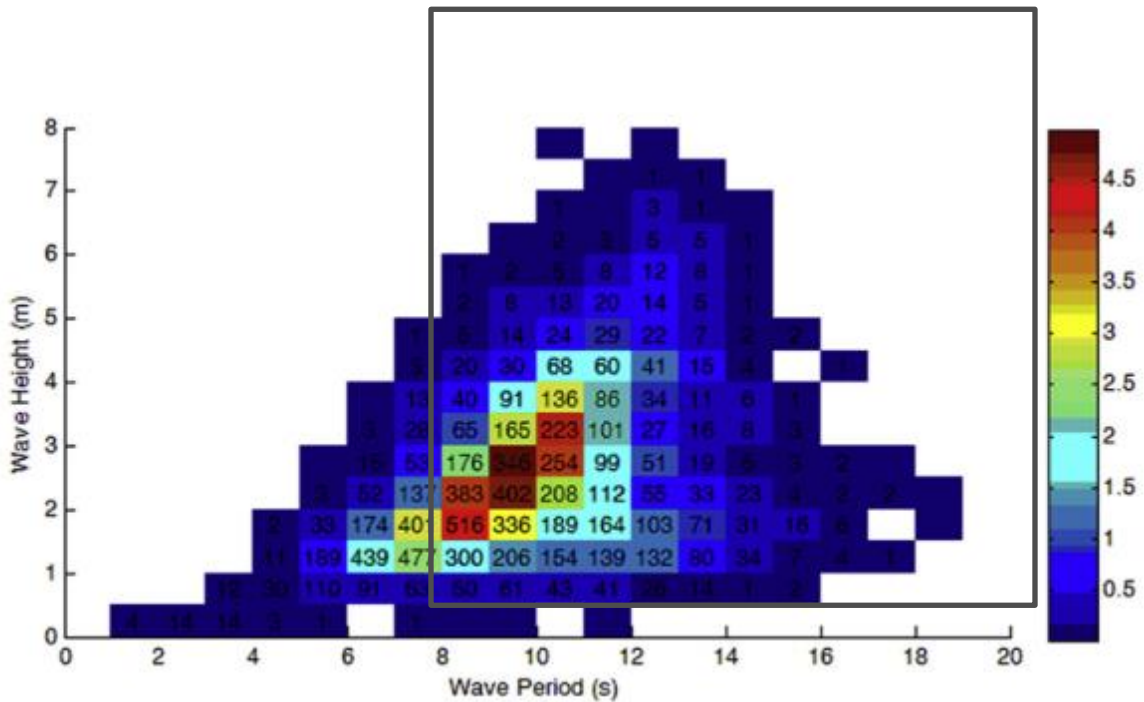


Figure 45: Histogram of significant wave height and period at Amphitrite Bank off the west coast of Vancouver Island [17] with the tested value range expressed as a box.

5.2 Kinematic Constraints and Performance Metrics

An incremental approach was used in testing the 2-body and 3-body versions of the VIZWEC. Kinematically constraining the systems allows for individual evaluation of DoFs, without effecting the dynamics of the system. Mooring lines can achieve the same goal of constraining the systems although as Ortiz showed, mooring lines can have a significant impact on system dynamics and power production [40]. Kinematic constraints will emulate what moorings could do to the system dynamics and provide insight into mooring design. Kinematic constraint scenarios are presented in incrementally decreasing pattern, gradually allowing more motion to each system shown in Table 12.

5.2.1 Kinematic Cases

- 1) A significant portion of research in point absorber dynamics has been subject to significant motion constraints, with heave constrained systems being very prevalent in existing literature. Thus the most constrained **Heave Only** case will be considered first to provide a baseline for comparison with following cases.
- 2) Parametric excitation has been shown in Chapter 2 to exist in the rolling DoF and hence the second case considered is constrained to **Heave and Roll** DoFs only. With no wave forces acting in the rolling direction of the WEC, any growth in rolling motion is indicative of parametric excitation.
- 3) The third case to be considered, '**Moored**', allows all DoFs except for surge and sway, holding the system on station while allowing for heave roll, pitch and yaw, achieving the goal of mooring without affecting the dynamics of the system.
- 4) Lastly all DoF are allowed in order to investigate the dynamics in every DoF and observe the **Free** system, this will be the first consideration of surge and sway.

Table 12: Kinematic Cases

Case	Free DoFs	Constrained Dofs
Heave Only	Heave	Roll, Pitch, Surge, Sway, Yaw
Have and Roll Only	Heave, Roll	Pitch, Surge, Sway, Yaw
Moored'	Heave Pitch, Roll, Yaw	Surge, Sway
Free	Heave, Roll, Pitch, Surge, Sway, Yaw	None

5.2.2 Performance Metrics

The first metric for comparison between the 2-body and 3-body systems is power production, power production is calculated through eq. (5.1) and eq. (5.2) where \dot{z}_{rel} is the relative velocity between the Float and Spar and Z_{PTO} is the dampening coefficient of the PTO calculated in Chapter 4. The power production calculation in Watts (joule/s) is performed for each tested condition. To eliminate transients in the data from the system reaching a steady state response, only the final 60 seconds of the simulation are used in the calculation. A time domain plot of system dynamics of the free 3-body system, the most complex system, with a wave height of 0.3 meters and a wave frequency of 2.5 rad/s is presented in Figure 46 as an example of how the system dynamics reach a steady state before the final 60 seconds.

$$P_{inst} = Z_{PTO}(\omega_e) \dot{z}_{rel}^2 \quad (5.1)$$

$$P_{avg} = \sum_{end-60(s)}^{end} P_{inst} / 60(s) \quad (5.2)$$

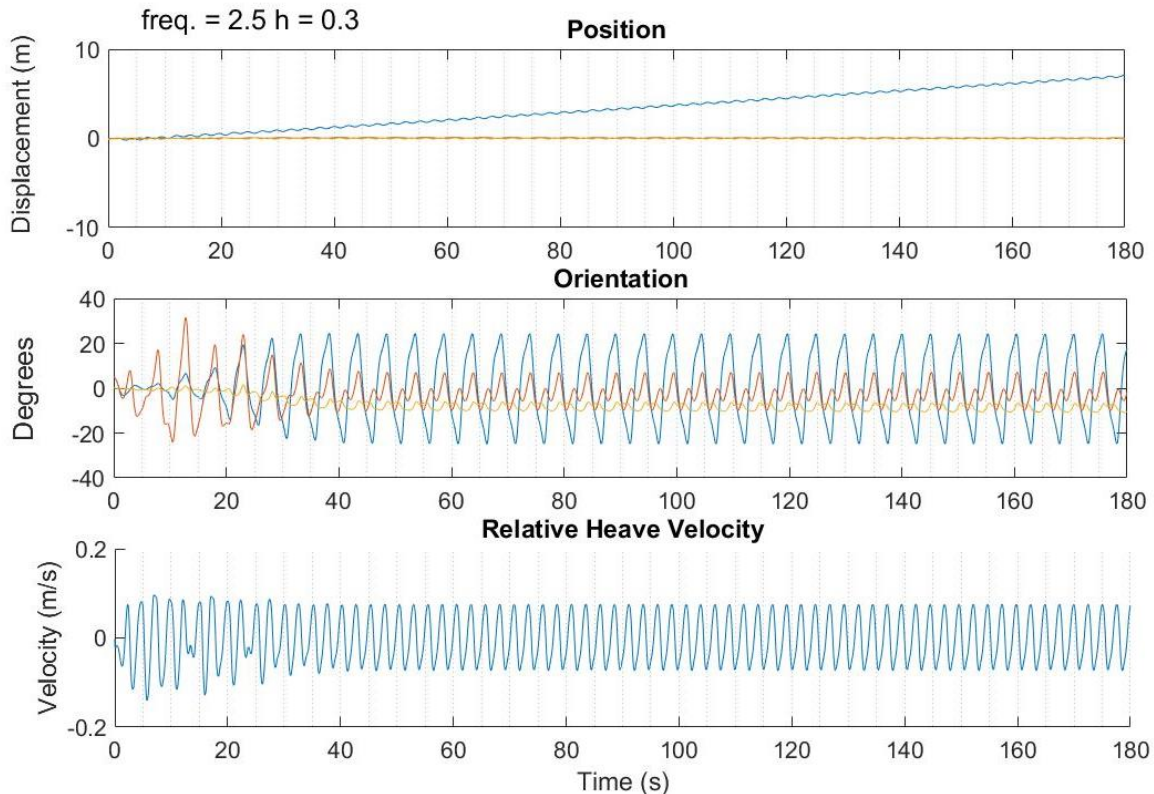


Figure 46: Time domain plot of the VISWEC at a frequency of 2.5 rad/s and wave height of 0.3 meters. The top showing position, middle orientation and bottom of relative velocity between the Spar and Float. The position/orientations are blue for surge/roll red for sway/pitch and yellow for heave/yaw.

For the second performance metric a single scalar metric was sought to capture the amount of roll and pitch oscillation present in any system. The single scalar metric is referred to as tipping magnitude (τ_{mag}) and is calculated using eq. (5.3) and eq. (5.4) where the final 20 oscillation amplitudes (θ_a, ϕ_a) were converted to a linear unit by taking the sine of the amplitude, were added and averaged giving a total average maximum magnitude of roll or pitch. The magnitudes of roll and pitch are then used in Pythagorean's theorem to give a total maximum displacement τ_{mag} . To assist in the visualization of this calculation, Figure 47 shows how each component, roll and pitch angle, is used to calculate a tipping magnitude. There will be no tipping magnitude calculation for the Heave Only scenario as there will be no tipping kinematically allowed. Additionally, tipping magnitude will be referred to as rolling magnitude in the Heave and Roll case as there will only be a contribution from the rolling motion, no pitching kinematically allowed.

$$\theta_{mag} = \sum_{end-20}^{end} \sin(\theta_a) / 20; \phi_{mag} = \sum_{end-20}^{end} \sin(\phi_a) / 20 \quad (5.3)$$

$$\tau_{mag} = \sqrt{\theta_{mag}^2 + \phi_{mag}^2} \quad (5.4)$$

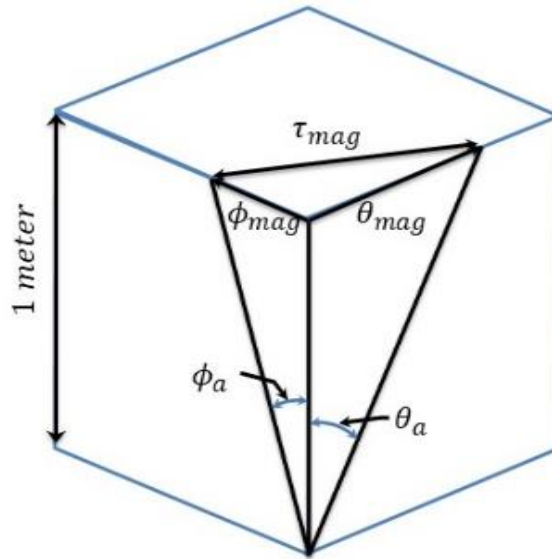


Figure 47: Visualization of the calculation of tipping magnitude

5.3 Simulation Results

5.3.1 Heave Only

The heave only scenario, as previously mentioned, provides a baseline measure of the system motions and performance for both the 2-body and 3-body systems. This case is not subject to the problem of parametric excitation and a focus of the work is in seeing how this is compromised as parametric excitation is introduced. If the suggestion from past work that the rolling motions are correlated with decreased power production is correct, then the power observed in this scenario will be the maximum. This scenario should also provide evidence that there is indeed a reason for implementing the 3-body system as past work by Bubbar has shown that there is a performance boost possible when the rotational inertia and PTO damping are properly set [25].

In the 2-body results, Figure 48a, if a line is drawn at a single wave height across all frequencies a dip, or valley, in power production can be observed around 2.65 rad/s. This valley corresponds to the bandwidth in which the PTO value was found to fall short of the optimal value in Section 4.3.3 (Figure 41) thus making the PTO value sub-optimal in this range. While the sub-optimal PTO value is not very apparent in power production at lower wave heights, the consequences are exacerbated as wave height increases. Additionally, at smaller wave heights there is little dependence of frequency on power production as the contour lines are generally level. However, as wave height grows there is a significant increase to the dependence of frequency on power production. There are two distinct regions of increased power production separated by the valley previously mentioned.

The 3-body results, Figure 48b, show similar trends but the valley in power production of the system seems to have increased and shifted to approximately 2.3 rad/s. This shift in the valley follows the shift in the peak PTO value shown in Figure 43, meaning the PTO value of the 3-body system is also sub-optimal akin to the 2-body system. Additionally similar to the 2-body system is the 3-body system's frequency dependence on power, however the dependence is reduced, observed by the generally consistent power production across a steady wave height. Moreover, the implementation of the VIS, shown in Figure 42 (2.125 – 3.7 rad/s), shows a relation to the valley of power production, the lower frequency delineating a sharp decrease of power production into the valley of reduced power production. Also notable is the beginning of a second valley towards the upper limit of tested frequencies, 4.0 rad/s.

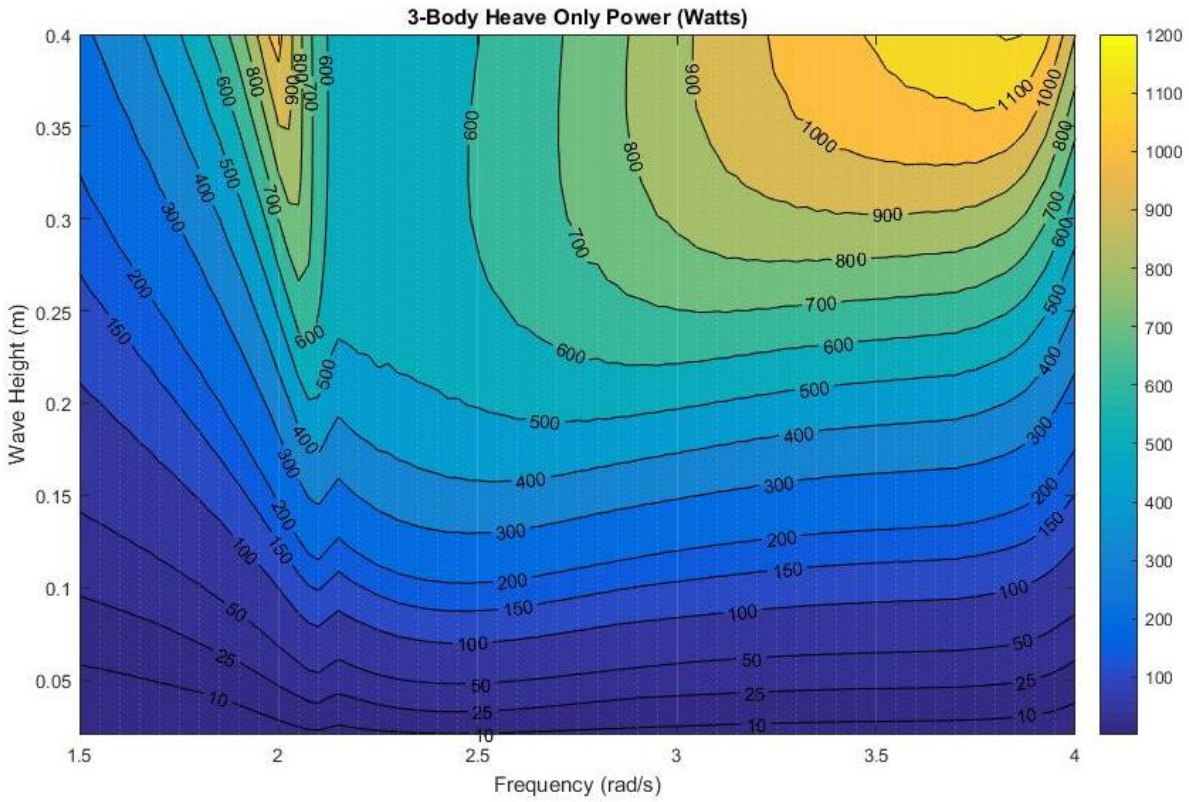
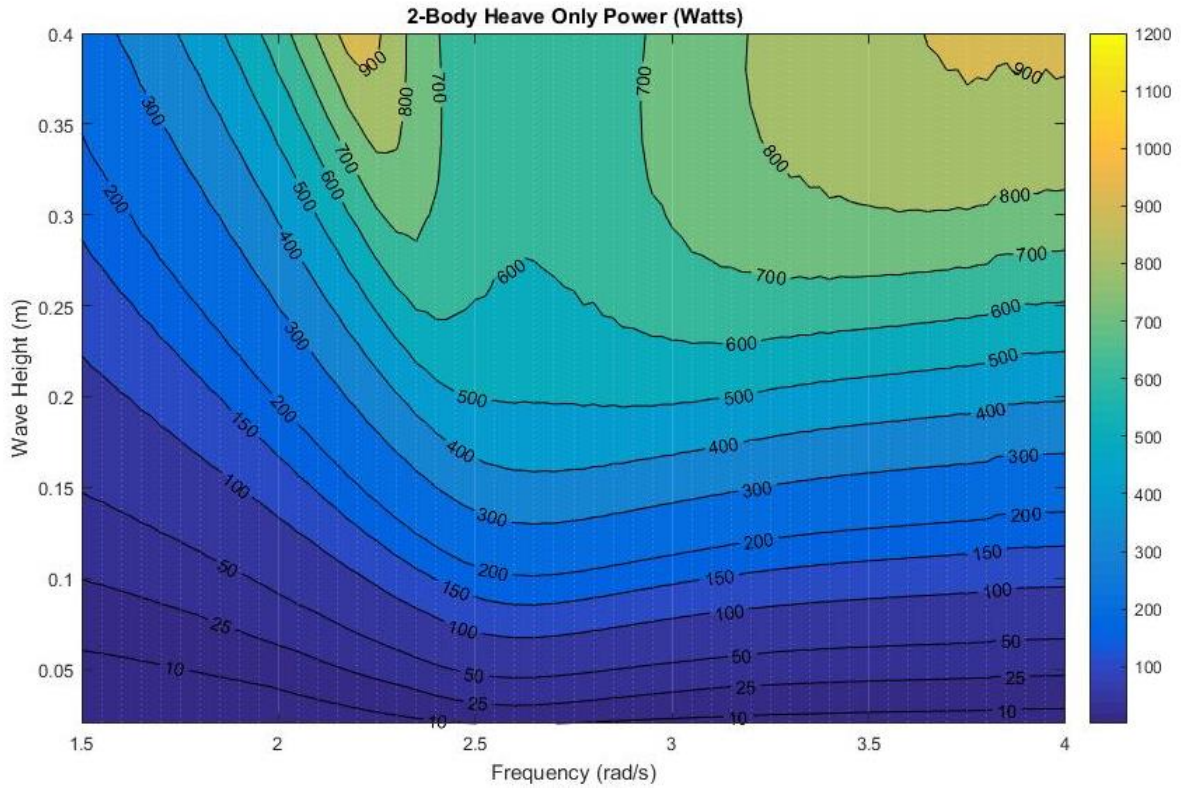


Figure 48: Heave Only a) 2-body and b) 3-body results

5.3.2 Heave and Roll

The Heave and Roll scenario is the simplest scenario that can still provide insight into the impact of parametric excitation. This case will isolate the roll mode of motion that is affected by parametric excitation. Pitching motion is also effected by parametric excitation however, the pitch DoF is heavily affected by the wave forces and moments making it difficult to differentiate contributions between parametric excitation and regular wave forcing. Unidirectional regular waves provide no direct forcing in the roll DoF and thus any rolling motion will be indicative of parametric excitation.

For both systems an initial roll displacement of 5 degrees (0.087 m) in the rolling DoF to ensure any effects from parametric excitation had a chance to develop within the 180 seconds simulations. In nature this perturbation is provided by wind, asymmetry of the approaching wave, or any other environmental force. Drag and damping forces resist any motion so if the system is not internally excited, there should be no rolling magnitude present.

The power production results of the 2-body system, Figure 49a, closely resemble that of the previous Heave Only case with the exception of a larger reduction in power production around the same valley of reduced power production shown in Figure 48a. Rolling motion shown in Figure 49b, can be seen to exactly match up with the increased reduction in performance compared to the Heave Only case. The valley of reduced power production has moved to a lower frequency because the contribution to the reduction of power is dominated by the increase in roll magnitude instead of the sub-optimal PTO damping value as demonstrated by the previous case.

In Figure 49b rolling magnitudes show the smallest bandwidth and magnitude of response at the minimum wave height then both magnitude and bandwidth increase with wave height up to 0.3 meters where the bandwidth of response begins to decrease and magnitude continues to increase with wave height. Additionally, the peak of the roll response remains constant at approximately 2.5 rad/s which is close to twice the natural roll frequency of the connected and locked values presented in Table 8.

Comparing the rolling response in Figure 49b and that of the test case in Chapter 2, the responses match in that the bandwidth of response grows with wave height but contrast as the wave height increases past 0.3 meters. The difference above a wave height of 0.3 meters must mean that a form of damping is starting to dominate the system, this contribution was not considered in the test case but is shown in other works [58], [60].

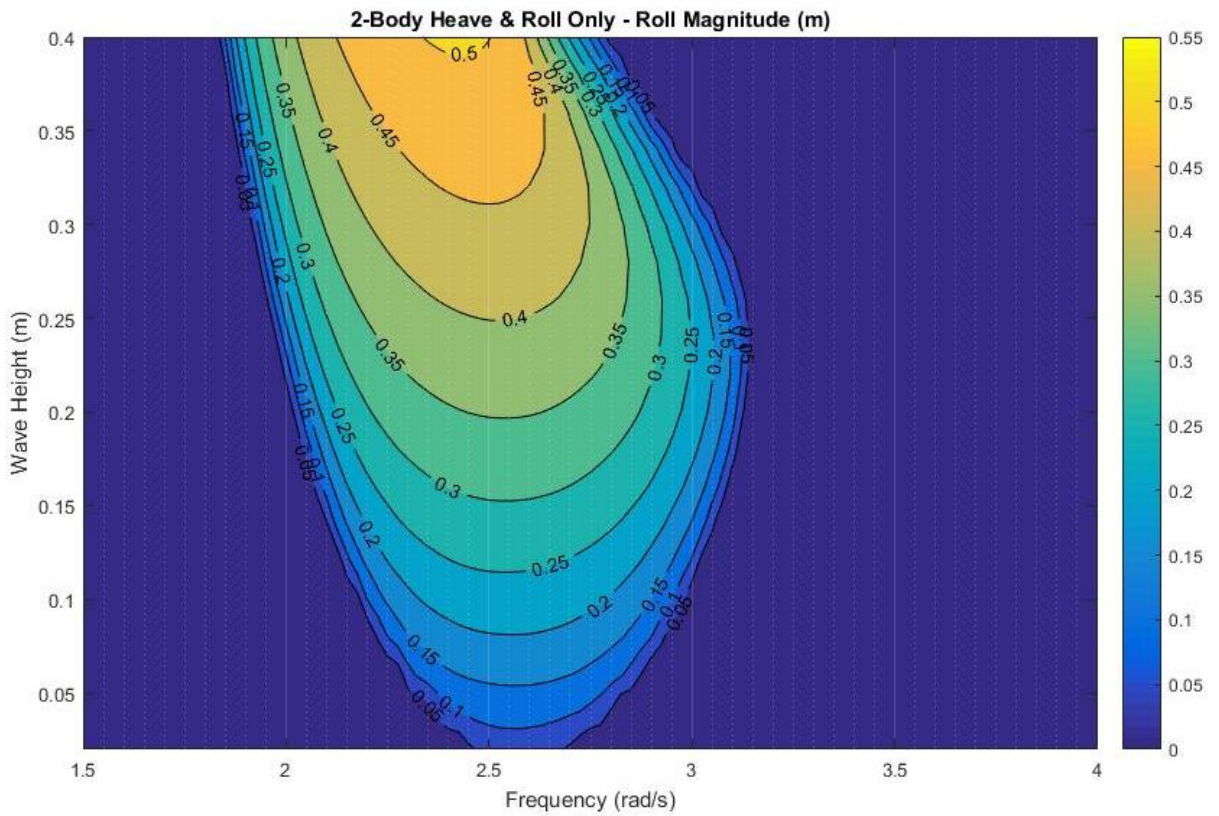
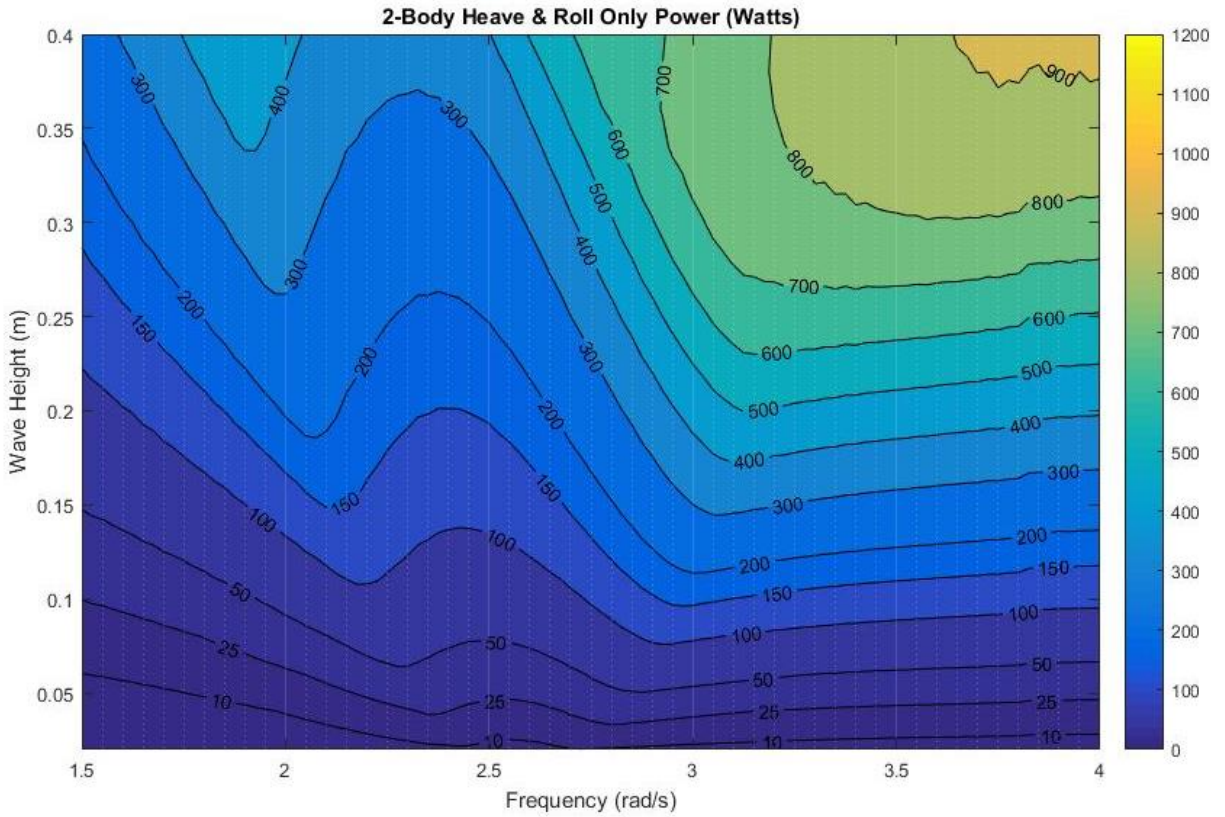


Figure 49: 2-body Heave and Roll Only a) Power Production and b) Rolling Magnitude

The 3-body power production results, Figure 50a, of Heave and Roll show similar results to the previous 3-body Heave Only case with the exception of a larger valley of reduced power production both in bandwidth and magnitude. Similar to the 2-body Heave and Roll case, the reduction in power production matches precisely with the Rolling magnitudes present in Figure 50b. In contrast to the 2-body Heave and Roll, the valley of reduced power production has not moved compared to the 3-body Heave Only case suggesting the system is still dominated by the same parameters.

The rolling magnitude results, Figure 50b, show a drastic increase from no response on the lower end of frequency response, but this response only appears at wave heights above 0.14 m. Wave heights 0.01-0.05 m resulted in no developed rolling motion, the response begins above 0.05 m at a frequency of 3.35 rad/s. The bandwidth of response is small to negligible at low wave heights but increases dramatically at 0.14 m spreading across the range of the active VIS, 2.125-3.7 rad/s. The average of the rolling response drops sharply to the lower frequencies as wave height increases above 0.15 m.

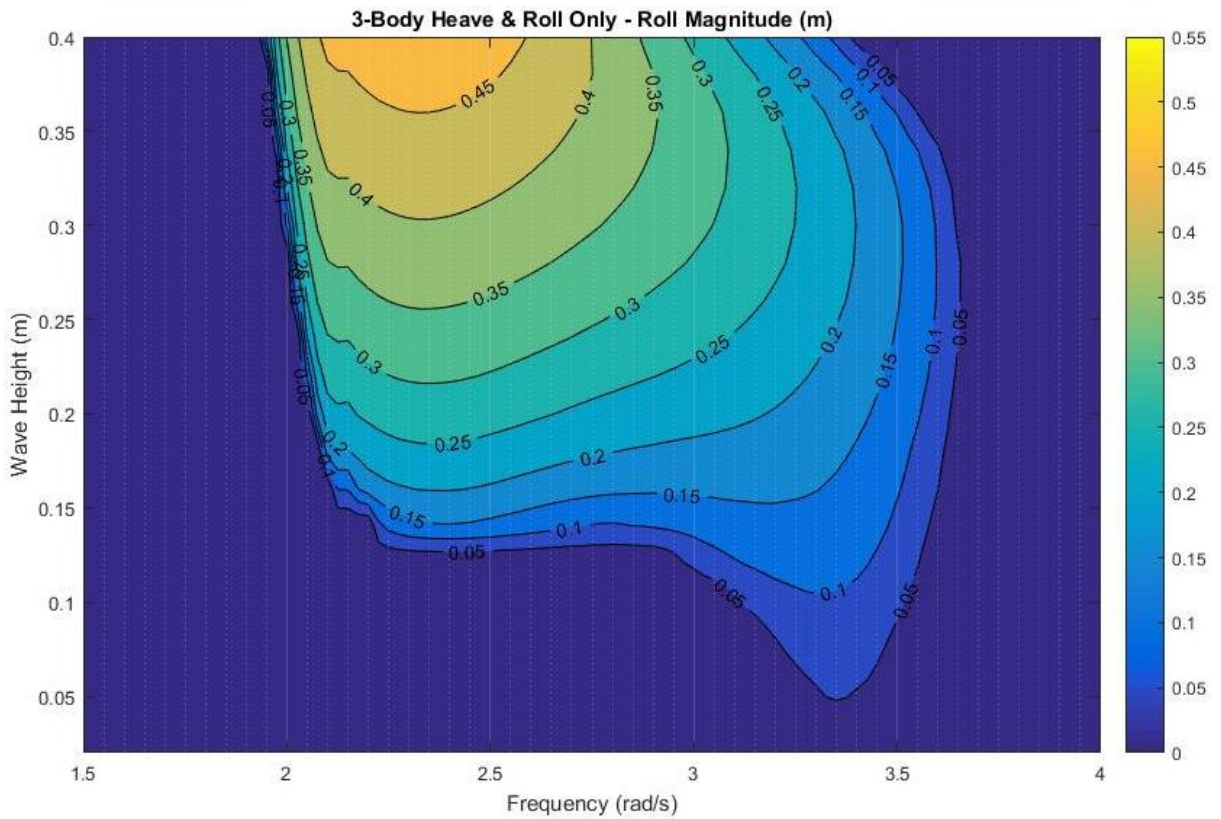
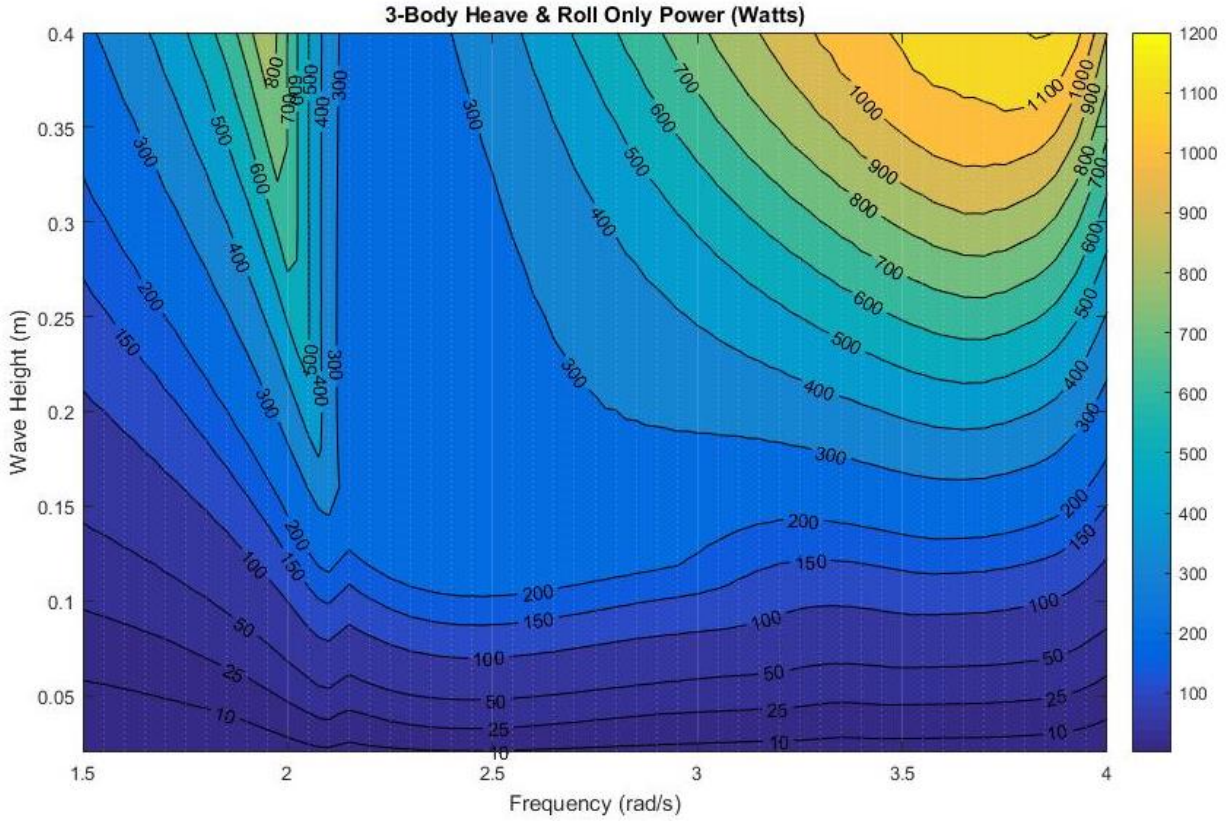


Figure 50: 3-body Heave and Roll Only a) Power Production and b) Rolling Magnitude

5.3.3 Moored

The third scenario of simulation is a case where surge and sway, translation, motions are inhibited but heave, roll, pitch and yaw are free. This scenario mimics the purpose of moorings, to keep a structure on station but doesn't add or detract from the dynamics of the system. This case will add the pitching DoF to the previous Heave and Roll case and most closely represents a WEC deployed at sea.

The moored 2-body power production, Figure 51a, shows similar trends as the previous Heave and Roll case without pitching motion, a valley of decreased power production at the same frequency (2.3 rad/s) due to rolling motions. Overall power production has decreased across the board with the exception of the low frequency, high wave heights. Interestingly power production has increased in this area despite the increase in DoF and tipping magnitude, Figure 51b. This power response must be because the system is pitching at the right phase with respect to the wave and increasing the relative velocity between the two bodies as the previous case shows there is no rolling motion.

The tipping magnitude results, Figure 51b, show what appear to be the results from the previous, Heave and Roll case with an addition of a mostly even magnitude of response across the span of frequencies increasing with wave height. The generally even distribution of pitching motion across frequency would indicate that pitching motion is generally dominated by the wave excitation forces as motion increases proportional with excitation forces. Another interesting point stems from drawing a line across a single wave height across the range of frequencies. This shows the tipping magnitude decreasing more dramatically at higher wave heights, before increasing significantly. The decrease in tipping motion is accompanied by an increase in power production.

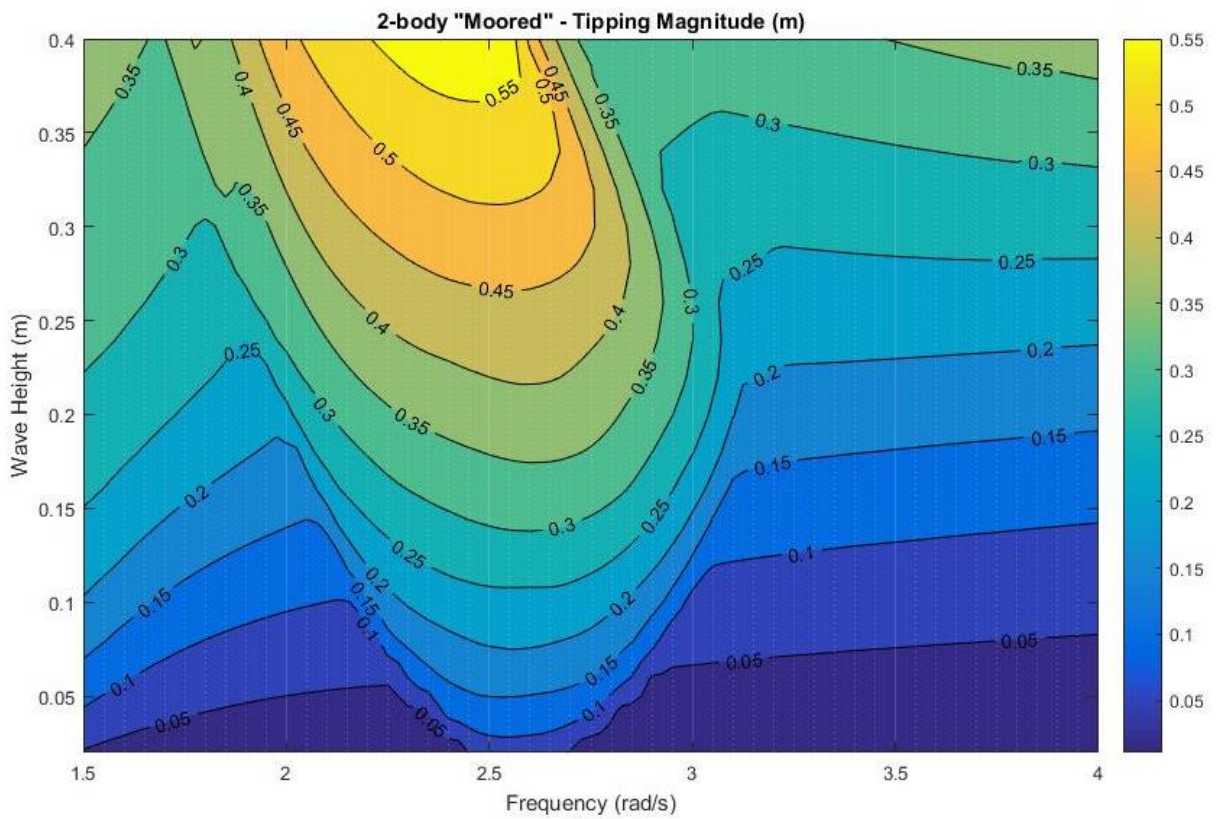
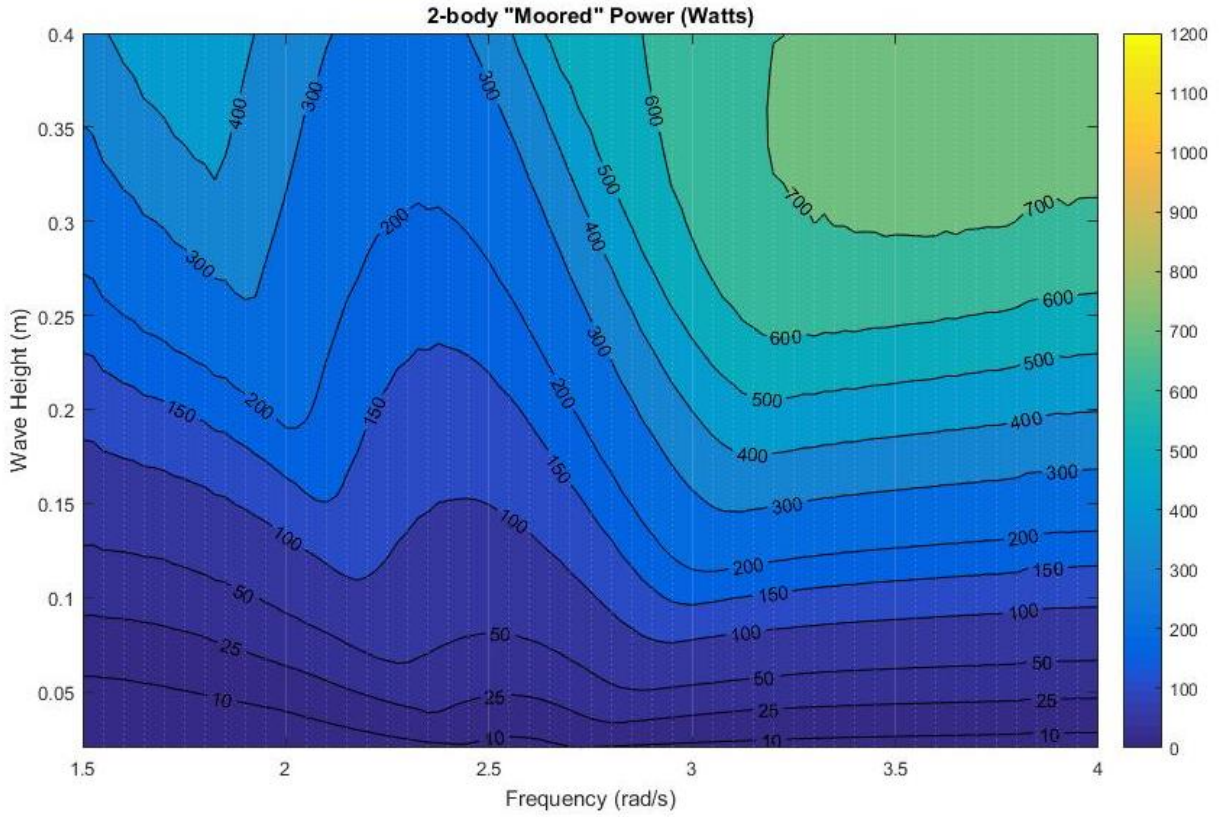


Figure 51: 2-body Moored a) Power Production and b) Tipping Magnitude

The 3-body results of power production, Figure 52a, show similar trends to the previous case of Heave and Roll for a 3-body system however, the overall power production is mostly reduced evenly across the domain. There is still a valley of reduced power production around a frequency of 2.3 rad/s due to rolling motion however, there is an increase in power production at the low range frequencies for larger wave heights compared to the 3-body Heave and Roll case previously presented. Similar to the 3-body Heave and Roll case, there is a larger reduction in power production at the lower range of frequencies approaching the limit of 4.0 rad/s.

The 3-body Moored tipping magnitude results, Figure 52b, shows increased motion in the lower frequencies as well as the similar rolling response trends as the previous Heave and Roll case. Again drawing a line across frequency at a single wave height, there is a significant reduction in the tipping magnitude before a large increase as seen in the previous 2-body Moored case. This trend between systems is similar to the reduction in magnitude of roll response before the increase of magnitude shown in the test case presented in Chapter 2; however the magnitude in the test case was not as dramatic. It would appear that this stabilization of the 3-body system tipping motion at these frequencies is more so than the corresponding 2-body resulting in increased power production.

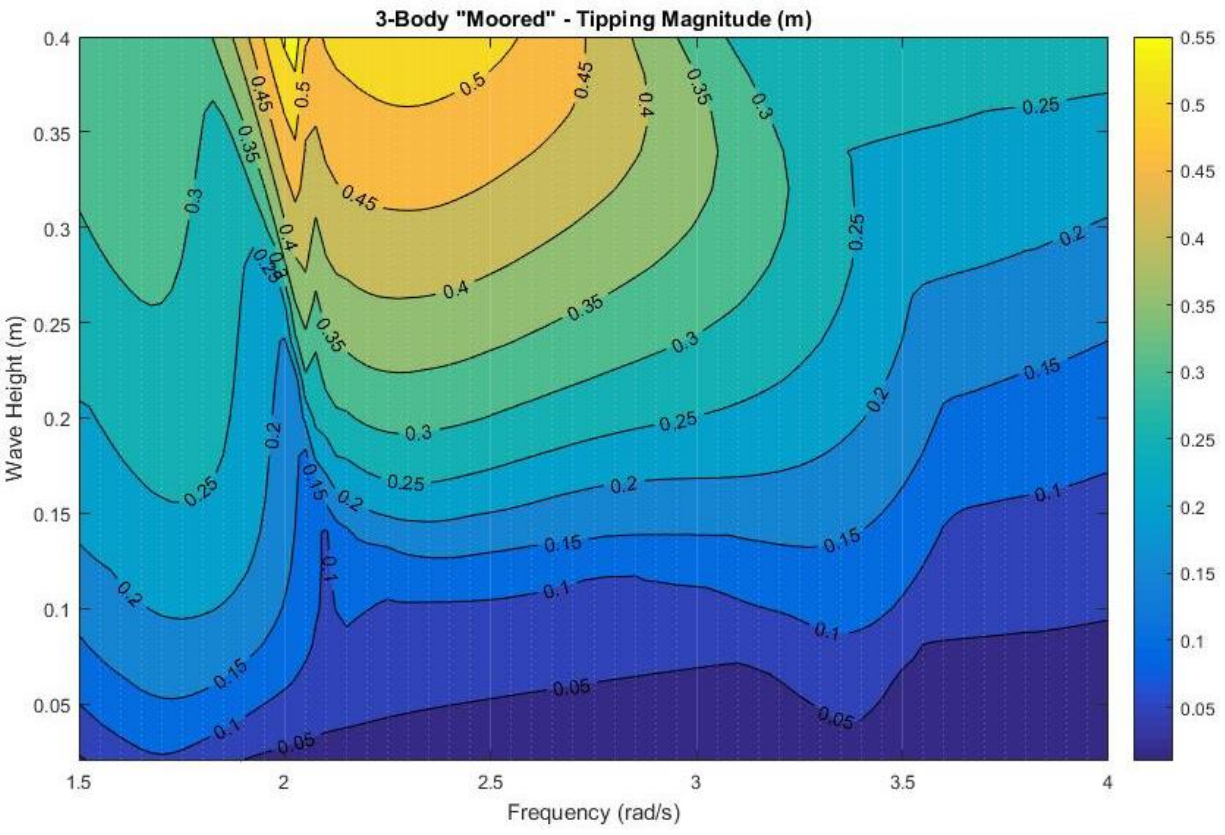
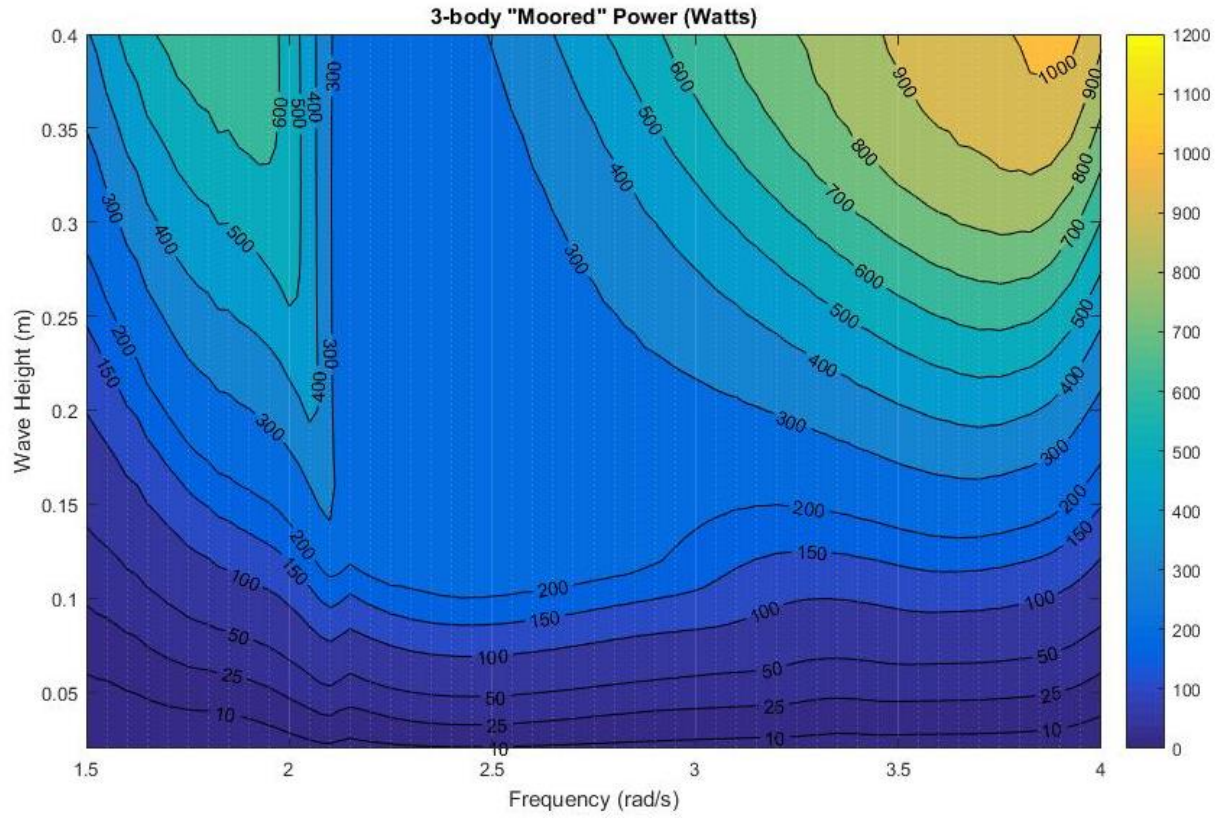


Figure 52: 3-body Moored a) Power Production and b) Tipping Magnitude

5.3.4 Free

The final kinematic scenario is fully unconstrained in order to observe the free dynamics of the system. This scenario will show if there is any substantial drifting effects as well as any other phenomenon that may occur. This is not considered a realistic scenario as a device could not be allowed to float freely but is important information for this and any future work pertaining to the VISWEC as it could present insight to wave drifting forces and possible mooring configurations just as each of the previous results.

The Free 2-body power production results, Figure 53a, show similar results as the 2-body moored case, the main difference manifesting at the low frequency range. At the frequency range 1.5 – 2 rad/s the power production relates more to that of the 2-body Heave and Roll case than the Moored case. However, at a frequency range of 3.3 – 4 rad/s Free 2-body power production matches that of the moored case more so than the Heave and Roll only. The valley of reduction in power production between these two ranges is more prominent than any previous case and occurs at a slightly higher frequency than any of the previous cases. The change in center of the valley of power reduction is most likely caused by the change in encounter frequency, or the frequency at which the body encounters the wave, due to surging motion.

The tipping magnitude results of the Free 2-body system, Figure 53b, shows a lower overall addition of magnitude to the 2-body Heave and Roll results than the 2-body Moored case. This reduction in tipping magnitude is due to drifting of the system, the power in the pitching DoF has been dissipated to the sway DoF, keeping the system more upright but still detracting power from the PTO. The tipping magnitude has a wider bandwidth than that of any of the previous 2-body cases, aiding in the reduction of power. Also noted is the disappearance of the significant decrease in tipping magnitude before the step increase across frequency at a single wave height displayed in the 2-body Moored case.

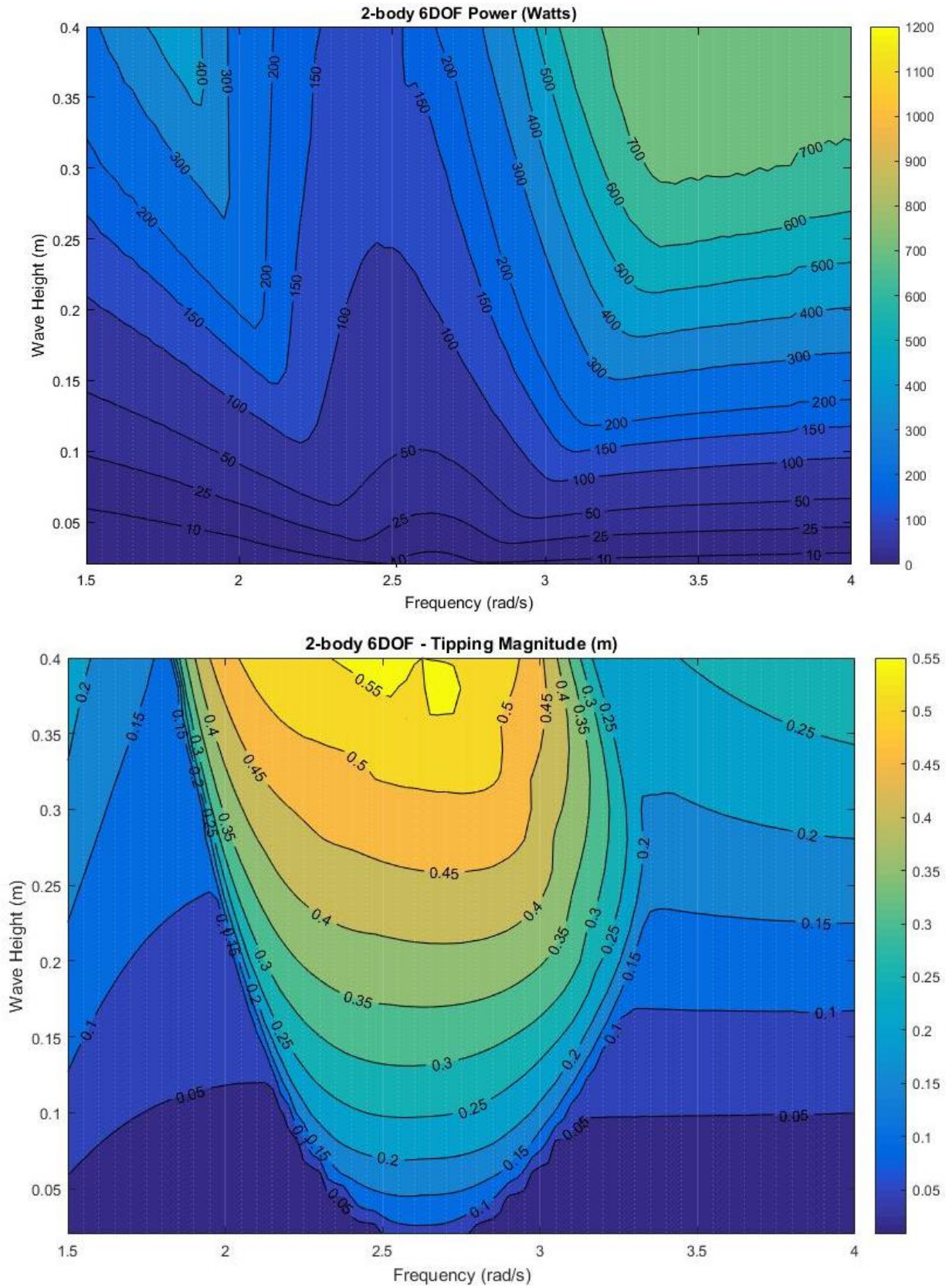


Figure 53: 2-body Unconstrained a) Power Production and b) Tipping Magnitude

The Free 3-body power production results, Figure 54a, shows a larger reduction of power in the valley seen in the previous 3-body results as well as across most frequencies and wave heights. The only exception again being at the low frequency large wave height where there is increased power production compared to the 3-body Heave and Roll results but not as much as the 3-body Moored results. The valley of power reduction at 2.35 rad/s is greater in magnitude and at a higher frequency than any previous 3-body case.

The tipping magnitude results of the Free 3-body, Figure 54b, shows a similar but greater increase in magnitude to that of the 3-body Moored case at the lower range of frequencies (1.5–2.1 rad/s). Furthermore, a larger bandwidth of tipping magnitude than that of any previous 2-body or 3-body case spanning frequencies 2.15–3.6 rad/s is observed. The drop in tipping magnitude before the increase at a single waveheight across the range of frequency is less than the previous 3-body Moored case. On the higher end of the range of frequencies (3.8–4.0 rad/s) there is an increase in tipping magnitude unseen in previous 3-body cases, especially at the larger wave heights (0.35-0.4 m).

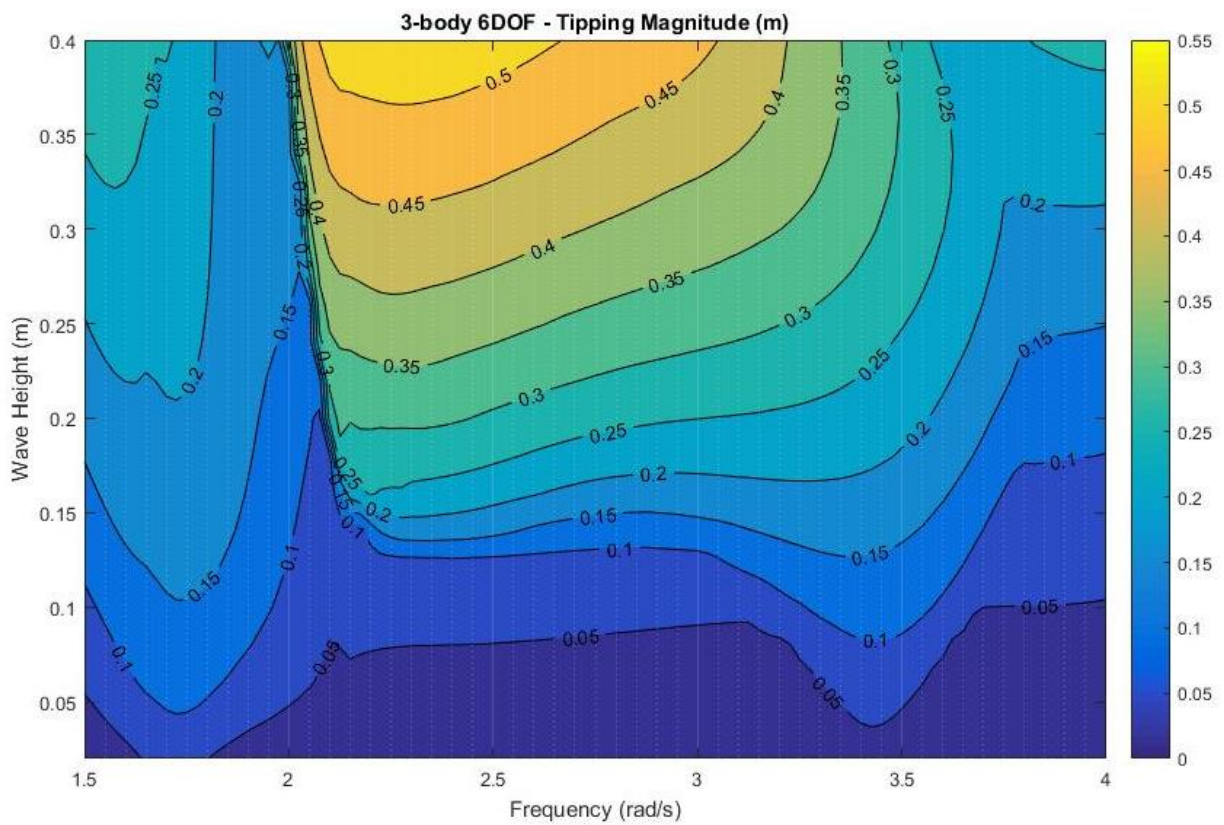
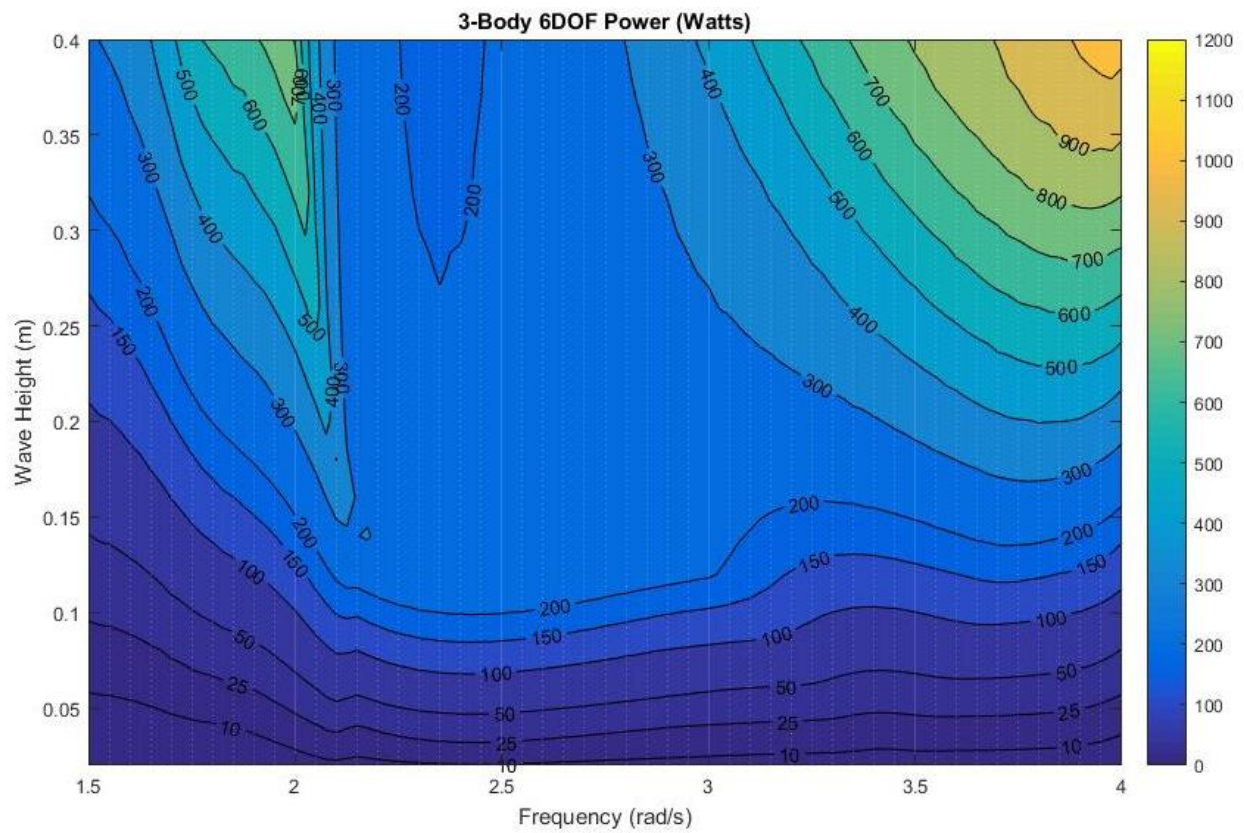


Figure 54: 3-body Free case results of a) Power Production and b) Tipping Magnitude.

5.4 Comparison of Results

In this section the results of the previous section are directly compared in two ways. First, the 2-body and 3-body system results are compared across the scenarios to reveal relative differences in the performance metrics for each system as new DoFs are added. Second, the comparisons of the 2-body against the 3-body system in each kinematic scenario will give insight to the benefit of the implementation of the VIS within the VISWEC.

5.4.1 Two-body System Comparison

The results of the two systems, 2-body and 3-body, presented in decreasing kinematic constraints provides insight to the efficiency of power production as more degrees of freedom are unlocked. Figure 55 presents a comparison of the 2-body system results for power production for the heave-roll, moored and free scenarios normalized against the power production of the heave only scenario. Red areas show where the power production of the Heave Only case outperformed the compared kinematic case, black areas indicating similar power performance. Generally speaking, as DoFs are increased, the power production is decreased. As mentioned previously, this follows reason as there is a limited amount of power captured by the VISWEC and as motion is allowed and absorbed into these non-power producing DoFs it detracts from the amount of power in heave, directed through the PTO. The exception to this theory is visible in the Moored and Free comparisons with the red areas, considering this increase in power production is not present in the Heave and Roll comparison it is logical that the increase in power is caused by pitching motions caused by wave excitation.

The comparison of the Heave Only and Heave and Roll clearly show the power reduction due to rolling motion at a frequency approximately that of twice the roll natural frequency of the locked and connected cases presented in Table 8 and validated with the test case of Section 2.5. This relation between the excitation frequency and natural frequency would suggest that parametric excitation is accountable for the rolling motion and thus the reduction in power production.

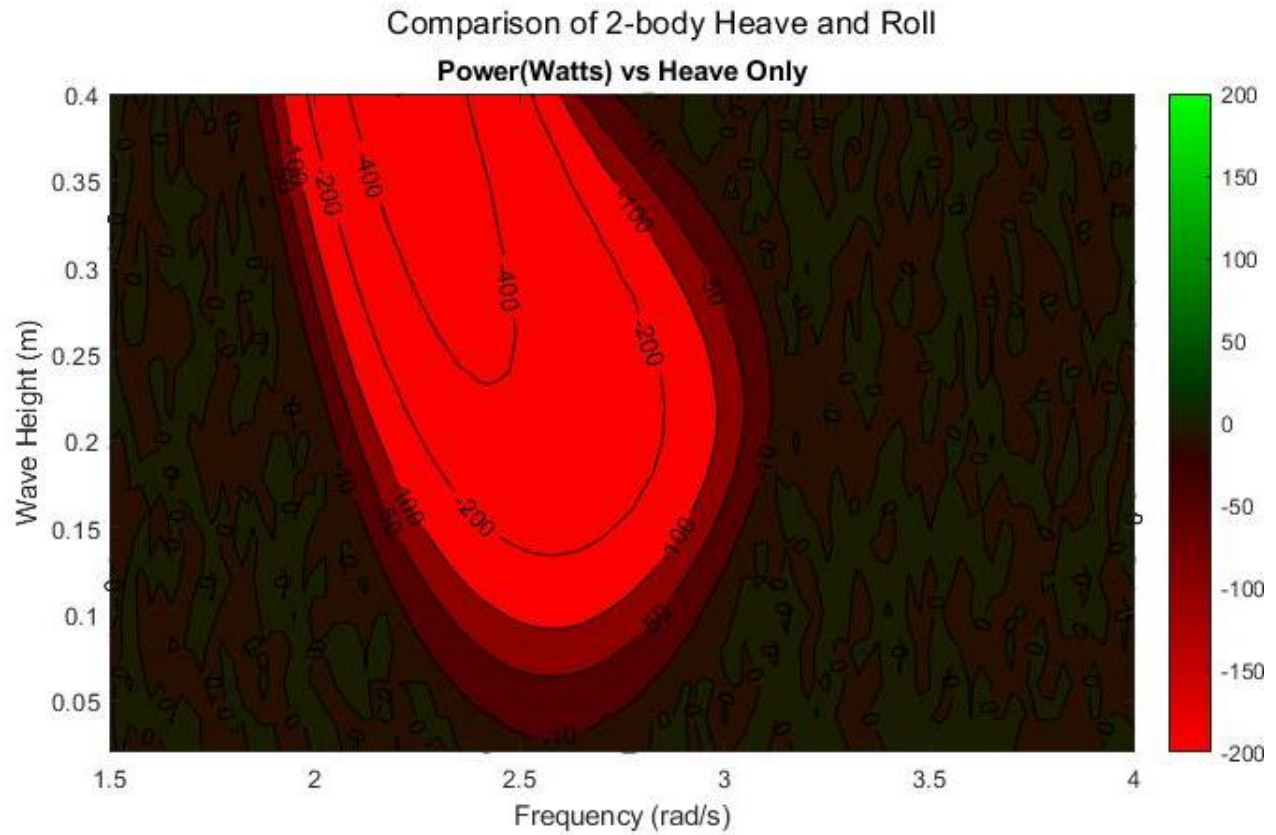


Figure 55: Comparison of 2-body power production in Watts between the Heave only case and Heave and Roll case, green shows where the Heave Only out performs Heave and Roll and red shows the contrary.

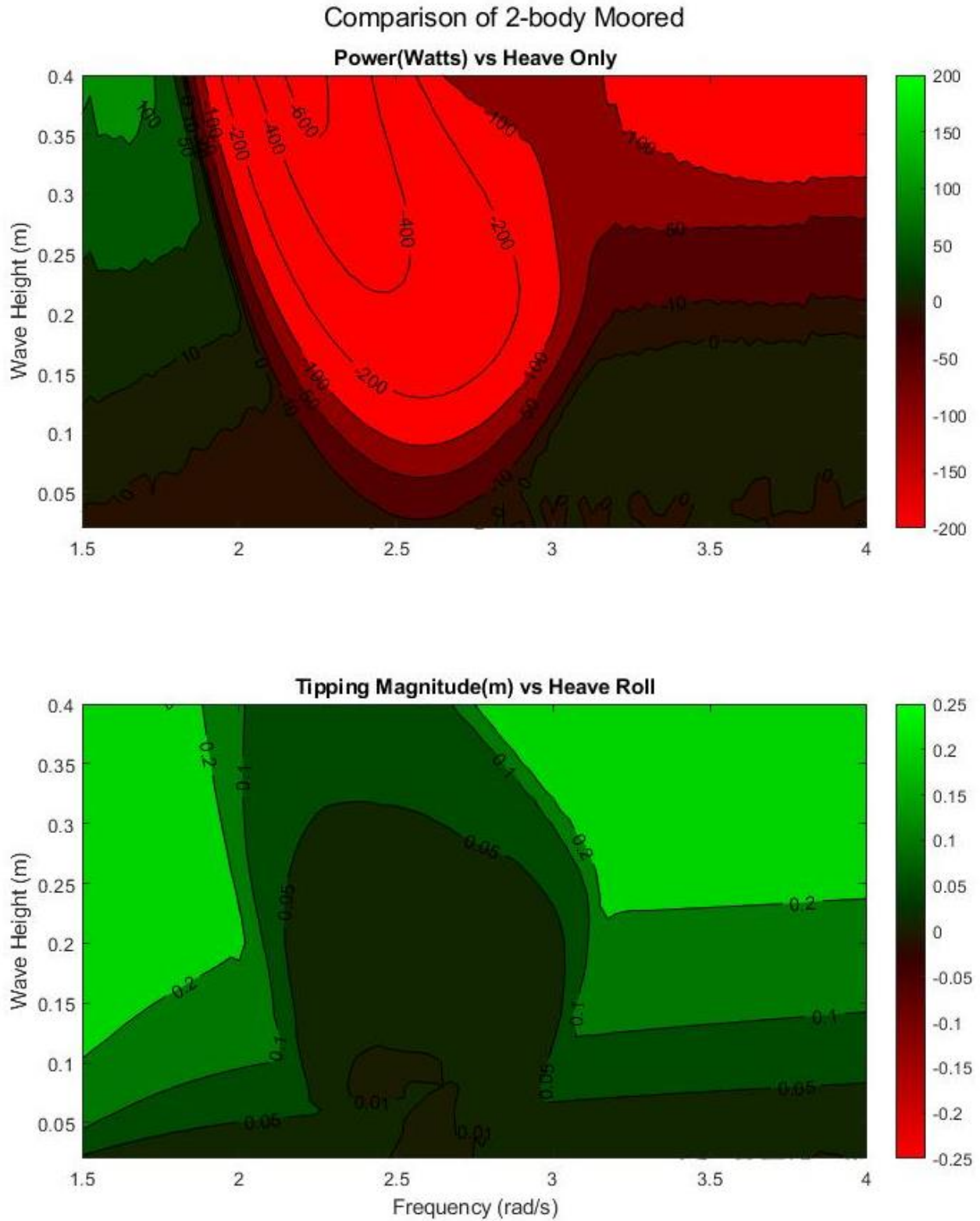


Figure 56: Comparison of 2-body a) power production in Watts between the Heave only case and Moored case and b) tipping magnitude in meters between the Heave and Roll case and Moored case, Green shows where the Moored values are larger, red shows the contrary.

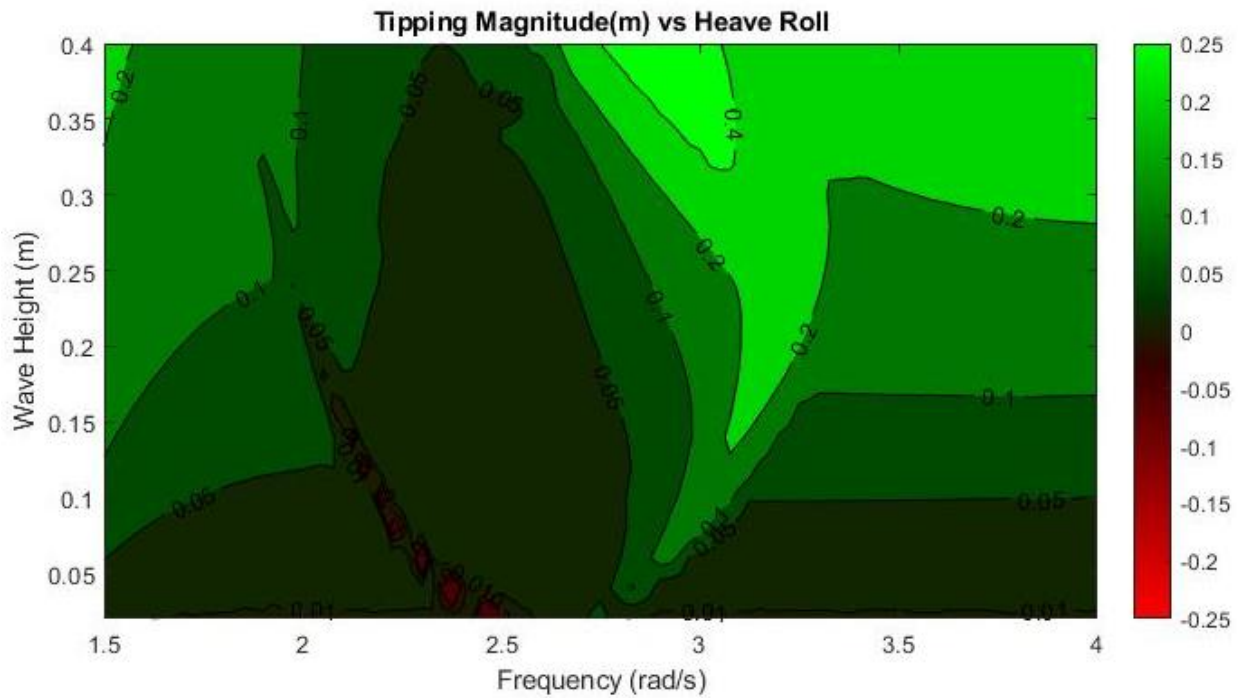
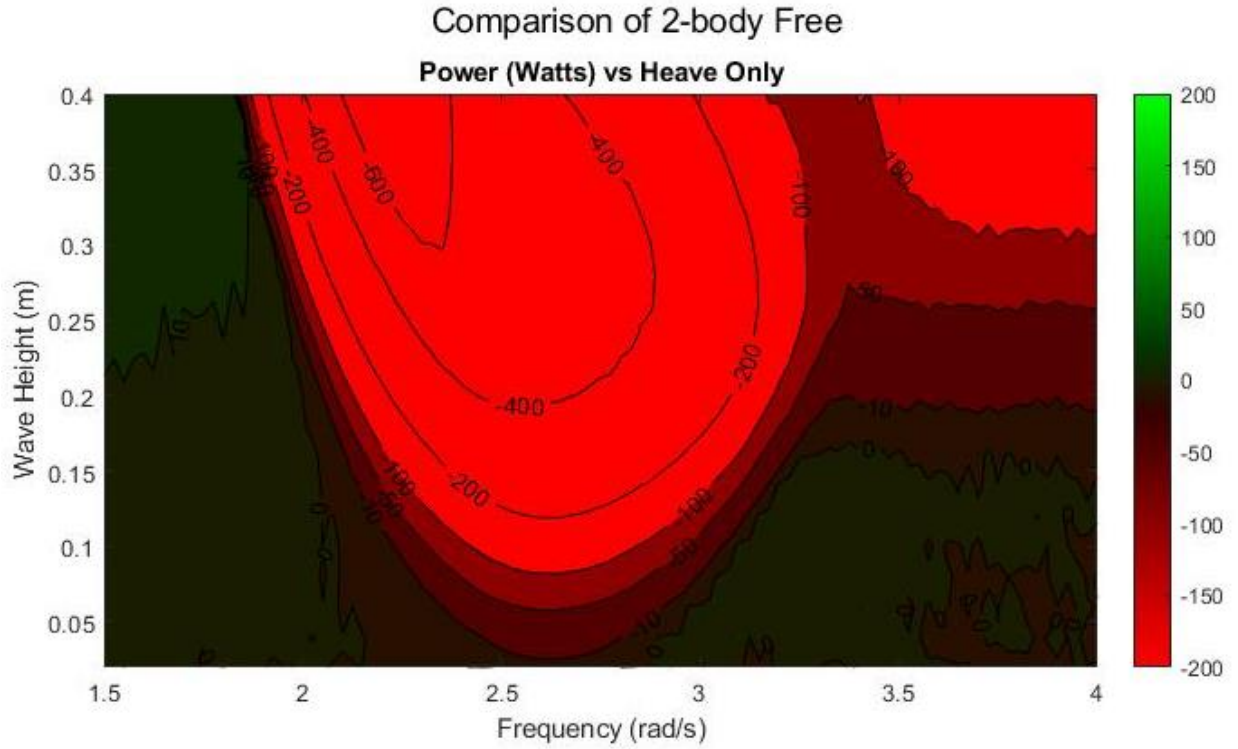


Figure 57: Comparison of 2-body a) power production in Watts between the Heave only case and Free case and b) tipping magnitude in meters between the Heave and Roll case and Free case, Green shows where the Moored values are larger, red shows the contrary.

5.4.2 Three-body System Comparison

Figure 58 presents a comparison of the 3-body system results for power production for the heave-roll, moored and free scenarios normalized against the power production of the heave only scenario. Red areas show where the power production of the Heave Only case outperformed the compared kinematic case, black areas indicating similar power performance. Again, generally speaking, as DoFs are unconstrained power production is reduced. The same exception applies to the 3-body comparison as the 2-body comparison where pitching motion appear to increase the power production higher than that of the Heave Only case. The reductions in power have a lower magnitude than that of the 2-body comparisons although the bandwidth is significantly greater.

If the 2-body cases present parametric excitation indicated by increased rolling motion in the Heave and Roll case accompanied by a reduction in power production then it could be interpolated that the reduction in power present in the Heave and Roll case comparison is indicative of parametric excitation. The conflicting argument here would be that the roll natural frequency presented in Table 8 has not changed so the bandwidth of roll response should not have changed. Although there is still an observed decrease in power production and increase in rolling magnitude for the 3-body Heave and Roll case.

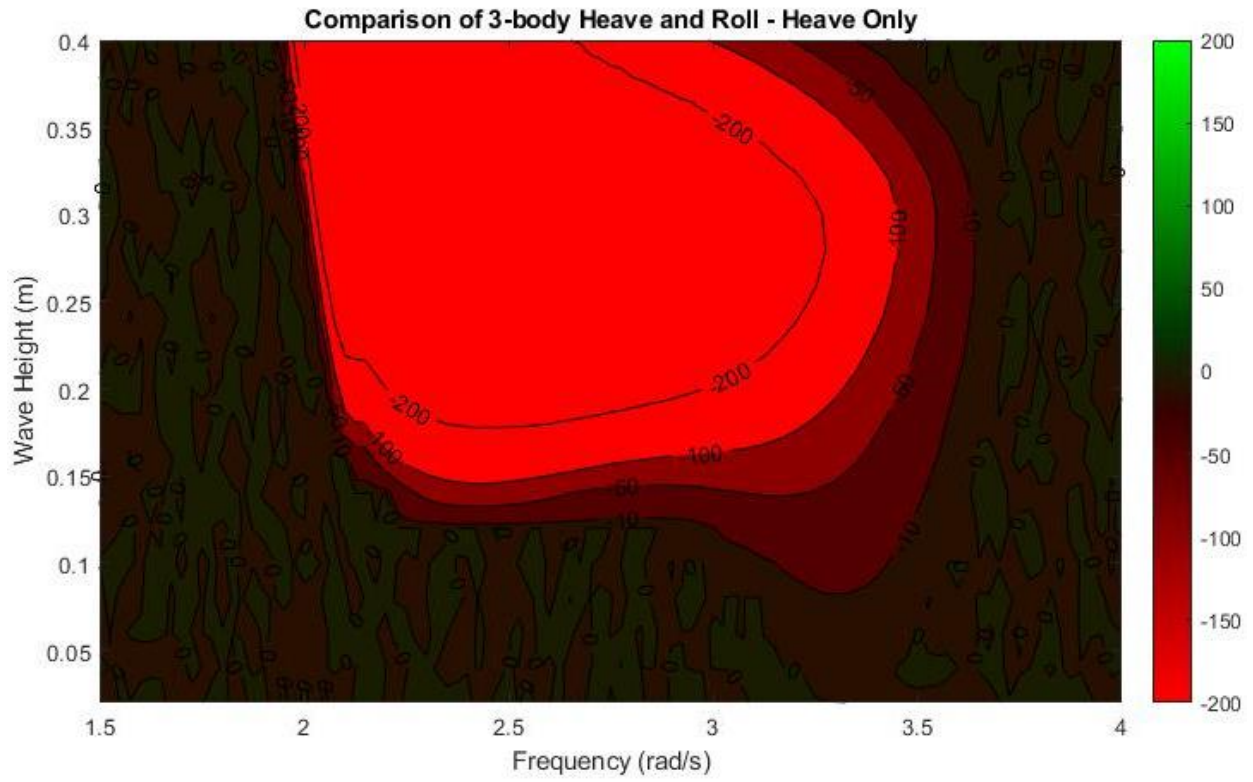


Figure 58: Comparison of 3-body power production in Watts between the Heave only case and Heave and Roll case, green shows where the Heave Only out performs Heave and Roll and red shows the contrary.

Comparison of 3-body Heave, Pitch, Roll - Heave Only

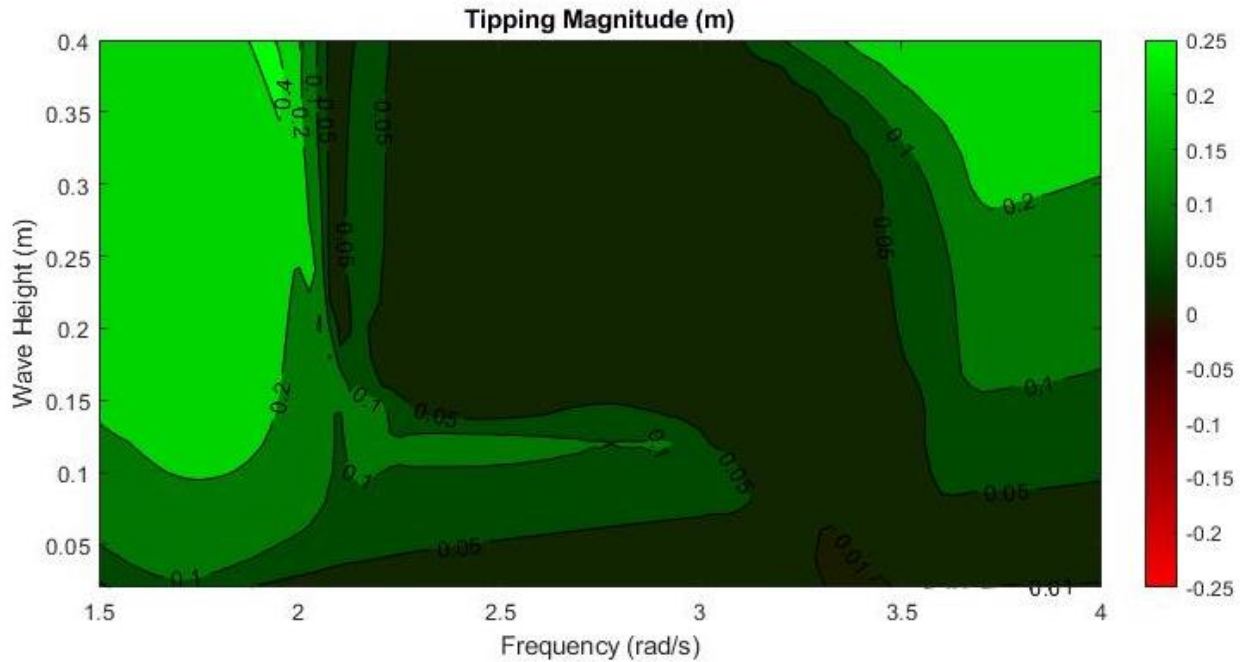
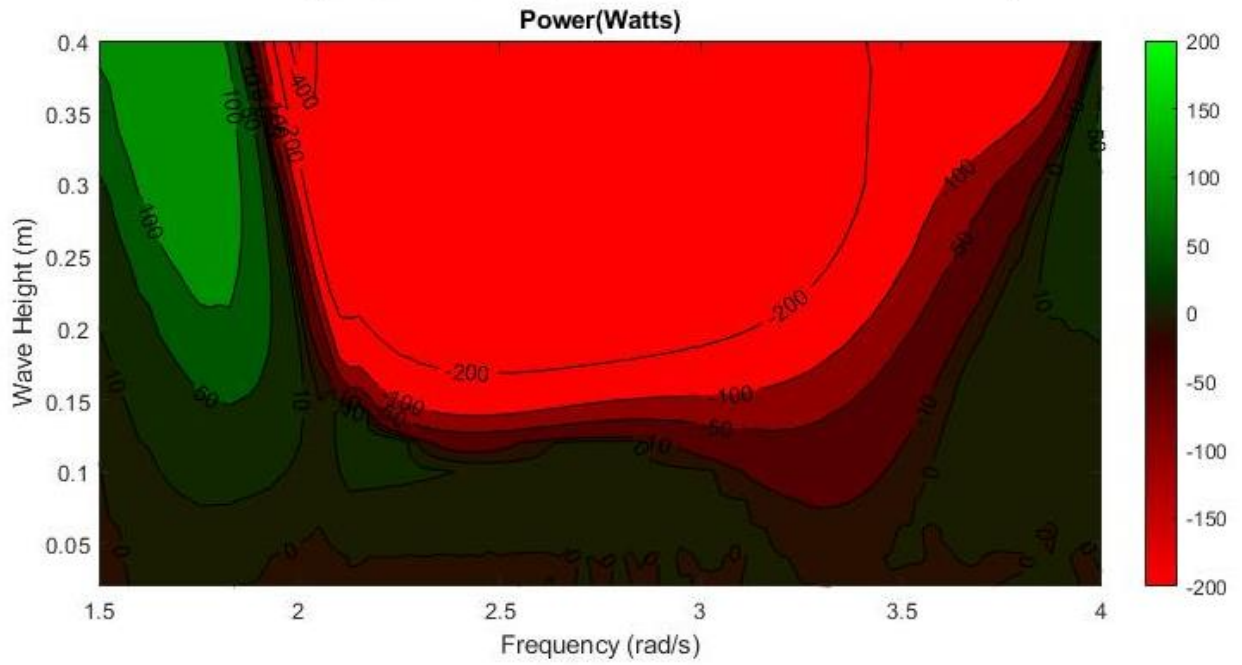


Figure 59: Comparison of 3-body a) power production in Watts between the Heave only case and Moored case and b) tipping magnitude in meters between the Heave and Roll case and Moored case, Green shows where the Moored values are larger, red shows the contrary.

Comparison of 3-body 6-DoF - Heave Only

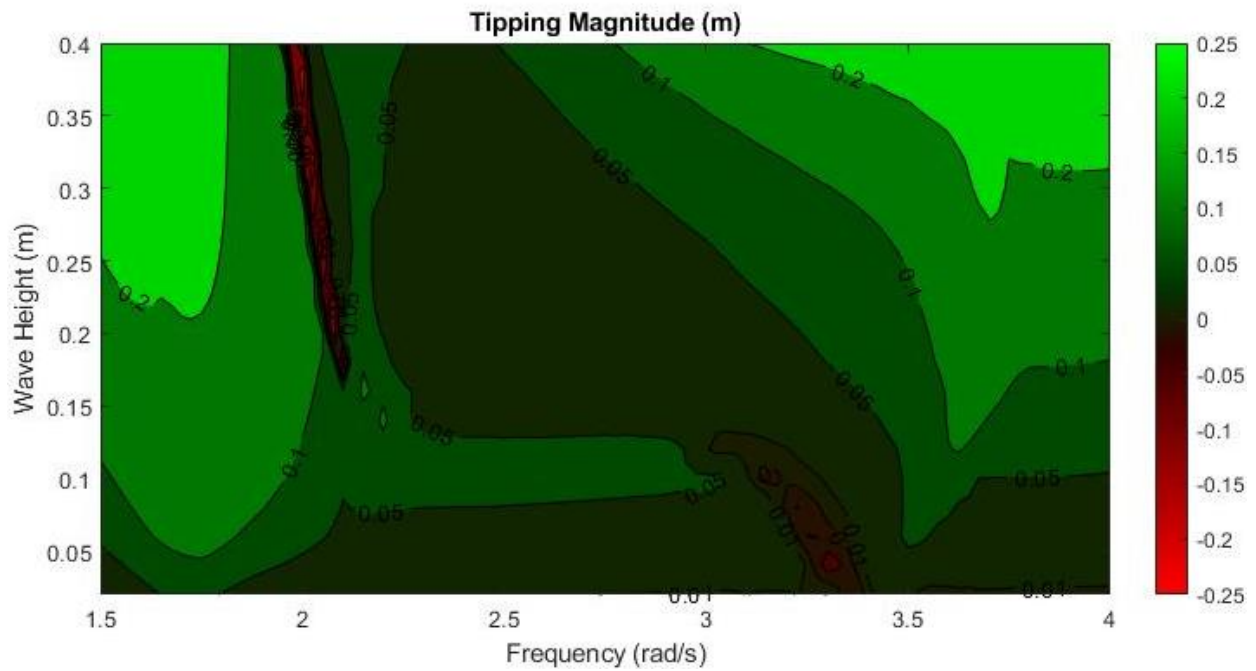
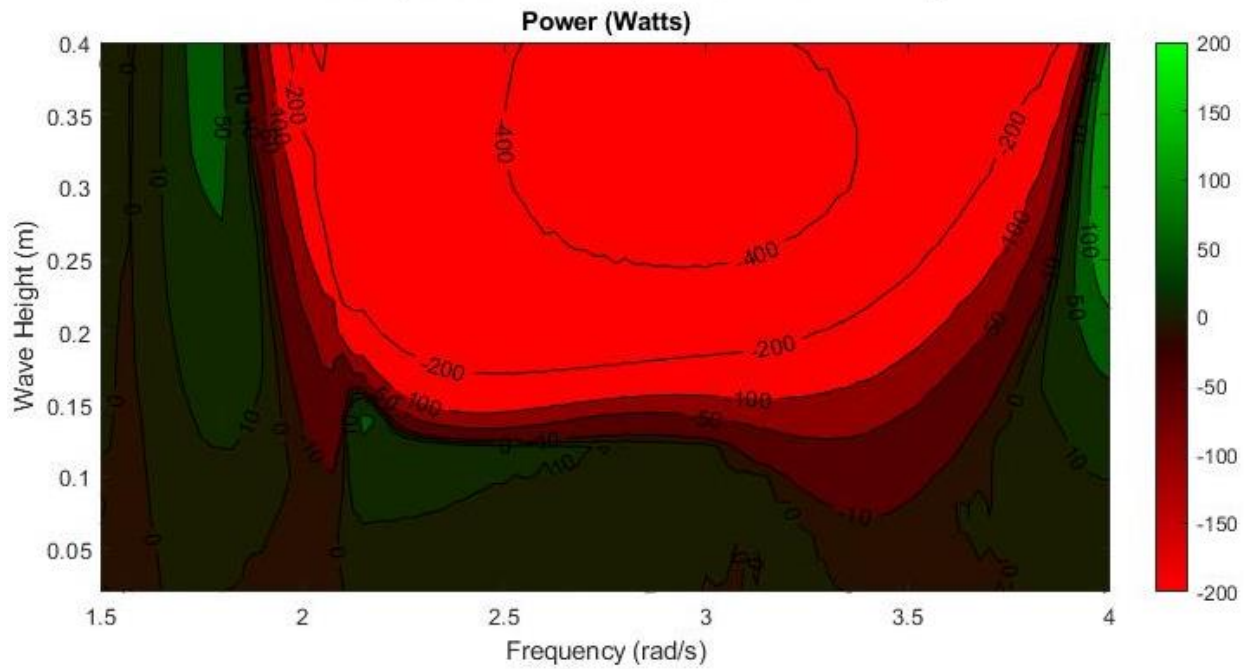


Figure 60: Comparison of 3-body a) power production in Watts between the Heave only case and Free case and b) tipping magnitude in meters between the Heave and Roll case and Free case, Green shows where the Moored values are larger, red shows the contrary.

5.4.3 Inter-system Comparison

The comparison between the 2 and 3-body power productions give insight into whether or not the implementation of the VIS would be beneficial. At a frequency of approximately 2.5 rad/s, in the heave only case, the 2 and 3-body systems produce the same amount of power. This is also where the PTO value of both systems match as shown in Figure 43. In all other kinematic cases, the 3-body system outperforms the 2-body system at lower, more common wave heights. Considering the PTO damping value was non-optimal at the system's natural frequency (peak PTO value) and the 3-body system is designed to change the system's natural frequency, the PTO value is most likely non-optimal across the frequency range where the VIS is active. The shortcomings of the PTO in the 3-body system could partially account for the 2-body system outperforming the 3-body system at the 3.0 – 3.6 rad/s frequency range. Another portion could be accounted for the 3-body system having increased rolling motion at the 3.0 – 3.6 rad/s frequency range where the 2-body system does not.

The fact that the 2-body system is outperforming the 3-body system when the 3-body system is rolling means that the increase in estimated power production from the implementation of the VIS does not overcome the loss in power from rolling motion.

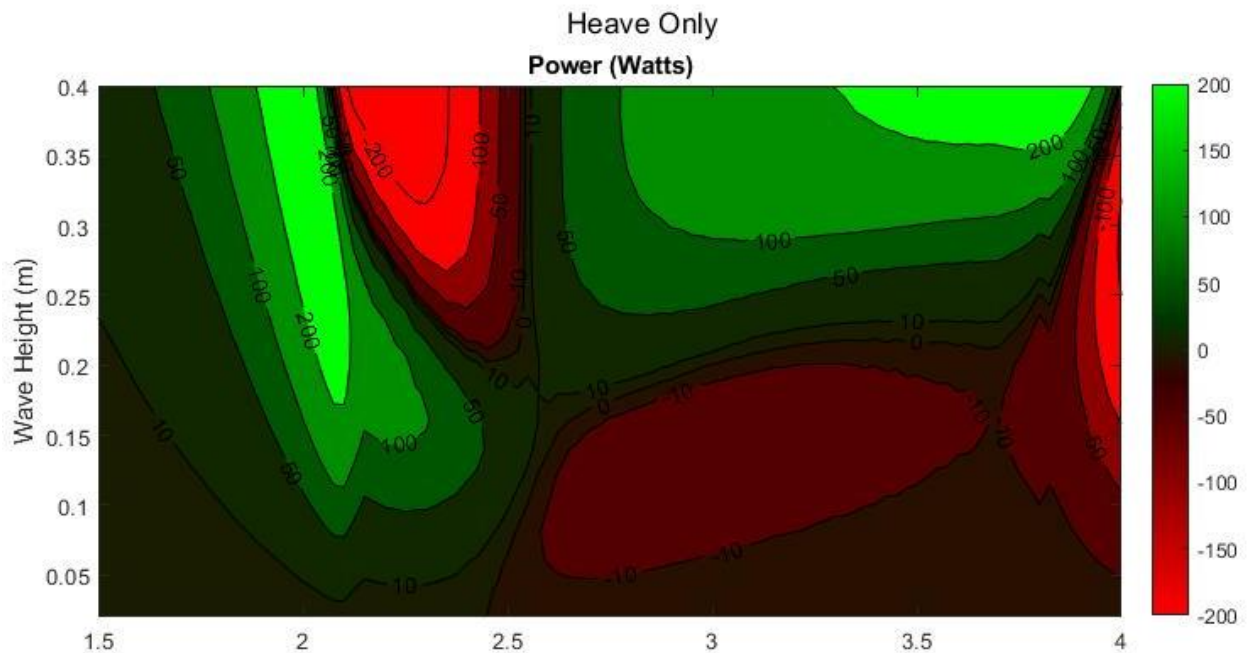


Figure 61: Comparison of the 2-body and 3-body power productions in Watts. Red shows where the 2-body system outperforms the 3-body system and green shows the opposite.

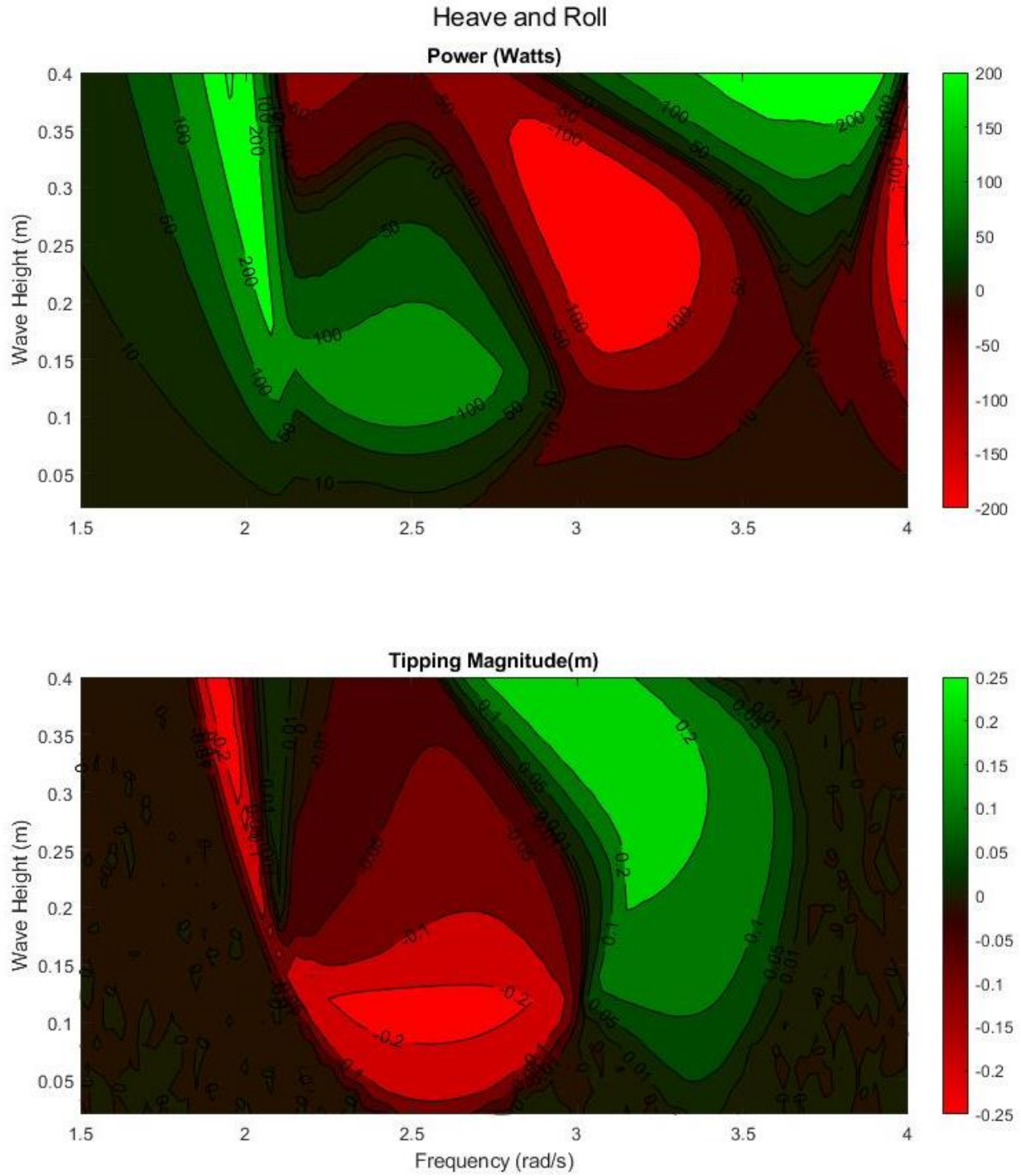


Figure 62: Comparison between the 2-body and 3-body systems Heave Only case of a) power production in watts and b) tipping magnitude in meters. Green areas show where the 3-body system values are greater than the 2-body system.

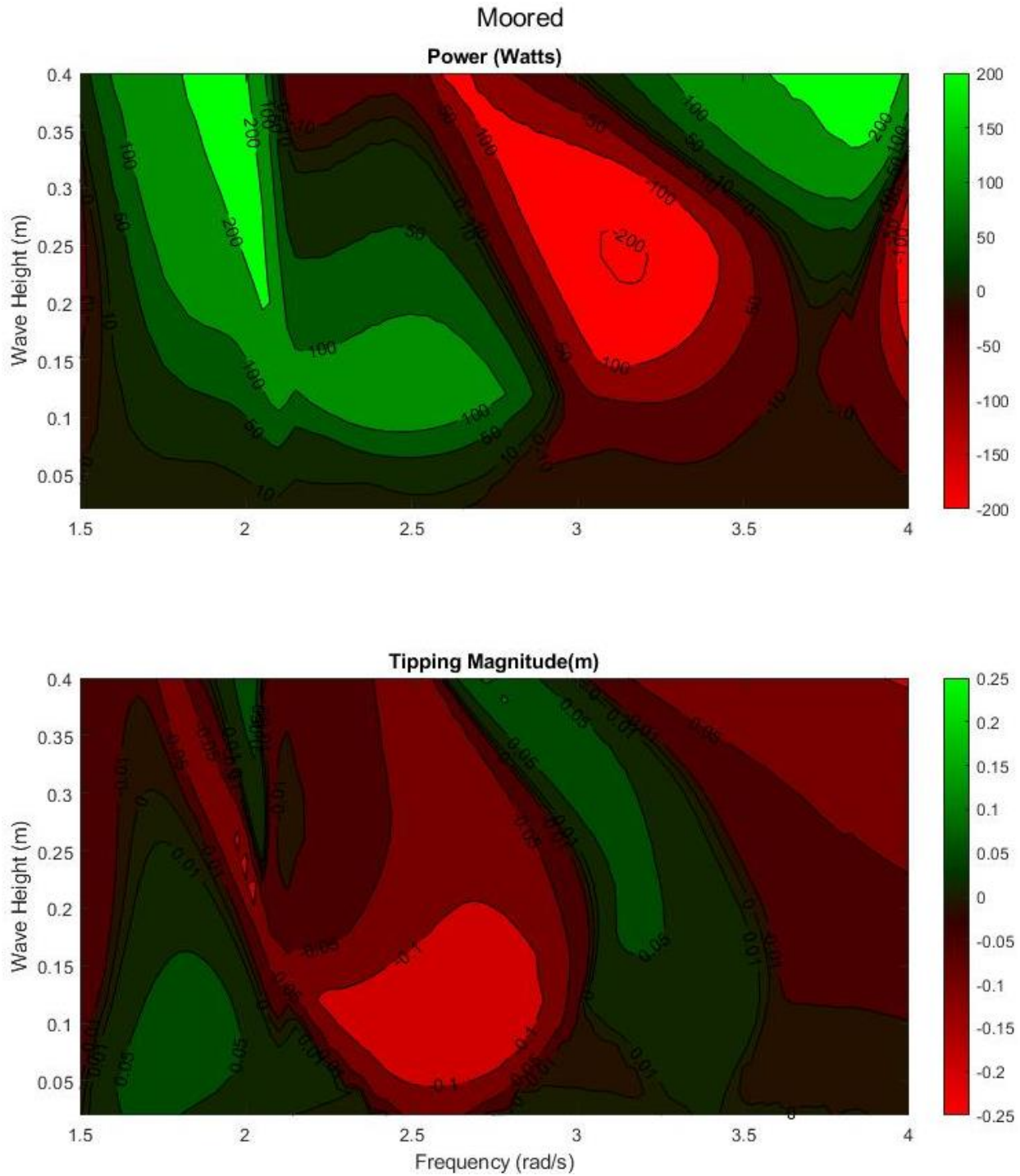


Figure 63: Comparison between the 2-body and 3-body systems Moored case of a) power production in watts and b) tipping magnitude in meters. Green areas show where the 3-body system values are greater than the 2-body system.

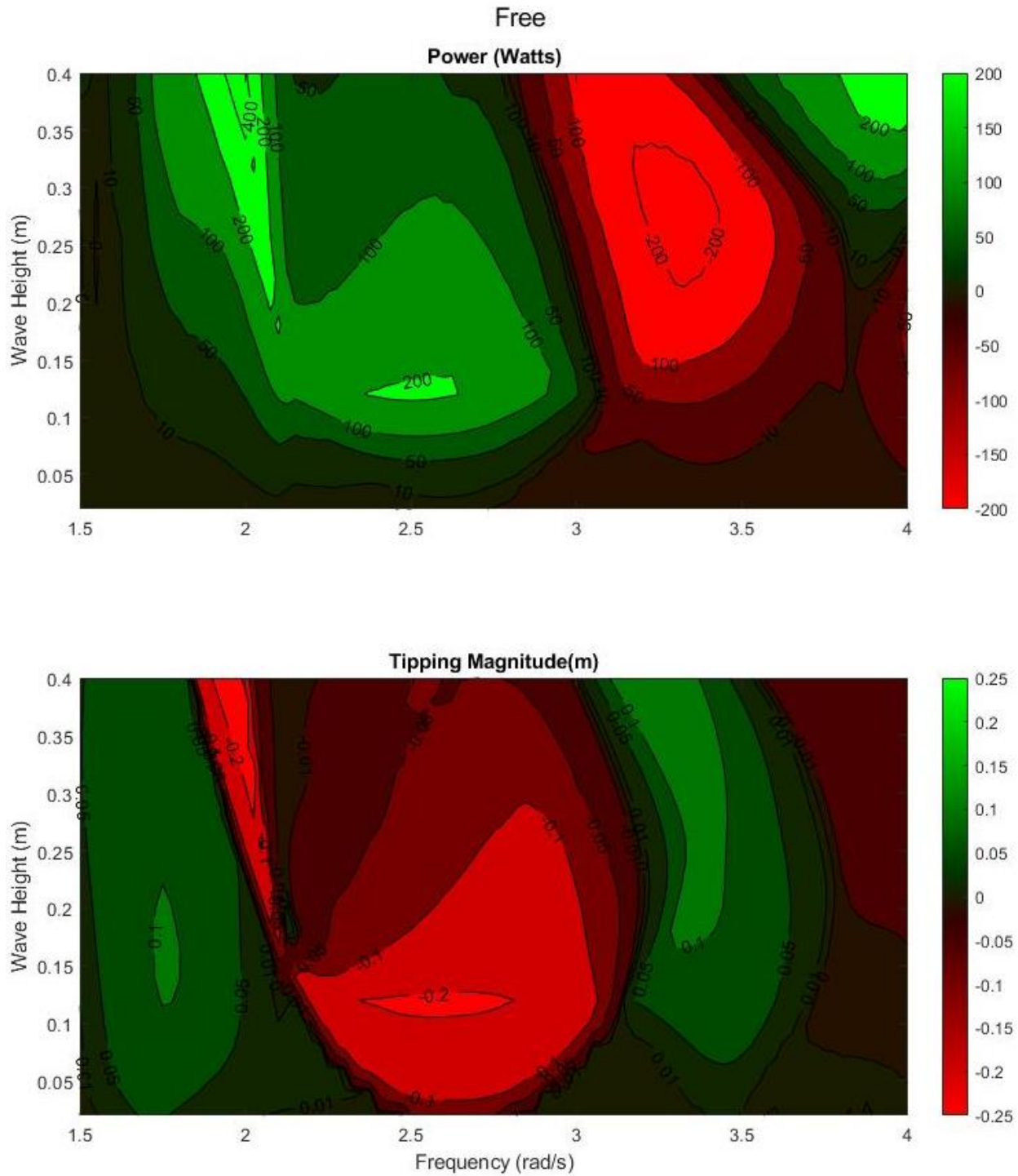


Figure 64: Comparison between the 2-body and 3-body systems Free case of a) power production in watts and b) tipping magnitude in meters. Green areas show where the 3-body system values are greater than the 2-body system.

Rolling motions are exclusively parasitic to power production, proof exists in the results of the scenarios in which the system moves in modes of motion other than heave and does not produce as much power as the heave only scenario, however pitching motion can increase power production higher than the heave only power production. This is interesting as it defies the idea that any motion other than heaving motion reduces power production. The only way pitching motion could add to the production of power is if the pitching motion increased the velocity between the Float and Spar. Rolling motions are reduced with the implementation of the VIS although the bandwidth of rolling response is widened which reduces the power production below that of the 2-body outside of its own rolling response but overall the 3-body system outperforms the 2-body system.

Chapter 6 Conclusions and Future Work

6.1 Observational Conclusions

6.1.1 PTO Damping Value

The implemented control strategy for the choice of PTO damping value falls short of the brute force optimized PTO value at the peak of the value over the tested frequency range making it sub-optimal, resulting in lower power production as shown in Figure 41. The sub-optimal setting of the PTO damping value contaminates the results shown by the valley of reduced power production in the Heave Only case shown in Figure 48. There should be higher peak power production rather than the valley of reduced power production but this is the consequence of the chosen method of PTO damping. While ideally the optimal PTO damping value would be implemented, the design space is too large for a 3-body system, having both a variable PTO value as well as rotational inertia of the VIS, to be computationally and temporally economic. The use of the closest possible value utilizing the least computationally expensive, most accurate techniques available at this time shows that the techniques still fall short, curtailing the peak power production.

6.1.2 VIS Implementation

The implementation of the VIS demonstrates higher power production and stabilization of the system with regards to parametric excitation. However the activation of the VIS seems to induce rolling motion even outside the range of twice the natural rolling frequency of the system shown in Table 8. This means that changing the response in the heave direction has an impact on rolling position but more testing is required. There exists an interesting relation between $2x$ the

roll natural frequency and the heave natural frequency as they are close in value (~2.64 rad/s compared to ~2.54 rad/s) due to the geometry of the system.

6.2 Future Work

6.2.1 PTO Value

The VISWEC has the potential to outperform the SRPA across all frequencies although a better method for calculating the optimal PTO damping value is needed. Bubbar outlined a method to extract velocities from data produced by WAMIT based on the linearized impedance, it would be interesting to see how these velocities match up to the velocities determined through ProteusDS. A better coefficient $\left(\frac{8}{3\pi}\right)$ in eq. (4.7), Clauss's estimation for linear drag force with a known quadratic drag coefficient would also help to more closely estimate the linearized drag force for use in PTO damping value calculation. To obtain this new coefficient a series of tests would need to be run or possibly derive a new coefficient for heaving using the method Clauss outlined for surge. Focus should be on matching the drag in resonance, the range of higher PTO values for 2-body system, rather than outside of this range as the 3-body device would be designed to resonate at a wider bandwidth of frequencies.

6.2.2 Frequency Testing Range

The design of the 3-body system would be of more use for full scale deployment off the West coast of Vancouver Island if the VIS was active in the higher frequency range, full scale period of 5-13 seconds [17] correlating to a 1/25th scale frequency range of 2.4-6.3 rad/s. This shift could be accomplished by changing the scale of the model, since no full scale VISWEC exists the change in scale is only a change in the concept of the full scale WEC. If the model designed is considered to be 1/20th scale instead of 1/25th scale the values would more closely relate to the environment off the coast of the west coast of Vancouver Island as shown in Table 13.

Table 13: 1/20th Scaled and Corresponding Full-scale Model Settings

Model Settings						
Parameter	1/20th scale			Full-scale		
	Min	Max	Inc	Min	Max	Inc
Frequency (rad/s)	1.50	4.00	0.025	0.34	0.89	0.006
Frequency (Hz)	0.24	0.64	0.004	0.05	0.14	0.001
Period (s)	1.57	4.19	0.026	7.02	18.73	0.117
Wave Height (m)	0.02	0.40	0.020	0.40	8.00	0.400

The frequencies tested in this work were more based on the limitations of the wave tank available in previous experimental testing rather than the wave field. The upper limit of the tested frequencies (4.0 rad/s) could have been increased to include the lower period of the wave environment off the coast of the west coast of Vancouver Island. This higher range of frequencies would show the dynamics of each system throughout the range. This would more importantly show the 3-body system where power production starts to drastically decrease at 4.0 rad/s without the increase in rolling or pitching motions. It would be interesting to see what happens to the system in this higher frequency range.

6.2.3 VIS Testing Range

For testing against the 2-body SRPA, it would have been better to have the VIS active over a larger frequency range, especially at the lower frequencies further away from the 2.5 rad/s, the natural frequency of the 2-body system. The limits of the VIS were placed based on the limits of the 1/25th scale physical model, to activate the VIS at lower frequency higher inertial settings would be necessary. The wider implementation of the VIS is a means for comparison of an optimally active 3-body system over the larger bandwidth of frequencies.

6.2.4 Limiting Parametric Excitation

Work to reduce the rolling motion caused by parametric excitation could be performed. The design of the outer hull could be revisited as Beatty et al. did when adding strakes to the geometry in attempt to reduce the pitching and rolling motion [39]. Though as the results show, pitching motions ideally would not be damped as they increase power production, only rolling motion would be damped as they are parasitic to power production as shown in comparison Figure 55 and Figure 58. The trouble with trying to limit only a single tipping DoF, roll or pitch,

is that in a natural wave environment, multi-frequency multi-directional with different wave heights, roll and pitch are not solely one direction.

The best way to limit parasitic parametric excitation is to limit the internal resonance of the stiffness parameter of the righting moment. It may be possible to limit parametric excitation with alternate settings of the VIS. It could be that the optimal setting for the VIS is not at the optimal setting set by impedance matching but rather slightly offset so as to not induce parametric excitation.

References

- [1] R. L. Johansen, "Machine for Utilizing Ocean Power," 475451, 1892.
- [2] "Our Electricity Future: Nova Scotia's Electricity Plan 2015-2040," 2015.
- [3] S. H. Salter, "Wave power," *Nature*, vol. 249, no. 5459, pp. 720–724, 1974.
- [4] K. Budar and J. Falnes, "A resonant point absorber of ocean-wave power," *Nature*, vol. 256, no. 5517, pp. 478–479, 1975.
- [5] Sweden.se, "Energy use in Sweden," 2016. .
- [6] BBC, "Scottish wind power surge reported in 2015," *BBC News Scotland*, 2016. .
- [7] Scotland Crown, "Energy in Scotland: Get the Facts," 2017. .
- [8] "Electricidad Con Sello Sostenible."
- [9] International Energy Agency, "World Energy Investment 2016," *Int. Energy Agency*, 2016.
- [10] V. Smil, "World history and energy," *Encycl. Energy*, vol. 6, pp. 549–561, 2004.
- [11] M. Z. Jacobson *et al.*, "100% clean and renewable wind, water, and sunlight (WWS) all-sector energy roadmaps for the 50 United States," *Energy Environ. Sci.*, vol. 8, no. 7, pp. 2093–2117, 2015.
- [12] G. Reikard, B. Robertson, and J. R. Bidlot, "Combining wave energy with wind and solar: Short-term forecasting," *Renew. Energy*, vol. 81, pp. 442–456, 2015.
- [13] N. W. Miller, M. Shao, S. Pajic, and R. D'Aquila, "Western Wind and Solar Integration Study Phase 3: Frequency Response and Transient Stability."
- [14] K. Gunn and C. Stock-Williams, "Quantifying the global wave power resource," *Renew. Energy*, vol. 44, pp. 296–304, 2012.
- [15] E. Luczko, "Assimilating a Higher Fidelity Representation of Wave Energy Converters in a Spectral Model," University of Victoria, 2016.
- [16] N. Booij and L. H. Holthuijsen, "Propagation of ocean waves in discrete spectral wave models," *J. Comput. Phys.*, vol. 68, no. 2, pp. 307–326, 1987.
- [17] B. R. D. Robertson, C. E. Hiles, and B. J. Buckham, "Characterizing the near shore wave energy resource on the west coast of Vancouver Island, Canada," *Renew. Energy*, vol. 71, pp. 665–678, 2014.
- [18] A. Cornett and J. Zhang, "Nearshore Wave Energy Resources, Western Vancouver Island, B.C.," *Energy*, no. April, p. 78, 2008.
- [19] J. Cruz, *Ocean Wave Energy*. 2008.
- [20] I. Martínez de Alegría, I. Kortabarria, J. Andreu, I. López, and S. Ceballos, "Review of wave energy technologies and the necessary power-equipment," *Renew. Sustain. Energy Rev.*, vol. 27, pp. 413–434, 2013.
- [21] E. Ozkop and I. H. Altas, "Control, power and electrical components in wave energy conversion systems: A review of the technologies," *Renew. Sustain. Energy Rev.*, vol. 67, pp. 106–115, 2017.
- [22] J. Falnes, *Ocean Waves and Oscillating Systems: Linear Interactions Including Wave-Energy Extraction*. Cambridge University Press, 2002.
- [23] J. Falnes, "Wave-Energy Conversion Through Relative Motion Between Two Single-Mode Oscillating Bodies," *J. Offshore Mech. Arct. Eng.*, vol. 121, no. 1, p. 32, 1999.

- [24] L. Meirovitch, *Elements of Vibration Analysis*, 2nd ed. McGraw-Hill, 1986.
- [25] K. Bubbar and B. Buckham, "On establishing an analytical power capture limit for self-reacting point absorber wave energy converters based on dynamic response," *Appl. Energy*, vol. 228, no. June, pp. 324–338, 2018.
- [26] J. Hals, "A Comparison of Selected Strategies for Adaptive Control of Wave Energy Converters A Comparison of Selected Strategies for Adaptive Control of," no. January 2016, 2011.
- [27] W. Dick, "Wave energy converter," US 6857266 B2, 2001.
- [28] B. Orazov, O. M. O'Reilly, and S. Savaş, "On the dynamics of a novel ocean wave energy converter," *J. Sound Vib.*, vol. 329, no. 24, pp. 5058–5069, 2010.
- [29] S. J. Beatty, M. Hall, B. J. Buckham, P. Wild, and B. Bocking, "Experimental and numerical comparisons of self-reacting point absorber wave energy converters in regular waves," *Ocean Eng.*, vol. 104, pp. 370–386, 2015.
- [30] S. J. Beatty *et al.*, "Experimental and numerical comparisons of self-reacting point absorber wave energy converters in irregular waves," *Ocean Eng.*, vol. 173, no. January, pp. 716–731, 2019.
- [31] K. Bubbar, B. Buckham, and P. Wild, "A method for comparing wave energy converter conceptual designs based on potential power capture," *Renew. Energy*, vol. 115, pp. 797–807, 2018.
- [32] Falcao, "Wave energy utilization: A review of the technologies," *Renew. Sustain. Energy Rev.*, vol. 14, pp. 899–918, 2010.
- [33] B. Orazov and O. M. O. Reilly, "On the dynamics of a novel ocean wave energy converter," *J. Sound Vib.*, vol. 329, pp. 5058–5069, 2010.
- [34] C. A. Diamond, C. Q. Judge, B. Orazov, Ö. Sava, and O. M. O. Reilly, "Mass-modulation schemes for a class of wave energy converters : Experiments , models , and ef fi cacy," vol. 104, pp. 452–468, 2015.
- [35] C. A. Diamond, O. M. O'Reilly, and Ö. Savaş, "The impulsive effects of momentum transfer on the dynamics of a novel ocean wave energy converter," *J. Sound Vib.*, vol. 332, no. 21, pp. 5559–5565, 2013.
- [36] M. Mosher, *A New Methodology for Frequency Domain Analysis of Wave Energy Converters with Periodically Varying Physical Parameters*. 2012.
- [37] N. Protter, B. Buckham, and S. Beatty, "Wave Energy Converter (SyncWave)," WO/2007/137426, 2007.
- [38] S. J. Beatty, "Analysis and Development of a Three Body Heaving Wave Energy Converter," University of Victoria, 2009.
- [39] S. Beatty, A. R. Roy, J. Ortiz, and P. M. Wild, "Experimental and Numerical Simulations of Moored Self-Reacting Point Absorber Wave Energy Converters," *Int. Ocean Polar Eng. Conf.*, no. June 2016, pp. 924–935, 2015.
- [40] J. Ortiz, "The Influence of Mooring Dynamics on the Performance of Self Reacting Point Absorbers," University of Victoria, 2016.
- [41] H. W. Louisell, *Coupled Mode and Parametric Electronics*. New York: Wiley, 1960.
- [42] J. F. Rhoads, N. J. Miller, S. W. Shaw, and B. F. Feeny, "Mechanical Domain Parametric Amplification," *J. Vib. Acoust.*, vol. 130, no. 6, p. 061006, 2008.
- [43] D. N. Veritas, "Environmental conditions and environmental loads," *Dnv*, no. October, pp.

- 9–123, 2010.
- [44] H. A. Haslum, U. Olje, and O. M. Faltinsen, “Alternative Shape of Spar Platforms for Use in Hostile Areas,” *Proc. Offshore Technol. Conf.*, pp. 1–12, 1999.
- [45] J. B. Rho, H. S. Choi, W. C. Lee, H. S. Shin, and I. K. Park, “Heave And Pitch Motions of a Spar Platform With Damping Plate.” International Society of Offshore and Polar Engineers.
- [46] L. Zhang, J. Zou, and E. W. Huang, “Mathieu instability evaluation for DDCV/SPAR and TLP tendon design,” in *Proceedings of the 11th Offshore Symposium, Society of Naval Architect and Marine Engineer*, 2002, pp. 41–49.
- [47] B. J. Koo, M. H. Kim, and R. E. Randall, “Mathieu instability of a spar platform with mooring and risers,” vol. 31, pp. 2175–2208, 2004.
- [48] M. A. S. Neves and C. A. Rodriguez, “On unstable ship motions resulting from strong non-linear coupling,” vol. 33, pp. 1853–1883, 2006.
- [49] M. A. S. Neves, B. M. Mattoso, C. Ufrj, and A. L. Santos, “Omae2008-57 567,” pp. 1–9, 2008.
- [50] A. Olvera, E. Prado, and S. Czitrom, “Parametric resonance in an oscillating water column,” *J. Eng. Math.*, vol. 57, no. 1, pp. 1–21, 2007.
- [51] J. H. Todalshaug *et al.*, “Tank testing of an inherently phase-controlled wave energy converter,” *Int. J. Mar. Energy*, vol. 15, pp. 68–84, 2016.
- [52] K. Tarrant and C. Meskell, “Investigation on parametrically excited motions of point absorbers in regular waves,” *Ocean Eng.*, vol. 111, pp. 67–81, 2016.
- [53] C. Villegas and H. Van Der Schaaf, “Implementation of a Pitch Stability Control for a Wave Energy Converter.”
- [54] J. E. Kerwin, “Note on rolling in longitudinal waves,” *Int Shipbuild Prog*, vol. 2, no. 16, pp. 597–614, 1955.
- [55] J. Paulling and R. Rosenberg, “On Unstable Ship Motions Resulting From Nonlinear Coupling,” 1959.
- [56] J. Paulling, “The Transverse Stability of a Ship in a Longitudinal Seaway,” *J. Sh. Res.*, vol. 4, no. 4 (Mar), pp. 37–49, 1961.
- [57] N. Umeda, H. Hashimoto, D. Vassalos, S. Urano, and K. Okou, “Nonlinear Dynamics on Parametric Roll Resonance with Realistic Numerical Modelling,” pp. 281–290.
- [58] A. Allievi and A. Soundack, “Ship stability via the Mathieu equation,” *Int. J. Control*, vol. 51, no. 1, pp. 139–167, 1990.
- [59] J. C. Gutie and S. Cha, “Mathieu functions, a visual approach,” pp. 233–242, 2003.
- [60] L. Ruby, “Applications of the Mathieu equation,” vol. 3680, no. 1982, pp. 108–112, 1996.
- [61] “MATLAB.” The MathWorks Inc, Natick, Massachusetts, United States, 2015.
- [62] J. Falnes, “A review of wave-energy extraction,” vol. 20, no. 0951, pp. 185–201, 2007.
- [63] H. Bailey, B. R. D. Robertson, and B. J. Buckham, “Wave-to-wire simulation of a floating oscillating water column wave energy converter,” *Ocean Eng.*, vol. 125, pp. 248–260, 2016.
- [64] A. Kurniawan, J. Hals, and T. Moan, “Modelling and Simulation of a Floating Oscillating Water Column,” *Int. Conf. Ocean. Offshore Arct. Eng. OMAE*, vol. June, 2011.
- [65] J. C. C. Henriques, A. Falcao, R. P. F. Gomes, and L. M. C. Gato, “OMAE2013-11213,” *Int. Conf. Ocean. Offshore Arct. Eng. OMAE*, vol. June, pp. 1–9, 2013.

- [66] A. Babarit, J. Hals, A. Kurniawan, and T. Moan, "The NumWEC project. Numerical estimation of energy delivery from a selection of wave energy converters – final report," no. April, 2011.
- [67] V. Mishra, S. Beatty, B. Buckham, P. Oshkai, and C. Crawford, "Application of an Arbitrary Mesh Interface for CFD Simulation of an Oscillating Wave Energy Converter," *Proc. 11th Eur. Wave Tidal Energy Conf.*, no. September, pp. 1–10, 2015.
- [68] A. R. Roy, S. J. Beatty, V. Mishra, D. M. Steinke, R. S. Nicoll, and B. J. Buckham, "A Submission for the Hydrodynamic Modelling of a Rigid Body," *OMAE*, 2015.
- [69] "ProteusDS 2013 Manual," 2014.
- [70] M. F. P. Lopes, J. Hals, R. P. F. Gomes, T. Moan, L. M. C. Gato, and A. F. d. O. Falcão, "Experimental and numerical investigation of non-predictive phase-control strategies for a point-absorbing wave energy converter," *Ocean Eng.*, vol. 36, no. 5, pp. 386–402, 2009.
- [71] A. S. Zurkinden, F. Ferri, S. Beatty, J. P. Kofoed, and M. M. Kramer, "Non-linear numerical modeling and experimental testing of a point absorber wave energy converter," *Ocean Eng.*, vol. 78, pp. 11–21, 2014.
- [72] S. Olaya, J. M. Bourgeot, and M. Benbouzid, "Modelling and preliminary studies for a self-reacting point absorber WEC," *2014 1st Int. Conf. Green Energy, ICGE 2014*, pp. 14–19, 2014.
- [73] S. J. Beatty, "Self Reacting Point Absorbers," University of Victoria, 2015.
- [74] Dassault Systems, "SolidWorks." 2014.
- [75] AeroHydro, "MultiSurf." Southwest Harbor, Maine, 2011.
- [76] WAMIT Inc., "WAMIT User Manual - Version 7.1," p. 375, 2015.
- [77] K. Bubbar, "Conceptual design of wave energy converters," University of Victoria, 2018.
- [78] G. Clauss, E. Lehmann, and C. Ostergaard, *Offshore Structures: Volume I: Conceptual Design and Hydromechanics*, Illustrate. Springer International Publishing, 2014.
- [79] C. E. Hiles, B. J. Buckham, P. Wild, and B. Robertson, "Wave energy resources near Hot Springs Cove, Canada," *Renew. Energy*, vol. 71, pp. 598–608, 2014.